Low-Frequency Unsteadiness in the Wake of a Normal Flat Plate

F.M. Najjar
National Center for Supercomputing Applications
University of Illinois at Urbana-Champaign

and S. Balachandar
Theoretical and Applied Mechanics
University of Illinois at Urbana-Champaign
Urbana, IL 61801, U.S.A.

Abstract

The separated flow past a zero-thickness flat plate held normal to a free stream at Re=250 has been investigated through numerical experiments. The long-time signatures of the drag and lift coefficients clearly capture a low frequency unsteadiness with a period of approximately 10 times the primary shedding period. It is observed that the low-frequency unsteadiness is not a simple superposition of a low frequency undulation imposed on the shedding frequency. The amplitude of drag and lift variations during the shedding process is strongly modulated by the low frequency. Furthermore, the low frequency unsteadiness modulates the shedding frequency, with the shedding frequency increasing with increasing mean drag. A simple model is proposed to characterize these variations. A physical interpretation of the low frequency behavior is that the flow oscillates between two different regimes: a regime **H** of high mean drag and a regime **L** of low mean drag. The fundamental difference in the Karman vortex dynamics between these two regimes is also explored through a phase-averaging procedure. It is observed that in regime **H** the shear layer rolls-up closer to the plate to form coherent spanwise vortices, while in regime **L** the shear layer extends farther downstream and the rolled-up Karman vortices are less coherent. The eduction of the three-dimensional vortical structures is achieved by defining the swirling strength as the imaginary part of the complex eigenvalue of the velocity gradient tensor and visualizing it. The three-dimensional structure of the wake is significantly different between regimes **H** and **L**. In the high drag regime three-dimensionality is characterized by coherent Karman vortices which are deformed along the spanwise direction and reasonably well organized streamwise vortices connecting the Karman vortices. With a non-dimensional near wake spanwise wavelength of about 1.2, the three-dimensionality in this regime is reminiscent of mode B three-dimensionality. It is observed that the high degree of spanwise coherence that exists in regime **H** breaks down in regime **L**. In the low drag regime the Karman vortices are seen to tear apart and gets tilted along the streamwise direction to form highly incoherent collection of streamwise vortices. It appears that the low frequency unsteadiness might be the result of a beat phenomenon arising from the interaction between the characteristic shedding frequencies in regime **H** and **L**. Based on detailed visualization of flow structures we conjecture that the formation of streamwise and spanwise vortices are not in perfect synchronization and that the low frequency unsteadiness is the result of this imbalance (or phase mismatch).

1. Introduction

Wakes of bluff bodies have been extensively studied because of their relevance to drag on vehicles, flow over ship hulls, and submarines. Such flows provide rich and interesting flow dynamics of considerable engineering relevance. Bluff bodies such as plates, discs, circular and rectangular cylinders, and V-shaped prisms, are used in combustors to enhance scalar mixing and provide a flame-stabilizing region. Several basic geometrical configurations including circular and rectangular cylinders, flat plates, and airfoils have been experimentally and numerically investigated to understand the fundamental aspects of flow separation and wake instabilities. The normal flat plate is one the simplest bluff body configuration that can be used to understand wake instabilities. Unlike the case of the circular cylinder, the flow past a flat plate is characterized by fixed separation points at the edges of the plate. As a result, the wake behind a normal plate exhibits interesting complex dynamics even at modest Reynolds numbers.

There have been several previous experimental and numerical studies of flow past a flat plate placed in a uniform stream. Almost all of the experimental studies have been in the high Reynolds number regime. Fage & Johansen (1927) conducted one of the earliest measurements of the upstream and downstream pressures for different angles of attack at a Reynolds number of $1.5\text{x}10^5$. Since then several other researchers (Bradbury & Moss 1975, Perry & Steiner 1987, Steiner & Perry 1987, Kiya & Matsumura 1988, Chua *et al.* 1990, Leder 1991 and Lisoski 1993) have investigated flow past a normal plate covering a wide range of Reynolds number from 1000 to 5×10^5. Compared to the experimental studies, a relatively smaller number of numerical studies have been carried out for the flow past a normal flat plate. Earliest attempts are by Kuwahara (1973) and Kiya & Arie (1980) using discrete-vortex method. Castro & Jones (1987) performed two-dimensional steady-state numerical simulations for Reynolds number in the range of 100 to 800 using finite-difference and finite-element techniques assuming symmetry of the flow about the centerline. Because of the steady-state assumption and the symmetry condition, the length of the mean wake recirculation region was significantly over-predicted. These computations have since then been improved (Lisoski 1993) and extended to three-dimensions (Joshi, Vanka & Tafti 1994, Najjar 1994, Najjar & Vanka 1995a, Najjar & Balachandar 1996).

A significant observation that can be made from the above studies (Lisoski 1993, Joshi et al.1994, Najjar 1994 and Najjar & Balachandar 1996) is that the temporal signal of drag and lift

coefficients is marked by a strong component of low frequency unsteadiness, over a wide range of Reynolds number from 250 to 2.5×10^5. The low frequency is about one tenth of the primary shedding frequency. Instantaneous drag coefficient can be observed to evolve back and forth between periods of high mean drag and periods of low mean drag. This results in a low frequency component superposed on the drag coefficient, in addition to its variation at twice the Karman vortex shedding frequency. Owing to symmetry of the wake about the centerline, no such low frequency component is superposed on the lift coefficient, which oscillates at the shedding frequency. On the other hand, the amplitudes of variation in both the drag and lift coefficients over a shedding cycle are significantly modulated by the low frequency unsteadiness. In addition to the amplitude modulation, a low frequency modulation of the shedding frequency can also be observed. In the discrete vortex simulations of Kiya & Arie (1980), a sustained low frequency unsteadiness was not observed, but a similar effect can be seen in the initial transients. The flow was observed to transition from an initial state of low mean drag to an eventual state of high mean drag.

In the canonical case of a circular cylinder, the presence of low frequency unsteadiness is not so clear. One of the earliest evidence of low frequency unsteadiness can be found in the seminal work on cylinder wake by Roshko (1954). In the Reynolds number range between 150 to 300, termed the transition range, irregular bursts appeared in the oscillograms, which he cited as the cause of the scatter in the measurement of shedding frequency. An examination of the oscillograms shows an approximate period of about 10 times the shedding period for the irregular bursts. Based on dye visualizations and velocity measurements at several points in the wake of a circular cylinder Tritton (1959) observed two different modes of Karman vortex shedding: a low-speed mode in the range $40<Re<110$ and a high-speed mode in the range $80<Re<160$. He observed the low-speed mode to result from an instability of the wake and the high-speed mode to result from the shedding of attached vortices off the cylinder. The low-speed and high-speed modes differed in their shedding frequency, and the transition between them was characterized by periodic beating, which was on the order of 6 to 14 times the primary shedding period. Berger (1964) observed similar transition between different frequencies in his measurements of air flow over thin cylinders.

Subsequent experiments by Gaster (1969) raised the possibility that the discontinuity in the shedding frequency and the low frequency beating observed by Tritton (1959) and Berger (1964) are due to flow nonuniformities. Gaster's (1969) measurements in the wake of a slender cone, whose local Reynolds number varied along the span, clearly showed low frequency beating. The beating frequency was observed to be the same throughout the flow and depended on the

spanwise variation in the shedding frequency. Similar phenomenon was observed in the case of a slightly tapered cylinder as well (Gaster 1971), marked by spanwise cells of regular periodic shedding with jumps in the shedding frequency between neighboring cells. In the transition regions between spanwise cells a low frequency beating, corresponding to the frequency difference between the adjacent cells, was observed. Such beating can also be observed in the case of a perfect cylinder subjected to a spanwise varying flow.

The effect of cylinder ends on the nature of Karman vortex shedding was investigated by Gerich & Eckelmann (1982). They observed a central region of regular shedding frequency and affected regions, near the cylinder ends, characterized by a lower frequency. Above a certain critical Reynolds number beatings were observed corresponding to the frequency difference between the central and the affected end zones. They also showed that beatings can be avoided in the central zone by appropriately manipulating the cylinder end conditions. Recent computations by Dauchy, Dusek & Fraunie (1997) confirm the influence of cylinder's free ends in generating a low frequency beating even at Reynolds numbers as low as 54. Apart from cylinder end conditions, cylinder vibration due to aeroelastic effects has also been know to result in low frequency unsteadiness (Van Atta & Gharib 1987).

Williamson (1992, 1996) made an experimental observation that in the wake transition regime ($180<Re<260$), where mode A instability gives way to mode B instability, two different shedding frequencies coexist. The higher shedding frequency is associated with a more regular three-dimensional state characterized by mode B instability, whereas, the lower shedding frequency is associated with large scale vortex dislocations. He also observed that the two frequencies do not coexist at one time, but the flow intermittently swaps between the lower and higher frequencies. The corresponding velocity signature at downstream locations ($x>10$) exhibited primary oscillation at the shedding frequency along with "glitches" associated with the large scale vortex dislocations. The "glitches" or the vortex dislocations were observed to occur at a low frequency, but for lack of direct measurement the magnitude of their impact on drag and lift can not be ascertained.

At reasonably high Reynolds number, in the range of 5×10^4 to 7×10^6, Schewe (1983) observed a strong low frequency component in the time trace of drag and lift coefficients for a circular cylinder. The measured temporal variation was qualitatively very similar to that observed for the normal plate by Lisoski (1993) and Najjar (1994). He noted significant correlation between peak rms fluctuation of lift coefficient and strong spanwise coherence. Similar low frequency bursting history has also been observed in pressure and velocity

measurements at points near the circular cylinder at Re=1.3×10^5 by Szepessy & Bearman (1992). More recently Szepessy (1994) reported strong oscillation in the spanwise correlation of surface pressure measured on a circular cylinder near the separation line having periods around 10 to 20 times the Strouhal period. The pressure correlation between different spanwise points also indicated that the low frequency unsteadiness was associated with phase shifts, which he conjectured were similar to the natural vortex dislocations addressed by Williamson (1992). Szepessy (1994) also proposed some simple plausible explanations for the measured spanwise phase drift and low frequency unsteadiness.

On the computational front, Karniadakis & Triantafyllou (1992) reported that in the Reynolds number range between 175 to 500 the wake of a circular cylinder undergoes a cascade of three-dimensional period doubling bifurcations which eventually lead to a chaotic state. They pointed out that at Re=500 the time trace of streamwise velocity signal shows periods of almost periodic behavior interspersed with periods of apparently random behavior. This observation can be interpreted as a manifestation of low frequency unsteadiness, but the time series is not long enough to be conclusive. The time traces of drag and lift coefficients presented in Mittal & Balachandar (1995a) for cylinders of three-different cross-section at Re=525 are also not long enough to shed light on their possible low frequency behavior. At Re=500 Henderson (1994) observed a periodic surge mainly in the lift force on a time scale much longer than the shedding period. At a higher Reynolds number of Re=1000 periodic bursts appear in both the drag and lift coefficients. Recent simulations by Belov, Martinelli & Jameson (1997) at Re=225 reported the presence of a low frequency component in the time trace of lift coefficient and base pressure. In general, in all the above simulations performed at low to modest Reynolds numbers, the observed amplitude of low frequency unsteadiness has been small that the low frequency behavior has not attracted much attention in the case of a circular cylinder.

The importance of cylinder end conditions in the generation of low frequency beating at fairly low Reynolds numbers has been well established from the experiments of Gaster (1969, 1971) and Gerich & Eckelmann (1982) and the recent computations of Dauchy et al. (1997). In the high Reynolds number experiments of Szepessy & Bearman (1992) and Lisoski (1993), the period of low frequency unsteadiness was observed to somewhat influenced by the cylinder aspect ratio. Nevertheless, as pointed out by Roshko (1993) the importance of spanwise end conditions on low frequency unsteadiness is not entirely clear. Furthermore, the observation of low frequency unsteadiness in the three-dimensional simulations, where end conditions are avoided with an assumption of spanwise periodicity, suggests that low frequency unsteadiness is an intrinsic property of the wake. While imperfect cylinder ends can certainly lead to low

frequency beating even at very low Reynolds numbers, there is sufficient evidence to suggest that it is entirely possible for the natural wake (without the influence of cylinder ends) to develop low frequency unsteadiness owing to interaction of intrinsic instabilities of the wake.

Low frequency unsteadiness has attracted significant attention in the context of separating-and-reattaching flows, such as flow past a backward facing step (Eaton & Johnston 1982) and blunt flat plate (Kiya & Sasaki 1983, 1985 and Cherry, Hillier & Latour 1984). Here the primary imprint of low frequency is in the slow back and forth streamwise oscillation of the reattachment point about its time-averaged mean location. The above experiments have employed simultaneous flow visualization, wall pressure and fluctuating velocity measurements to infer the details of the flow structure and the low frequency unsteadiness. Eaton & Johnston (1982) suggested that the low frequency unsteadiness is associated with a near two-dimensional vertical movement of the shear layer. Later measurements by Kiya & Sasaki (1985) confirmed this suggestion, but the amplitude of vertical oscillation was observed to be only 2.5% of the blunt flat plate's thickness. Eaton & Johnston (1982) further suggested that the low frequency unsteadiness is the consequence of an instantaneous imbalance between the entrainment from the recirculation region along the shear layer and the reinjection of fluid near the reattachment point. This hypothesis was supported by the experimental measurements of Kiya & Sasaki (1985), who observed the recirculation region to periodically shrink and enlarge in size in response to changes in entrainment. The speed of shrinkage was estimated to be faster than the speed of enlargement. They speculated that the strength of the spanwise vortices in the reattaching zone depends on the phase of the low frequency unsteadiness. They further went on to verify that the low frequency behavior is associated with short term breakdown in the spanwise coherence of the spanwise vortices.

Cherry et al. (1984) associated the low frequency unsteadiness with the characteristic time scale of relaxation between two different phases of shedding, and attempted to explain the cause of back and forth oscillation in the instantaneous reattachment point. They described this behavior as "necking" of the shear layer and occasional pseudo-periodic bursts of large scale vortices. Tafti & Vanka (1991) have performed three-dimensional numerical simulations of the unsteady flow over a blunt plate at Re=1000. They captured a low-frequency component in the evolution of the shear layer, with characteristic period of six shedding cycles. Based on numerical flow visualization, they found evidence of at least one stronger than usual vortex shedding during the shrunken state of the recirculation region. They provided conjectures similar to those of Eaton & Johnston (1982), Cherry et al. (1984) and Kiya & Sasaki (1985). Low frequency unsteadiness was also observed in cavity flow (Rockwell & Naudascher 1979 and

Rockewell & Kinsely 1980), primarily caused by the feedback of disturbances from the impingement point up the shear layer.

In spite of the above investigations, many aspects of the low frequency behavior still remain largely unexplored and unexplained, especially in the context of bluff body wakes. A detailed three-dimensional description of the process is in particular lacking. Here we will present results from a well-resolved direct numerical simulation of flow past a normal plate at Re=250. Even at this modest Reynolds number, the drag and lift coefficients show a strong low frequency component and have a striking resemblance to the corresponding results at high Reynolds number for the normal plate (Najjar 1994 and Lisoski 1993) and for the circular cylinder (Schewe 1983). Thus the wake of a normal plate at Re=250 captures the essential features of low frequency unsteadiness without the added complexities of a highly turbulent flow in the wake. The present Re=250 flow is by no means simple or regular; it is reasonably complex to support low frequency unsteadiness, but simple enough to allow for detained investigation of the instantaneous and phase averaged vortical structures of the wake. Based on the simulation results, a simplified model of drag and lift variation is proposed. It is observed that the low frequency unsteadiness is primarily three-dimensional in nature and can be described as the process of flow periodically varying between two different states of three-dimensionality. These two three-dimensional states can be characterized by their coherence (or incoherence); the state of high mean drag is marked by reasonably regular spanwise and streamwise vortical structures, while the state of low mean drag is marked by spanwise vortices which are torn apart and an incoherent distribution streamwise vortices. A simple filter has been developed to separately identify the spanwise and streamwise vortical structures, which allows evaluation of their individual statistics. Based on which, the three-dimensional states are characterized.

The paper is organized as follows. A brief discussion of the simulation details will be presented in section 2. A detailed characterization of the low frequency behavior is presented in section 3. To facilitate discussion, two distinctly different shedding regimes are defined; one corresponds to high mean drag, while the other corresponds to low mean drag. The pressure and Reynolds stress distributions within these two regimes are discussed in section 4. The details of the Karman vortex formation and its dynamics within these two shedding regimes and their connection to the observed drag and lift behavior are addressed in section 5. A detailed discussion on the observed two different modes of three-dimensionality and statistics on spanwise and streamwise vortices in each of these modes is presented in section 6. Section 7 presents a discussion of the present results in the context of other relevant observations and

conjectures a possible physical mechanism for the observed low frequency behavior. Finally, section 8 presents a brief conclusion.

2. Computational Details

The time-dependent Navier-Stokes equations along with the incompressibility constraint are solved in three dimensions. All quantities are non-dimensionalized with the plate height (h_p) and the freestream velocity (U_∞) as the length and velocity scales (see Figure 1). Reynolds number is then the only non-dimensional parameter, defined as $\mathrm{Re} = h_p U_\infty / \nu$, where ν is the kinematic viscosity. The governing equations are discretized in time using a second-order accurate, time-splitting procedure. The convective and diffusive terms are represented by a fully-explicit Adams-Bashforth scheme. The time-splitting procedure is implemented by the following three steps: In the first step, an intermediate velocity field is calculated by solving the momentum equations without the contribution of the pressure gradient. In the next step, the pressure field is computed by solving a Poisson equation. In the final step, the divergence-free velocity field at the next time step is obtained by correcting the intermediate velocity field, with the computed pressure gradient. Although the explicit representation of the viscous terms requires a small time-step size at low Reynolds number, this restriction is somewhat eased at higher Reynolds numbers.

The spatial discretization is accomplished with a high-order accurate collocated finite-difference stencil. In the present formulation, a fifth-order upwind-biased finite difference scheme (Rai and Moin, 1991) is used to evaluate the convective term. The diffusion term is evaluated using a fourth-order accurate central difference scheme (Collatz, 1960). Fourth-order accuracy is maintained at the near-boundary grid points using asymmetric stencils. In the Pressure-Poisson equation, the gradient term, ∇p, is discretized with a fourth-order central difference stencil, while the divergence operator is formulated with a finite-volume scheme. A direct algorithm based on eigen-decomposition methodology (Haidvogel & Zang 1979 and Madabhushi, Balachandar & Vanka 1993) is used to solve the discretized Poisson equation. In the solution of the pressure Poisson equation, the presence of the normal plate inside the computational domain renders the Laplace operator non-separable. Here in the solution algorithm the Capacitance Matrix Technique (Buzbee et al., 1971; Schumann, 1980) has been incorporated for this purpose. A mixed spectral (Fourier) and high order finite-difference algorithm is invoked in the spanwise direction. Further details can be found in Najjar and Vanka (1995b), and Najjar (1994).

The computational domain extends from 5 non-dimensional units upstream of the normal plate in the streamwise direction (x) to 20 non-dimensional units in the downstream direction. In the cross-stream (y) direction the computational domain extends from $-L_y$ to $+L_y$, where $L_y = 8$. The spanwise width of the computational domain is chosen to be $L_z = 2\pi$. This choice of the spanwise extent for the computational domain was guided in part by the recent three-dimensional stability results of circular and square cylinders (Barkley & Henderson 1996, Williamson 1996 and Robichaux, Balachandar & Vanka 1997). As will be seen below, the present computational domain is large enough to accommodate from five to six pairs of three-dimensional streamwise vortical structures and therefore is adequate in resolving the spanwise flow variations. The present simulation at Re=250 employed a grid of 192x128x48 nodes along the streamwise, cross-stream and spanwise directions, respectively. In order to better resolve the near-wall flow features a smoothly varying nonuniform grid was used in the streamwise and cross-stream directions. A thorough investigation of the effects of domain size and grid resolution on the flow dynamics has been performed by Najjar (1994).

The following boundary conditions are applied along the edges of the computational domain: (i) At the inlet to the computational domain a uniform non-dimensional streamwise velocity of unity, and zero cross-stream and spanwise velocities are specified. Further, the normal gradient of pressure is set to zero in the solution of the pressure Poisson equation. (ii) At the top and bottom boundaries, freestream conditions ($u = 1$, $p = v = w = 0$) are imposed. (iii) At the outlet of the computational domain, a convective boundary condition is applied. A convective velocity of 0.8 was chosen a priori based on the experiments of Kiya and Matsumura (1988). This was subsequently found to agree well with the convective velocity inferred from the current simulation.

Results from a three-dimensional simulation at Re=250 will be reported. The time step size, Δt, is set to $4\text{x}10^{-3}$, which maintains the convective (CFL) and diffusive numbers under their respective stability limits. The three-dimensional computation was started from the corresponding two-dimensional result with a random spanwise perturbation applied to the streamwise velocity in the vicinity of the plate for a brief period of 250 time steps to drive the flow into a three-dimensional shedding state. The saturation of the three-dimensional mode has been monitored by following the volume-integrated streamwise vorticity magnitude ($\iiint |\omega_x| dx\,dy\,dz$), shown in figure 2. The transition to a three-dimensional flow is observed to occur after 80 non-dimensional units. The simulation was integrated further for up to 512 non-

dimensional time units. At this Re we observe an average shedding period of 6.5 non-dimensional time units, hence the present computation spans approximately 66 shedding cycles. The computations were performed on the massively parallel CM5 and the entire simulation required approximately 500 CPU hours on a 128 node partition. The pressure and three-dimensional velocity fields have been stored every hundred time steps (0.4 time units) thus providing approximately 16 flow dumps every shedding cycle. These dumps are processed *a-posteriori* to compute time and phase-averaged flow structures which will be discussed in detail in the following sections.

3. Shedding and Low Frequency Components of Drag and lift

3.1 Comparison of 2-D and 3-D Simulations

Figures 3a and 3b illustrate the temporal variation in the instantaneous drag coefficient, C_D, as computed from two and three-dimensional simulations, respectively. In the case of the three-dimensional simulation, the drag coefficient is based on the span-averaged drag force on the normal plate. As observed by many earlier investigators (for example, Najjar & Vanka 1995a, Mittal & Balachandar 1995a, Chua et al. 1990, Tamura, Ohta & Kuwahara 1990) the two-dimensional simulation considerably over-predicts the drag coefficient with a mean C_D of 3.36. The mean drag coefficient predicted by the three-dimensional simulation is 2.36. Thus, even at the present low Reynolds numbers of Re=250, restriction to two-dimensionality results in an approximate 42% overprediction of mean drag. The drag coefficient computed in the three-dimensional simulation is somewhat larger than the range of experimentally measured value of 1.8 to 2.15 (Fage & Johansen 1927, Abernathy 1962, Castro 1971, Arie & Rouse 1956 and Lisoski 1993). However, the Reynolds number of these experiments is generally much larger and furthermore if blockage effect due to the finite size of the computational domain is accounted for (Maskell 1963) then the corrected drag coefficient reduces and approaches the experimental measurements. Also note that inclusion of leakage effects in the experimental measurements can slightly increase the drag coefficient, as pointed out by Abernathy (1962).

The fundamental difference between the two and three-dimensional simulations is well brought in the corresponding instantaneous contours of spanwise vorticity (ω_z) shown in Figures 4a and 4b, respectively. In the case of the three-dimensional simulation, contours of the span-averaged spanwise vorticity are plotted on the x-y plane. Negative spanwise vorticity (dashed lines) corresponds to clockwise rotation of the vortices and positive vorticity (solid lines)

corresponds to counter-clockwise rotation. The first striking difference between the two snapshots is in the structure of the shear layers developing from the edges of the plate located at $y = \pm 1/2$ and x=0. In the three-dimensional simulation, the shear layer is seen to extend downstream up to two plate heights before roll-up into Karman vortices. In the two-dimensional result, the shear layers roll-up much closer to the plate. Further, in the three-dimensional simulation, the vortices can be seen to break-up into smaller vortices farther downstream for x>8. Whereas in the two-dimensional simulation the Karman vortices undergo no such break-up and they maintain their coherence. Distinct and strong vortices are observed to convect parallel to the centerline for some distance and then begin to interact with each other before being convected out of the computational domain (Najjar & Vanka 1995b). The absence of three-dimensionality in the form of vortex stretching and tilting preserves the form of these spanwise vortices without much distortion.

The compact vortices that form closer to the normal plate in the two-dimensional simulation are responsible for the higher suction pressure along the base and result in a significantly higher drag. This can be seen in figure 5, where the distribution of the mean pressure coefficient, $\overline{C}_p = \dfrac{2(\overline{p}^* - p_\infty^*)}{\rho U_\infty^2}$, based on the time and span-averaged dimensional pressure, $\overline{p}^*$, is plotted around the surface of the plate. In terms of the computed non-dimensional mean pressure distribution, $\overline{p}$, the pressure coefficient can be written as $\overline{C}_p = 2(\overline{p} - p_\infty)$. Also presented are the experimental data of Fage and Johansen (1927) and the computational results of Lisoski (1993) using the discrete vortex method. The current three-dimensional simulation compares well with the experimental data. Whereas, the two-dimensional as well as the discrete vortex simulations predict a significantly lower base pressure and do not capture the "flat" distribution of pressure on the back side of the plate. The near constant pressure in the base region, measured in the experiments is, however, well captured by the three-dimensional simulation. The non-uniform pressure distribution along the base and the higher suction have been observed in the two-dimensional simulation of other bluff body geometries as well (Mittal & Balachandar 1995a, Tamura et al. 1990).

In the two-dimensional simulation (figure 3a), the drag coefficient exhibits a dominant periodic time variation with a period of about 3.6 non-dimensional time units driven by the Karman vortex shedding process in the wake. This translates to a primary two-dimensional shedding period of 7.2, since the drag coefficient oscillates at twice the shedding frequency. Apart from this dominant frequency, a low-amplitude low frequency unsteadiness can also be

observed to be superimposed in the drag variation. This low frequency unsteadiness appears to occur with a period of about 10 times the fundamental period of drag variation or 5 times the period of the Karman vortex shedding process.

Oscillations at twice the shedding frequency can be observed in the instantaneous span-averaged drag signature of the three-dimensional simulation as well (see figure 3b); however, the amplitude of drag oscillation at this frequency is greatly diminished. The overprediction of fluctuation in the drag coefficient at twice the shedding frequency, observed in the two-dimensional simulation, is consistent with earlier findings in other bluff body geometries (Mittal & Balachandar 1995a). Plotted in figure 3c is the corresponding variation in the instantaneous span-averaged lift coefficient, C_L, computed in the three-dimensional simulation. For the normal plate, the lift force is solely due to the instantaneous viscous shear stress that acts on the front and back sides of the plate. The coefficient of lift can be expressed in terms of the non-dimensional spanwise vorticity distribution around the plate as $C_L = \frac{2}{\mathrm{Re}}\left[\int_{-1/2}^{1/2} (\omega_{z,Back} - \omega_{z,Front})\, dy\right]$, where $\omega_{z,Front}$ and $\omega_{z,Back}$ define spanwise vorticity on the front and back faces of the normal plate. The mean period of vortex shedding observed in the lift coefficient is T_p=6.2, corresponding to a primary shedding (or Strouhal) frequency of $F_p = 1/T_p$=0.16. Thus, restriction to two-dimensionality results in not only overprediction of the mean and fluctuating drag and lift forces, but also a 16% overprediction of the primary vortex shedding period.

The drag and lift coefficients reveal a strong component of unsteadiness at a much lower frequency with a long period of approximately ten times that of the main vortex shedding process. The nature of low frequency unsteadiness observed in the three-dimensional simulation appears to be significantly different from that observed in the two-dimensional simulation. First of all, the amplitude of low frequency unsteadiness in the three-dimensional simulation is much larger than that in the two-dimensional simulation. In fact, in the three-dimensional simulation the variation in drag coefficient is significantly stronger at the low frequency than at twice the shedding frequency. Whereas, the contrary is true in the two-dimensional result.

A three-dimensional simulation at a higher Reynolds number of Re=1000 also displays a similar strong low frequency component in the drag and lift signatures (Najjar & Vanka 1995a). It is important to point out that the temporal variation of drag and lift coefficients shown in figures 3b and 3c and observed in the higher Reynolds number simulation closely resembles the experimental measurements of C_D and C_L by Lisoski (1993). His measurements were also for

the case of a normal plate over a wide Reynolds number range from 1000 to 12,500. For the case of a circular cylinder, similar behavior for drag and lift coefficients can be observed in the experimental results of Schewe (1983) over a high Reynolds number range of 5×10^4 to 7×10^6 (see his figures 13 and 14). Similar low frequency unsteadiness has also been observed in the context of separating-and-reattaching flows (Eaton & Johnston 1982, Kiya & Sasaki 1983, 1985 and Cherry et al. 1984).

3.2 Characterization of Low Frequency Unsteadiness

Even at the modest Reynolds number of Re=250, the wake dynamics as predicted in the present three-dimensional simulation is sufficiently complex and the resulting drag and lift variations as shown in figures 3b and 3c are fairly irregular. However, the primary shedding and low frequency components appear to dominate the essentially chaotic behavior. In the case of the lift coefficient, C_L, its variation to first approximation can be adequately represented as a low frequency modulation of lift variation at the primary shedding frequency. The lift variation can then be approximately expressed as: $a_L \sin^2(\pi F_s t)\sin(2\pi F_p t + \phi_L)$, where ϕ_L is the phase angle between the primary shedding and low frequency modulation processes. Here a_L represents the amplitude of low frequency modulated lift variation. The *primary* shedding and *secondary* low frequencies are denoted by F_p and F_s, respectively (with appropriate subscripts "p" and "s").

In the case of the drag coefficient, a low frequency component can be clearly identified. The mean drag evaluated over each shedding cycle can be observed to vary between 2 to 3. Although not as clear as in the lift variation, a low frequency modulation of the drag coefficient can also be identified. The amplitude of drag variation over a shedding cycle is large when the mean drag is large (at t≈225, 250, 300 and 375), whereas when the mean drag is low, variation in drag coefficient over a shedding cycle is nearly absent (at t≈210, 275 and 350). The drag variation can be approximately expressed as: $\overline{C}_D + a_{D1}\sin^2(\pi F_s t)\sin(4\pi F_p t + \phi_D) - a_{D2}\cos(2\pi F_s t)$, where $\overline{C}_D$ is the time averaged mean drag coefficient and ϕ_D is the phase angle. Here a_{D1} and a_{D2} represent the amplitudes of contribution to the drag coefficient from the modulated shedding process and the low frequency unsteadiness, respectively. The amplitude of low frequency component, a_{D2}, is observed to be larger than the amplitude of modulated shedding process, a_{D1}. In comparison, in the two-dimensional simulation (figure 3a) the low frequency modulation of the shedding process is virtually non existent, and the low frequency contribution to drag coefficient is at a relatively low amplitude.

A careful examination of the drag and lift coefficients plotted in figures 3b and 3c shows that it is not only the amplitude but also the shedding frequency is significantly modulated by the low frequency unsteadiness. This frequency modulation is better evident in figure 6 which shows a close-up of the time history of drag and lift coefficients spanning 100 non-dimensional time units from t=412 to 512, covering approximately two low frequency periods. To quantify the amplitude and frequency modulations, the beginning of each Karman shedding cycle is arbitrarily defined by the local peak value of C_L. Thus shedding cycles are defined to extend between adjacent peaks in the lift coefficient. For each shedding cycle, the shedding period, T_p, the mean coefficients of drag and lift, $\overline{C}_D^{Sh}$ and $\overline{C}_L^{Sh}$, and amplitudes of drag and lift variation, a_D^{Sh} and a_L^{Sh}, are computed. The amplitudes of drag and lift variation are simply defined as half the difference between the maximum and minimum values of drag and lift coefficients, respectively, during that cycle.

In figure 6a also overlaid on the drag coefficient is a plot of $\overline{C}_D^{Sh}$ versus t, where time for each shedding cycle is taken to be at the mid point of the cycle. By definition, the time variation in C_D captured by $\overline{C}_D^{Sh}$ accounts for only the contribution to the drag coefficient from the low frequency component and the difference between C_D and $\overline{C}_D^{Sh}$ is due to the Karman vortex shedding process. Thus the temporal variation in $\overline{C}_D^{Sh}$ shows an approximate sinusoidal behavior arising from the low frequency unsteadiness, whose amplitude provides an estimate for a_{D2} to be about 0.5.

Each cycle of low frequency unsteadiness is arbitrarily defined to extend between two adjacent minimums of $\overline{C}_D^{Sh}$ (from one point of minimum $\overline{C}_D^{Sh}$ to the next). Based on this definition, at any time instance the corresponding phase during the low frequency cycle can be defined as:

$$\Phi = \cos^{-1}\left(\frac{2\left(\overline{C}_D^{Sh} - \overline{C}_D\right)}{\left(\overline{C}_{D,\max}^{Sh} - \overline{C}_{D,\min}^{Sh}\right)}\right). \qquad (1)$$

The time-averaged mean drag coefficient, $\overline{C}_D$=2.36, is also the average of $\overline{C}_D^{Sh}$ over many low frequency cycles. Further, $\overline{C}_{D,\min}^{Sh}$ and $\overline{C}_{D,\max}^{Sh}$ are the minimum and maximum of $\overline{C}_D^{Sh}$ and therefore the denominator is approximately given by $2a_{D2}$. With the above definition, the low frequency phase can be computed at any given time and it is in the range $0 \le \Phi \le 2\pi$. The low frequency phases, $\Phi = 0$ and 2π correspond to time instances of overall low drag ($\overline{C}_D^{Sh} \to \overline{C}_{D,\min}^{Sh}$), while $\Phi = \pi$ corresponds to instances of high drag ($\overline{C}_D^{Sh} \to \overline{C}_{D,\max}^{Sh}$).

The amplitude and frequency modulation of the shedding process by the low frequency unsteadiness can now be extracted by plotting the shedding period, T_p, and the amplitudes of drag and lift variation, a_D^{Sh} and a_L^{Sh}, over each shedding cycle against the corresponding phase, Φ, along the low frequency cycle. In figures 7a and 7b, a_D^{Sh} and a_L^{Sh}, for 47 different shedding cycles are plotted against the low frequency phase (computed from equation 1) at the mid point of the shedding cycle. Also plotted are the expected form of drag and lift coefficient modulation, $a_{D1}\sin^2(\Phi/2)$ and $a_L\sin^2(\Phi/2)$. The general agreement between the data points and the analytical expression is quite good. The amplitudes of drag and lift modulation can be estimated from these figures as a_{D1}=0.3 and a_L=0.12, respectively. Thus it can be seen that drag variation due to low frequency unsteadiness ($2a_{D2}$) is about 67% larger than drag variation due to the shedding process ($2a_{D1}$).

Figure 7c shows variation in the primary shedding frequency ($F_p=1/T_p$) against the corresponding low frequency phase for 47 shedding cycles. A general trend of higher shedding frequency (or lower shedding period) with increasing mean drag ($\Phi \rightarrow \pi$) can be identified. Extraction of an exact form for this frequency modulation is made difficult by the scatter in the plot, but significant variation in shedding frequency from about 0.12 to 0.18 can be observed. The data points in this figure are marked by four different symbols. Open squares indicate shedding cycles during which the mean drag was low, filled circles indicate shedding cycles during which the mean drag is on the rise, open triangles corresponds to cycles of high mean drag and finally filled squares correspond to cycles of decreasing mean drag (more precise classification will be provided below). In addition to the general trend of increasing shedding frequency with increasing phase (or mean drag), as indicated in the plot, a tendency towards hysteresis can also identified.

It must be cautioned that the above presented functional forms for the drag and lift coefficients are intended to serve only as a model, since the actual low frequency effect neither simply superposes nor simply modulates the Karman vortex shedding process. Significant nonlinear interaction exists between the mechanisms responsible for Karman vortex shedding and low frequency unsteadiness resulting in a chaotic wake dynamics. The complex nature of low frequency unsteadiness is clear from the fact that its period does not remain fixed. It can be observed that the low frequency period varies anywhere between 35 to 55 non-dimensional time units. Furthermore, the low frequency unsteadiness appears to be asymmetric, resulting in relatively longer duration of quiescence and low mean drag separated by comparatively shorter duration of intense vortex shedding and high mean drag. Such asymmetry in the low frequency

unsteadiness has originally been suggested by Eaton & Johnston (1982). Based on surface pressure measurements Kiya & Sasaki (1985) have estimated the time duration of low drag to extend nearly twice as large as that of high drag in a reattaching flow over a blunt plate. These observations are consistent with the behavior of drag coefficient shown in figure 3b. Thus the strength of the shedding process appears to influence the nature of low frequency unsteadiness as well. To fully explain the complex variation in drag and lift coefficients seen in figure 3b it is necessary to go beyond a simple coexistence of the shedding and low frequency processes and consider their nonlinear interaction.

3.3 High, Low and Transition Drag Regimes

A simple physical interpretation of the low frequency behavior seen in the drag and lift variations is that the flow periodically varies between two extreme states: an active state of strong vortex shedding marked by large amplitude oscillation in drag and lift and a weak vortex shedding state marked by low levels of drag and lift variation. Existence of such distinctly different shedding states has been previously inferred based on experimental measurements by Kiya & Sasaki (1985). As remarked above, the total duration of these states need not be equal and the frequency of Karman vortex shedding is significantly higher in the active state than in the relatively weaker state. In order to well understand these two significantly different states of vortex shedding and the process of periodic transition from one to the other, we first classify these states. Based on the close-up shown in figure 6, four different flow regimes have been identified as follows:

(i) The *High Drag Regime* (marked **H**) encompasses the time interval where the drag coefficient is large and the corresponding lift coefficient shows large fluctuation. In figure 6 this occurs over the following time intervals: t=413-419 and t =467-485.

(ii) The *Low Drag Regime* (marked **L**) represents the time interval where the drag coefficient is low with correspondingly low level of fluctuation in the lift coefficient. This regime is observed to occur for t=426-462 and t>492.

(iii) The *Transition Regimes* (marked **D** and **I**) represent the transition regions that link Regimes **H** and **L**. Regimes **D** and **I** represent regions with decreasing and increasing drag coefficient, respectively. In figure 6 the time frames during which these transitions occur are t=419-426, t=485-492 and t=462-467.

Autocorrelations of the drag and lift coefficients computed over the entire period are shown in figure 8. The shedding period of T_p=6.2 is well captured by the dominant peak in the

autocorrelation of lift, while the influence of shedding process is seen to have only a weak effect on the autocorrelation of drag. The dominant peak in the drag correlation corresponds to a low frequency period of T_s=65.5. Thus the low frequency unsteadiness of the wake is at about one tenth of the shedding frequency. This ratio between the shedding and low frequencies is in agreement with the experimental measurements of Lisoski (1993) for the flow over a normal plate and with the spectral simulation results of Henderson (1994) for flow over a circular cylinder. In the case of a separating-and-reattaching flow over a blunt flat plate Kiya & Sasaki (1985) observe a low frequency of 1/6th the shedding frequency. Other measurements (Roshko 1954, Tritton, 1959, Gerich & Eckelmann 1982, Williamson 1992 and Szepessy 1994) also place the low frequency to be about one tenth to one twentieth of the shedding frequency. Small undulations in the drag autocorrelation are due to oscillations in the drag coefficient at twice the shedding frequency. To illustrate the difference in shedding frequency between the *High* and *Low regimes*, the autocorrelation of lift within each of these regimes was computed. From the dominant peak it was seen that the average shedding period in the regimes **H** and **L** are about 5.96 and 7.0, respectively. The corresponding mean shedding frequencies are 0.167 and 0.143, respectively. These frequencies computed from the autocorrelation are in good agreement with the average frequencies of 0.162 and 0.148 estimated in regimes **H** and **L** from figure 7c. The corresponding average frequencies in the transition regimes **I** and **D** are 0.169 and 0.144. Thus there is about 20% variation in the shedding period over the low frequency cycle (see figure 7c). Similar large variation in the shedding period over a low frequency cycle has also been observed in the recent investigation of wake of a circular cylinder with free ends (Dauchy et al. 1997). The wide range of shedding frequency seen in figure 7c is consistent with other reported experimental measurements. For flow over a normal plate, the experimental and computational investigations of Fage & Johansen (1927), Abernathy (1962), Kiya & Arie (1980) and Lisoski (1993) report shedding frequency covering a wide range of from 1.2 to 1.6.

3.4 Streamwise Velocity Signature and its Autocorrelation

While global quantities such as drag and lift coefficients have clearly exhibited the presence of low frequency unsteadiness, it is important to assess its impact on velocity measurements at isolated points in the wake. Such velocity measurements in the wake are more common than drag and lift measurements. Therefore, it remains to be seen if the low frequency behavior can be inferred from the single point velocity signature. In figures 9a, 9b and 9c temporal variations of the streamwise velocity component measured at three different downstream points x=1, x=4 and x=8 are plotted. All three points are located at y=0.5 and z=π/2. Oscillation in the streamwise velocity component at the shedding frequency is quite clear in the immediate wake (x=1) and at x=8, whereas at the intermediate location of x=4 the streamwise velocity signature is far more

complex. Occasional large departures from the near periodic behavior can be seen as "glitches", which are most evident at x=8 for $t \approx 270-285$ and $t \approx 430-460$. As can be seen from figure 3b, these time intervals precisely coincide with regime **L**. While the signature of the low frequency unsteadiness is well evident at the downstream velocity probe at x=8, this behavior is not so evident in the other two near wake velocity signatures.

The corresponding autocorrelations of the streamwise velocity component are shown in figures 9d, 9e and 9f. At x=8 the most dominant peak in the autocorrelation corresponds to a shedding period of about 6.12 and the second most dominant peak corresponds to a low frequency period of about 65.56. Both these values are in good agreement with those obtained from the drag and lift coefficients. The near wake probe at x=1 extracts a reasonably consistent shedding period of about 6.44 and a low frequency period of about 65.48, even though the signature of the low frequency is not immediately apparent in the velocity signature. In spite of its complexity, the velocity signature at x=4 extracts a shedding period of about 6.96 and a longer period of about 65.68 can also be discerned. Hence, we believe that identification of the low frequency unsteadiness, if any, is possible based solely on hot-wire probes, especially with the use of autocorrelation. Furthermore, the low frequency unsteadiness is not just restricted to global measurements, it is a complex phenomenon experienced by the entire flow field. Based on their velocity and surface pressure measurements Kiya & Sasaki (1985) also make a similar observation that the low frequency unsteadiness is a global event felt everywhere within the recirculation bubble (and possible outside as well).

The "glitches" in the streamwise velocity seen in figure 9c are similar to those observed by Willamson (1992) in the case of a circular cylinder at around a non-dimensional downstream distance of $x \approx 10$. He pointed out that these glitches are associated with vortex dislocations which appear in the wake transition regime. Velocity measurements at a series of downstream locations from x=5 to x=40 showed that, while the shedding frequency dominates the velocity signature at x=10, the low frequency unsteadiness associated with the glitches dominate the spectrum farther downstream. It was also observed that the shedding frequency with and without vortex dislocations is different and that the shedding frequency decreases with the presence of dislocations (also see Williamson 1996). The difference in the shedding frequency between the high and low drag regimes observed in the present simulation is consistent with these results.

4. Pressure and Reynolds Stress Distributions in the Wake

The spatial distribution of time and span-averaged pressure coefficient within regimes **H** and **L** are presented in figures 10a and 10b, respectively. Also marked in the figures as thick lines are the boundaries of the mean recirculation region. The non-dimensional length of the recirculation region in the wake, defined as the distance from the base to the reattachment point (marked R in figure 10), is 1.70 and 3.13 in regimes **H** and **L** respectively. The corresponding half heights of the recirculation region (defined as the maximum cross-stream distance from the centerline to the periphery of the mean recirculation region) in regimes **H** and **L** are 0.72 and 0.92. The repeated shrinkage and expansion of the mean recirculation region as the flow state changes between regimes **H** and **L** are consistent with previous observations of significant oscillation in the reattachment point along the longitudinal direction (Kiya & Sasaki 1985, Eaton & Johnston 1982). The non-dimensional length and half height of the mean recirculation region computed over all the four regimes are 2.35 and 0.8, respectively. In comparison, the experimental measurements of Bradbury & Moss (1975) and Leder (1991) at much higher Reynolds numbers of Re = $2.6\text{x}10^4$ and $2.8\text{x}10^4$ reported a mean wake recirculation length of 1.92 and 2.50, respectively. The 2-D simulation predicts an extended mean recirculation region of length of 13.75. As explained by Najjar & Vanka (1995a) this is caused by the low-pressure wake region downstream of the normal flat plate that hinders the interaction of shed Karman vortices of alternating vorticity. Balachandar, Mittal & Najjar (1997) have summarized various experimental and computational results for the circular cylinder where the non-dimensional length of the mean recirculation region is observed to vary from 1.1 to 2.0. It is thus evident that the wake cavity length is significantly larger for the normal flat plate than for the circular cylinder as discussed in Balachandar et al. (1997).

The suction pressure in the wake is significantly higher in regime **H** than in regime **L**. For example the lowest pressure coefficient of about -3.0 is reached approximately at x=0.8 in regime **H**, while the pressure coefficient in regime **L** reaches only about -1.6 at around x=1.6. The significantly smaller mean wake bubble in region **H** is consistent with the higher suction pressure and the higher mean drag. The distributions of time and span-averaged pressure coefficient on the upstream and downstream faces of the normal flat plate computed separately in regimes **H** and **L** are also shown in figure 6. Regime **L** yields a near constant pressure coefficient value of -1.35 on the downstream face while Regime **H** results in a higher suction pressure coefficient of -2.1. The overall flow pattern falls between those of regimes **H** and **L**, leading to a base pressure coefficient of -1.63. In comparison, the 2-D computation predicts a

base pressure coefficient of -2.8. Thus the behavior of regime **H** is relatively closer to the two-dimensional simulation than regime **L**.

The non-dimensional Reynolds streamwise normal and shear stresses ($\overline{u'^2}$ and $\overline{u'v'}$) evaluated in regime **H** are plotted in figures 11a and 11b. The corresponding figures for regime **L** are shown in figures 11c and 11d. Here the overbar indicates an average over both time and span within regimes **H** and **L** and Reynolds stresses are computed based on streamwise and transverse velocity perturbations away from their respective time and span-averaged quantities ($u' = u - \overline{u}$ and $v' = v - \overline{v}$). Consistent with the smaller recirculation region, in regime **H** the Reynolds stresses are distributed in the wake close to the base of the normal plate. Whereas, in regime **L** the stresses are distributed farther away from the immediate base and in fact both the streamwise normal and shear stresses are nearly zero for x<0.75. The behavior of the cross-stream normal stress, $\overline{v'^2}$, (not shown here) is also similar in nature. The low level of Reynolds stresses in the near wake region for regime **L** suggests that here the shear layers are nearly two-dimensional and reasonably time independent. Both three-dimensionality and temporal variation contribute to velocity perturbation and therefore to Reynolds stresses. Therefore the delayed roll-up process contributes to Reynolds stress only away from the immediate wake of the normal plate. Furthermore, the Reynolds stresses in regime **H** are nearly 60% stronger than those in regime **L**.

Owing to the non-linearity of the Navier-Stokes equation, the time and span-averaged mean pressure distribution in the wake is dependent not only on the time and span-averaged mean flow field, but also on the level of perturbation through the Reynolds stresses. The pressure Poisson equation for the time and span-averaged pressure, $\overline{p}$, can be expressed as

$$\nabla^2 \overline{p} = -\left[\frac{\partial^2 \overline{u}^2}{\partial x^2} + 2\frac{\partial^2 \overline{u}\,\overline{v}}{\partial x \partial y} + \frac{\partial^2 \overline{v}^2}{\partial y^2}\right] - \left[\frac{\partial^2 \overline{u'^2}}{\partial x^2} + 2\frac{\partial^2 \overline{u'v'}}{\partial x \partial y} + \frac{\partial^2 \overline{v'^2}}{\partial y^2}\right] \qquad (2)$$

where the second term on the right hand side is the source term to $\overline{p}$ arising from the Reynolds stresses. It was shown in Mittal & Balachandar (1995a) that differences in the Reynolds stresses influence the mean pressure distribution more than changes in the time and span-averaged mean flow. Thus Reynolds stress distributions in the wake influence the drag force. The higher suction pressure and the significantly enhanced drag observed in regime **H** are directly related to the stronger Reynolds stresses observed in the immediate wake. The relation between the time and span-averaged mean pressure, $\overline{p}$, and the Reynolds stresses can also be explored in the context of a force balance around the mean wake recirculation region (Roshko 1993 and Balachandar et al. 1997). The net pressure force around the mean wake recirculation region must be balanced by

forces exerted by the shear and normal stresses. An increase in the stress level around the periphery of the mean recirculation region can result in an increase in the pressure differential between the base and the reattachment point. Significant contribution to the Reynolds stresses comes from the dynamics of the Karman vortices. Therefore the fundamental difference in the Karman vortex dynamics between regimes **H** and **L** will be explored below in the following section.

5. Karman Vortex Dynamics

5.1 Phase Average and Swirling Strength

In order to clearly identify the spanwise Karman and streamwise vortices and gain further insight on their dynamics, in this section we will first define the vortex identification technique employed here along with the necessary phase averaging technique. The spanwise and streamwise vortices are visualized by plotting contours of their *swirling strength*, λ_i, defined as the imaginary part of the complex eigenvalue of the velocity-gradient tensor, $\nabla\mathbf{u}$ (Dallmann *et al.* 1991, Chong, Perry & Cantwell 1990, Mittal & Balachandar, 1995b and Zhou *et al.* 1997). At spatial locations where all three eigenvalues are real, λ_i is set to zero. Positive λ_i indicates that locally vorticity dominates over strain and therefore correctly identifies vortical regions of local circular or spiraling streamlines. It thus avoids misinterpreting shear layers from rolled-up vortices. The swirling strength, λ_i, has the same dimension as vorticity (or velocity gradient), and in a purely vortical flow its magnitude is half of the local vorticity. This vortex identification procedure is applied to the full three-dimensional flow field and the corresponding three-dimensional swirling strength, denoted by $\lambda_{i,3D}$, simultaneously extracts both the spanwise and streamwise vortices.

To individually extract the spanwise and streamwise vortices we also employ the vortex identification procedure to velocity data on two-dimensional x-y, y-z and x-z planes (Zhang, Balachandar & Tafti 1997). The corresponding planar swirling strengths will be denoted as $\lambda_{i,xy}$, $\lambda_{i,yz}$ and $\lambda_{i,xz}$, respectively. The structure of spanwise Karman vortices is extracted from the x-y swirling strength, $\lambda_{i,xy}$, and will be denoted as $\lambda_{i,p}$ (to indicate primary vortex structure). This quantity is in general three-dimensional (dependent on x, y and z) due to distortions in the spanwise Karman vortices along the spanwise (z) direction. The streamwise vortices, also often referred to in literature as the streamwise ribs, that connect the adjacent spanwise Karman vortices are normally tilted in the x-y plane and are not purely oriented along the streamwise (x) direction. A combined measure of y-z and x-z swirling strengths as given by $\lambda_{i,s}=(\lambda^2_{i,yz}+\lambda^2_{i,xz})^{1/2}$ will be used to identify these vortices. Here, we will correctly refer to $\lambda_{i,s}$ as the cross-span

swirling strength or the secondary swirling strength (hence the subscript "s"). Whereas, for conformity, the cross-span vortices will be addressed by their commonly used terminology as the streamwise vortices or streamwise ribs.

In order to reduce the background fluctuations and enhance the Karman vortex dynamics, here we follow the phase averaging technique originally proposed by Reynolds & Hussain (1972) and Cantwell & Coles (1983) and apply it separately within the different regimes. The flow variables such as, $(\mathbf{u},p,\lambda)$, are considered to consist of three main components: a time and span-averaged mean $(\overline{\mathbf{u}},\overline{p},\overline{\lambda})$, a periodic $(\tilde{\mathbf{u}},\tilde{p},\tilde{\lambda})$, and a random component $(\hat{\mathbf{u}},\hat{p},\hat{\lambda})$ as follows: $(\mathbf{u},p,\lambda)=(\overline{\mathbf{u}},\overline{p},\overline{\lambda})+(\tilde{\mathbf{u}},\tilde{p},\tilde{\lambda})+(\hat{\mathbf{u}},\hat{p},\hat{\lambda})$. According to this definition the periodic component, which arises from the dominant shedding process, and the random component together contribute to the total perturbation away from the time and span-average (i.e., $(\mathbf{u}',p',\lambda')=(\tilde{\mathbf{u}},\tilde{p},\tilde{\lambda})+(\hat{\mathbf{u}},\hat{p},\hat{\lambda})$). The coherent component, also referred to as the phase-averaged component, denoted by $(\overline{\tilde{\mathbf{u}}},\overline{\tilde{p}},\overline{\tilde{\lambda}})$, is defined as the sum of the time and span-averaged and periodic parts as: $(\overline{\tilde{\mathbf{u}}},\overline{\tilde{p}},\overline{\tilde{\lambda}})=(\overline{\mathbf{u}},\overline{p},\overline{\lambda})+(\tilde{\mathbf{u}},\tilde{p},\tilde{\lambda})$.

In the present study, each shedding cycle, which is arbitrarily defined to start with a local peak in the lift coefficient and extend up to the next peak, is divided into 8 phases of equal extent each covering one eighth of the shedding cycle. All the three-dimensional data dumps are first sorted according to the four flow regimes: **H**, **L**, **D** and **I**, respectively. Within each regime the dumps are further sorted out into the eight phase bins, according to the time of the data dump (or the phase) within the shedding cycle. All data sets in a phase bin within each regime are averaged to obtain the phase-averaged or the coherent component. The phase averaging procedure also includes an average along the span and therefore the phase-averaged variables are two-dimensional and will be denoted by $[\overline{\tilde{\mathbf{u}}}]_k(x,y)$ or $[\overline{\tilde{\lambda}}]_k(x,y)$, where k=1, ..., 8 is the phase bin number. The large number of data sets considered in this study along with the limited number of phase bins, guarantee reasonably converged phase average within each bin.

5.2 Phase-Averaged Spanwise Swirling Strength

First, the evolution of the spanwise Karman vortices are followed separately in regimes **H** and **L**. Attention is focused on phase-averaged, coherent component of the spanwise swirling strength, $[\overline{\tilde{\lambda}}_{i,p}]_k$. Figures 12a-d present contours of $[\overline{\tilde{\lambda}}_{i,p}]_k$ for the first four phases (k=1-4) in regime **H**. This sequence covers one half of the shedding cycle and swirling strength for phases 5 through 8 can be obtained from the other four phases with appropriate symmetry about the

wake centerline of the following form: $[\overline{\tilde{\lambda}}_{i,p}]_k(x,y)=[\overline{\tilde{\lambda}}_{i,p}]_{k-4}(x,-y)$. Hence, the evolution of the Karman vortices over the entire shedding cycle can be followed. From figure 12 the separated shear layers are seen to roll-up and form new spanwise vortices very close to the flat plate within a region of x<1. The separation of the rolled-up vortices from the shear layers seems to be complete within two plate heights downstream of the normal plate (x<2). The coherence of the Karman vortices is maintained up to x=10 and beyond. The corresponding four phases in regime **L** are plotted in Figures 13a-d. Significant differences in the wake dynamics can be observed between regimes **H** and **L**. In regime **L** the roll-up of the separated shear layers appears to be complete only farther downstream for x>2 and correspondingly the vortex pinch-off from the shear layer is delayed to x≈3. This difference in the dynamics of the spanwise vortices clearly explain the shrinkage of the mean recirculation region from regime **L** to **H**.

Figure 14a presents the evolution of the coherent vortex core strength as it travels in the downstream direction for regimes **H** and **L**, measured in terms of the maximum magnitude of $\overline{\tilde{\lambda}}_{i,p}$ within the vortex core. Since vorticity is approximately twice the swirling strength, the peak vorticity magnitude in regimes **H** and **L** are approximately 8 and 3, respectively. Near the separation point (x~0) the initial strength of the Karman vortex in regime **H** is a factor of 2.5 higher than that in regime **L**. Although the spanwise vortices in regime **H** decay at a faster rate as they evolve downstream and appear to approach the strength of the corresponding vortices in regime **L**, even at x>15 the spanwise Karman vortices in regime **H** are nearly twice as strong as those in regime **L**. It must be stated in passing that the magnitude of phase-averaged $\lambda_{i,p}$ decays to about 25 to 30% of its initial value by around x=10 to 15 in both regimes **H** and **L**. This compares favorably with the experimentally measured fraction of initial circulation in the convected vortices in the region x=10 to 16 (60% by Fage & Johansen 1927, 43% by Roshko 1954, 30% by Bloor & Gerrard 1966 and 26% by Davies 1976).

The trajectories of the clockwise and counter-clockwise Karman vortex cores in the upper and lower halves of the x-y plane are plotted in figure 14b for regimes **H** and **L**. In both regimes the spanwise vortices evolve nearly parallel to the x-axis. The primary differences are that in regime **H** the vortices form closer to the plate and that they remain closer to the wake centerline. Also plotted in this figure are the centers of the time-averaged upper and lower shear layers, y_c, for both regimes **H** and **L**. Following the conventional definition used in mixing layers, y_c is defined as the transverse location at which the time and span-averaged streamwise velocity has a value of $0.67\Delta\overline{u}+\overline{u}_{min}$, where $\Delta\overline{u}=\overline{u}_{max}-\overline{u}_{min}$ is the velocity difference between the maximum velocity, $\overline{u}_{max}$, on the high-speed side and the minimum velocity, $\overline{u}_{min}$, on the low-

speed side. The position of the mean shear layers as well as the Karman vortex trajectories suggest that as the wake goes through the low frequency cycle, the shear layers will appear to undergo a transverse oscillation. Eaton & Johnson (1982) have conjectured such low frequency vertical oscillation of the shear layer. Experimental measurements by Kiya & Sasaki (1985) have confirmed the vertical oscillation of the shear layer but the amplitude of oscillation was observed to be only 2.5% of the blunt flat plate's thickness. Recent measurements in the shear layers of a circular cylinder (Prasad & Williamson 1997) have shown that the vertical motion of the shear layer is utmost 8% of the shear layer thickness, which itself is a small fraction of the cylinder diameter.

Interpretation of the shear layer center shown in figure 14b requires some caution. First of all, y_c is obtained from a mathematical definition based on the time-averaged flow, so one is able to obtain a value for y_c even downstream after the shear layers have rolled-up into Karman vortices. Although the difference in centers of the shear layers between regimes **H** and **L** at x=1 appears to be about 0.2, the roll-up of the shear layers in regime **H** occurs close to the plate, well upstream of x=1. For x<0.5, the shear layer centers in regimes **H** and **L** are apart by less than 10% of the plate height. This is still substantially larger than the vertical movement estimated by Prasad & Williamson (1997), which may be the result of differences in the geometry and the Reynolds number. Nevertheless, characterization of the low frequency unsteadiness as "shear layer flapping" (as sometimes done in the past) does not provide a complete description of the observed behavior. The forward and backward movement of the formation region is much more pronounced than the up and down motion of the shear layers. Of course these two movements are interrelated. Furthermore, as will be seen below, the low frequency unsteadiness has its origin in the three-dimensional state of the wake. Therefore here we will consistently adhere to the terminology "low frequency unsteadiness".

5.3 Connection to Drag and Lift Variation

The above observations on the dynamics of the spanwise Karman vortices in regimes **H** and **L** are completely consistent with the drag and lift variations reported in the earlier sections. First of all, the spanwise vortices in regime **H** are compact and they form close to the base of the normal plate and their dynamics is such that the resulting time and span-averaged mean wake recirculation region is small and compact (see figure 10a). On the other hand, the roll-up process is delayed in regime **L** resulting in an extended mean wake recirculation region. The periodic shedding of the strong compact spanwise vortices in regime **H** directly contributes to the enhanced Reynolds stress components in the immediate wake (see figure 11). On the other hand, in regime **L** the Reynolds stresses are weaker and are distributed farther away from the base,

consistent with the observed delayed vortex roll-up process. In section 4 it was shown that as a result of the enhanced Reynolds stresses in the immediate wake, the associated time and span-averaged mean pressure along the base is significantly lower in regime **H** than in regime **L**, contributing to significantly higher drag in regime **H** when compared to regime **L**. The periodic exchange between the shedding of strong compact Karman vortices of regime **H** and the weaker shedding process in regime **L** directly contributes towards the observed low frequency component of the drag coefficient. Owing to the symmetry of the wake about its centerline, the mean lift within each shedding cycle is constrained to be nearly zero. Thus there is no low frequency component superposed in the lift coefficient, as in the drag coefficient.

For the normal plate, the fluctuating lift force over each shedding cycle is due to the fluctuating viscous shear stress on the back side of the plate. The periodic shedding of strong compact clockwise and counter-clockwise Karman vortices in regime **H** directly translates to a large amplitude fluctuation in the lift coefficient over each shedding cycle. Whereas in regime **L**, the less compact Karman vortices shed farther away from the base have less of an impact on the viscous shear stress that acts on the back face of the normal flat plate. As a result, the variation in lift coefficient during the shedding process is weak in regime **L**. On the other hand, fluctuations in the drag force are due to oscillations in the pressure distribution around the normal plate, primarily at twice the shedding frequency. To see the connection between Karman vortex shedding and the pressure fluctuation a bit more clearly, consider the following Poisson equation (similar to equation 2) for the periodic part of pressure, $\tilde{p}$, as shown below:

$$\nabla^2 \tilde{p} \approx -2\left[\frac{\partial^2 \overline{u}\tilde{u}}{\partial x^2} + \frac{\partial^2 (\overline{u}\tilde{v} + \overline{v}\tilde{u})}{\partial x \partial y} + \frac{\partial^2 \overline{v}\tilde{u}}{\partial y^2}\right] - \left[\frac{\partial^2 u'^2}{\partial x^2} + 2\frac{\partial^2 u'v'}{\partial x \partial y} + \frac{\partial^2 v'^2}{\partial y^2}\right] \qquad (3)$$

It was shown in Mittal & Balachandar (1995a) that at moderate Reynolds numbers the incoherent contribution arising from the second term on the right hand side is negligible. The periodic part of pressure is therefore primarily from the coherent contribution (the first term on the right hand side) arising from the interaction between the time and span-averaged mean and the periodic part of the flow field. The strong compact vortices of regime **H** would thus correspond to large pressure fluctuations as well. As indicated in Mittal & Balachandar (1995a), although pressure fluctuates at the shedding frequency, its distribution around the normal plate at this frequency has a near front-back symmetry that it makes little contribution to drag. On the other hand, fluctuation in pressure at twice the shedding frequency is also strong and the pressure distribution at this frequency around the normal plate is such that it makes a strong contribution to drag variation. Owing to the weaker vortex shedding process in regime **L**, $\tilde{u}$ and

$\tilde{v}$ are generally smaller in magnitude and distributed farther away from the base. Based on this result, the near absence of drag variation during a shedding cycle in regime **L** can be justified.

Finally, there is ample evidence to suggest an inverse relation between the strength and coherence of the shed spanwise Karman vortices and the period at which they are shed. This also translates to an inverse relation between the length of the Karman vortex formation region (or the length of the mean wake recirculation region) and the frequency of shedding. For example, an increase in net circulation of the shed vortices with increasing Reynolds number, contributes to an increase in the shedding frequency. The shedding process can be considered to be the act of a newly forming spanwise vortex moving towards the centerline and cutting off the continued supply of vorticity to the earlier vortex of opposite sign from its shear layer. The movement of these vortices is in turn governed by their mutual induction. Thus with increasing strength of the spanwise vortices, their induced velocities increase, resulting in reduced shedding period and increased shedding frequency. This line of argument sufficiently explains the observed low frequency modulation of the shedding frequency.

Two distinct states of vortex shedding have also been observed by Kiya & Arie (1980) in their discrete vortex simulations of flow over a normal plate. Regimes **L** and **H** closely resemble their state I and state II vortex shedding. They observe that in state I, the separated shear layers extend farther downstream and result in a formation region of length 55% more than in state II. While in the present computation a continuous low frequency switching between regimes **H** and **L** is observed, in the discrete vortex simulations of Kiya & Arie (1980) state I (or regime **L**) was observed only during the initial transients of the computation. State I was generally observed to be unstable and give way to an eventual state II (or regime **H**) behavior. As we will see below, this may be an artifact of the two-dimensional limitation of their discrete vortex simulation. Nevertheless, many of the features of regimes **H** and **L** outlined above are in agreement with the observations of Kiya & Arie (1980). They observe the nondimensional shedding frequency to be approximately 0.25 in state II and 0.2 in state I. As pointed out by Kiya & Arie (1980), these values are somewhat larger, owing to the two-dimensional nature of the discrete vortex simulations, and do not quantitatively compare with the shedding frequencies of 0.162 and 0.14 for regimes **H** and **L**. But the qualitative trend remains the same in both simulations. Their time averaged C_D measured in state I was approximately 2.0, while state II yielded a much higher mean drag coefficient of about 3.0. Furthermore, consistent with the present observations, it can be seen in their time history of C_D that the drag variation over a shedding cycle in state I was negligible when compared to the strong cyclic variation in state II.

Interesting comparison can also be made with the behavior of wakes behind cylinders undergoing forced vibration. In the lock-in (or synchronized) regime, the formation length decreases systematically with increased amplitude of vibration of the cylinder (Griffin & Votaw 1972 and Griffin & Ramberg 1974). While the formation length is intimately related to the streamwise length of the mean recirculation region, the amplitude of vibration of the cylinder in the forced case plays an analogous role to the amplitude of drag and lift variation in the unforced wake. Furthermore, Griffin and coworkers observed that as the frequency of forcing is increased the scale of the formation region decreases. Thus the relation between the amplitude, frequency and the nature of vortex roll-up process observed in the present computation in regimes **H** and **L** appears to hold good even in case of forced wakes.

6. Distinct Modes of Three-Dimensionality

The above section clearly characterized the two different states of Karman vortex shedding in regimes **H** and **L**. In this section we will explore mechanisms responsible for these two distinct states of vortex shedding. The marked difference between the two-dimensional and three-dimensional simulation results, along with the absence of a strong low frequency component in the case of the two-dimensional simulation, suggests that the difference between regimes **H** and **L** has its root in their respective three-dimensional structure. Figure 15a shows a perspective view of the three-dimensional vortical structure in regime **H**, plotted in terms of an iso-surface of three-dimensional swirling strength, $\lambda_{i,3D}=1.0$. The flow is from left to right and the corresponding top and bottom views are shown in figures 15b and 15c. This instantaneous plot at t=416 corresponds to an instance in regime **H**. Marked in this figure are two generation of clockwise Karman vortices (CR0 and CR1) appearing from the top shear layer and three generation of counter-clockwise vortices (CCR0, CCR1 and CCR2) appearing from the bottom shear layer. Noticeable spanwise distortion is present even in the newly forming counter-clockwise rotating Karman vortex (CCR0), which is clearly visible in the bottom view. The distorted spanwise vortices are connected by streamwise vortices (or streamwise ribs). The spanwise extent of the computational domain is sufficiently wide enough to accommodate about five pairs of streamwise vortices in the near wake region (see section 7 for details).

The organization of spanwise and streamwise vortices in figure 15, although hardly perfect, is reasonably well structured, especially when compared to the corresponding three-dimensional structure in regime **L**. In figures 16a, 16b and 16c, the perspective, top and bottom views of an iso-surface of $\lambda_{i,3D}=1.0$ are shown at t=456 in regime **L**. This time instance corresponds to a point of minimum lift during regime **L**. The delayed roll-up of the spanwise Karman vortices is

evident. The counter-clockwise rotating spanwise vortex (CCR1) that has just detached from the bottom shear layer is seen to be torn apart in the spanwise direction. The detached clockwise vortex CR1 is in fact distorted to an extent that it can not be clearly identified. Many streamwise vortices can be identified but their size, shape and spatial organization are far more irregular. Some of the streamwise looking vortices appear to have their origin in the pieces of distorted spanwise vortices that are torn apart and tilted in the streamwise direction. The conversion of spanwise vorticity from the Karman vortex cores into streamwise vortices is at the heart of core and elliptic instability (Pierrehumbert & Widnall 1982, Corcos & Lin 1984, Waleffe 1990) and mode A instability of bluff body wakes (Williamson 1996). Similar scenario of large chunks of spanwise vorticity escaping from the core of Karman vortices to form streamwise vortices has previously been identified in the context of spanwise subharmonic instability and period doubling in the wake of a circular cylinder (Mittal & Balachandar 1995b).

Apart from the above two time instances, the three-dimensional vortex structure behind the normal plate was carefully analyzed at several other time instances as well. In addition to the three-dimensional visualization, the distribution of swirling strength (or vorticity) was examined systematically on a series of x-y and y-z planes, at the various time instances considered. The detailed structure of both the spanwise and streamwise vortices showed variability from shedding cycle to shedding cycle in both regimes **H** and **L**. Nevertheless, the following common features can be identified to be characteristic of regimes **H** and **L**. In regime **H** the Karman vortices undergo significant distortion in the spanwise direction, but generally remain distinct from the streamwise vortices. In each braid region between the Karman vortices, a finite number of streamwise vortices are seen, which remain coherent, concentrated and spatially compact. On the other hand, in regime **L** the spanwise vortices are torn apart and broad regions of streamwise vorticity can be identified. Although some compact streamwise vortices can be identified, the distribution of streamwise vorticity is in general diffused and not organized. In what follows the above observations will be quantified with appropriate statistics.

6.1 Span-Averaged Statistics

To separately quantify the spanwise and streamwise vortices active at the time instances shown in figures 15 and 16, the instantaneous velocity field was used to compute the corresponding spanwise and cross-span swirling strengths, $\lambda_{i,p}$ and $\lambda_{i,s}$. The span-averaged values of these two quantities, defined as

$$<\lambda_{i,p}>_z = \frac{1}{L_z}\int_0^{L_z} \lambda_{i,p}\, dz \quad \text{and} \quad <\lambda_{i,s}>_z = \frac{1}{L_z}\int_0^{L_z} \lambda_{i,s}\, dz, \tag{4}$$

are plotted in figures 17a and 17b. The size and position of the clockwise and counter-clockwise vortices, marked CR0, CCR0, CR1, CCR1, etc., in figure 17a are clearly representative of regime **H**. In figure 17b, the streamwise ribs connecting the spanwise vortices can be clearly seen and they are marked R0, R1, etc. By comparing figures 17a and 17b it can be observed that there are two distinct sources of cross-span swirling strength. Cross-span swirling strength is significant even in regions of spanwise swirling strength; the strong bending and distortion of the spanwise vortices result in conversion of part of the local spanwise vorticity into streamwise vorticity. The other source of streamwise vorticity is the streamwise ribs that connect the distorted spanwise vortices.

The corresponding span-averaged measures of spanwise and cross-span swirling strength corresponding to figure 16 of regime **L** are shown in figures 17c and 17d. To facilitate direct comparison, the contour levels are maintained the same in all the four plots. Consistent with the tearing of the spanwise vortices, in figure 17c, coherent spanwise vortices are not observed downstream of x=12. The plot of $\langle\lambda_{i,s}\rangle_z$ indicates a spatially distributed streamwise vorticity with only a weak resemblance to streamwise ribs connecting spanwise vortices. Based on these figures it is tempting to conclude that the streamwise vortex ribs are more active in regime **H** than in regime **L**. Such conclusion is not supported by the three-dimensional visualizations (figures 15 and 16), since significant streamwise rib activity is seen in both regimes **H** and **L**. The proper interpretation of figures 17b and 17d is that in regime **H**, the streamwise vortices are coherent along the spanwise direction to make significant contribution to the spanwise average. Whereas in regime **L**, the streamwise vortices, although nearly equally active, are not coherent along the spanwise direction and therefore do not make a unified contribution to the spanwise average.

6.2 Cross-stream (y-x) Plane-Averaged Statistics

In figure 18a the streamwise distribution of spanwise Karman vortex strength, measured in terms of the y-z plane-average of the spanwise swirling strength defined as:

$$\langle\lambda_{i,p}\rangle_{yz} = \frac{1}{2L_y L_z} \int_{-L_y}^{L_y} \int_{0}^{L_z} \lambda_{i,p}\, dy\, dz\,, \qquad (5)$$

is plotted for both regimes **H** and **L** corresponding to the two time instances shown in figures 15 and 16. The peaks correspond to the different clockwise and counter-clockwise rotating spanwise vortices. The presence of strong spanwise vortices in the immediate vicinity of the normal plate is clear in regime **H**. Whereas, for regime **L** the first significant peak occurs only at x≈2.5. The plots if scaled by the area of cross-section ($2L_yL_z$) provides the total spanwise

swirling strength at any streamwise location. Instead if the averaging procedure were to be restricted to only regions where spanwise vortices are present (i.e. regions where $\lambda_{i,p}>0$; note that outside the spanwise vortex $\lambda_{i,p}=0$) then one obtains the true intensity or the average concentration of swirling strength within the spanwise vortices. In other words, figure 18a needs to be inversely scaled by the fractional area, A_p, occupied by the spanwise Karman vortices in any y-z plane, which is defined as

$$A_p(x,t)=\frac{1}{2L_yL_z}\int_{-L_y}^{L_y}\int_{0}^{L_z} I_p(x,y,z,t)\,dy\,dz\,, \quad \text{where } I_p(x,y,z,t)=\begin{cases}1 & \text{if } \lambda_{i,p}>0\\ 0 & \text{if } \lambda_{i,p}=0\end{cases}. \qquad (6)$$

The resulting plots of $<\lambda_{i,p}>_{yz}/A_p$, shown in figure 18b for regimes **H** and **L**, are similar to those shown in figure 18a. The fractional area occupied by the spanwise vortices ranges from about 6% close to $x\approx0$, where the spanwise vortices are compact, to about 10% farther downstream, where the spanwise vortices are more diffused. As pointed out in section 5.1, in vorticity dominated regions the swirling strength is approximately half of local vorticity. So the counter-clockwise vortex (CCR0) seen in figure 17a to just form downstream of the normal plate is centered around x=0.5 and has an average non-dimensional vorticity concentration of about 5.0 at this streamwise location. The vorticity concentration at the subsequent downstream vortices decreases due to diffusive and dissipative processes. The dominant counter-clockwise vortex in regime **L** seen in figure 17c is centered around x=2.5 and the average vorticity concentration at this central streamwise location is only about 2.6.

In figure 18a the sharp peaks observed in regime **H** are indicative of the compactness of the spanwise vortices. In between the peaks, $<\lambda_{i,p}>_{yz}$ reaches near zero value, thereby clearly marking a well defined braid region in between the spanwise vortices. The distinction between the spanwise vortices and the interconnecting braid regions is somewhat less well defined in regime **L**, especially for x>10. Due to tearing and spreading, the spanwise vortices are more evenly spread along the streamwise direction without a strong peak-valley structure in $<\lambda_{i,p}>_{yz}$. In the near wake, the overall magnitude of the spanwise swirling strength is larger in regime **H** than in regime **L**. Whereas, the overall magnitude appears to be nearly the same farther downstream; the only difference is that the spanwise vorticity remains concentrated and focused into compact spanwise vortices in regime **H**, while it is more diffused in regime **L**. Thus some level of caution needs to be exercised in comparing figures 17a and 17c. Fewer contours farther downstream in figure 17c must correctly be interpreted as lack of coherence rather than lack of spanwise vorticity.

In figure 19 the distribution of cross-span swirling strength averaged over the entire y-z plane, defined as:

$$<\lambda_{i,s}>_{yz} = \frac{1}{2L_y L_z} \int_{-L_y}^{L_y} \int_{0}^{L_z} \lambda_{i,s}\, dy\, dz\,, \qquad (7)$$

is plotted for both regimes **H** and **L**, corresponding to the two time instances shown in figures 15 and 16. As pointed out earlier, these plots when scaled by $2L_yL_z$ provide the total cross-span swirling strength at any streamwise location. A comparison of the regimes **H** and **L** shows that if the entire streamwise direction is taken into account, the cross-span swirling strength is about the same in both regimes. It can be observed that in regime **H** the x locations of peaks in the cross-span swirling strength coincide with those of peaks in the spanwise swirling strength. This may at first seem surprising since the streamwise ribs are anticipated to be most active in the braid region between the spanwise vortices. As pointed out earlier with reference to figure 17b, the bending and distortion of the spanwise vortices also contribute to cross-span swirling strength. Although the concentration of swirling strength in the streamwise ribs is expected to be stronger, the streamwise ribs are spaced apart along the spanwise direction. Whereas, the distorted spanwise vortices occupy the entire spanwise extent. Thus the overall contribution of distorted spanwise vortices to the y-z plane-averaged cross-span swirling strength, $<\lambda_{i,s}>_{yz}$, is likely to be comparable to that from the streamwise ribs. The overlap of spanwise and cross-span swirling strengths can also be seen in regime **L**, but at a much reduced level since the spanwise vortices are torn apart and distributed along the streamwise direction.

6.3 Conditional Average of Cross-span Swirling Strength

In order to quantify the strength of the streamwise ribs, without the inclusion of the distorted spanwise vortices, in the following we will consider conditional average of cross-span swirling strength in regions outside the distorted spanwise vortices. In order to accomplish this, we first define a filter function $I_s(x,y,z,t)$, which will serve to isolate the streamwise ribs. The filter function will be simply defined as follows:

$$I_s(x,y,z,t) = \begin{cases} 1 & \text{if } \lambda_{i,s} > \lambda_{i,p} \text{ and } \lambda_{i,s} > 0 \\ 0 & \text{otherwise} \end{cases}. \qquad (8)$$

and $\lambda_{i,s}\, I_s$ will now be used to identify the streamwise ribs. In other words, the streamwise vortices are identified as regions of positive cross-span swirling strength greater than the local spanwise swirling strength. The need to separate the streamwise ribs from distorted spanwise vortices in their measurement of streamwise vorticity was originally identified by Hayakawa & Hussain (1989). In their case, the nature of experimental measurement and the higher Reynolds number required a complex set of conditions to filter the streamwise ribs. It will be shown below

that for the present case, the filter given in equation (8) will be sufficient to extract the streamwise ribs.

In figures 20a, 20b and 20c, contours of the three-dimensional swirling strength, $\lambda_{i,3D}$, unfiltered cross-span swirling strength, $\lambda_{i,s}$, and filtered cross-span swirling strength, $\lambda_{i,s} I_s$, are plotted on a y-z plane corresponding to the streamwise location x=1.5, for t=416 (regime **H**). From figures 17a and 17b, it can be seen that this plane primarily cuts through the streamwise ribs, R1, and the clockwise spanwise vortex CR0. In figure 20a the three-dimensional swirling strength can be seen to extract both the distorted spanwise vortex as well as the streamwise ribs which connect CR0 and CCR1. About ten streamwise vortices can be identified in this section. In the corresponding unfiltered cross-span swirling strength all of the streamwise vortices are still clearly extracted, but much of the spanwise vortex is eliminated. Some imprint of the distorted spanwise vortex can still be seen, in particular in regions where the spanwise vortex is tilted the most. Finally, in figure 20c the efficacy of the filter function (equation 8) can be observed. The filtered cross-span swirling strength, $\lambda_{i,s} I_s$, while retaining all the streamwise ribs intact, essentially removes all of the distorted spanwise vortex. Close examination of figures 17a and 17b, and also the three-dimensional visualization (figure 15), shows that the small patches of filtered cross-span swirling strength seen in figure 20c above the spanwise vortex at around y=0.6 are in fact related to the downstream tips of the newly forming streamwise ribs, R0.

Based on the filter function presented in equation (8), the following two quantities are defined:

$$< \lambda >_{rib} (x,t) = \frac{1}{2L_y L_z} \int_0^{L_z} \int_{-L_y}^{L_y} \lambda_{i,s}(x,y,z,t)\, I_s(x,y,z,t)\, dy\, dz \qquad (9a)$$

$$A_{rib}(x,t) = \frac{1}{2L_y L_z} \int_0^{L_z} \int_{-L_y}^{L_y} I_s(x,y,z,t)\, dy\, dz \qquad (9b)$$

where A_{rib} measures the fractional area on the y-z plane occupied by the streamwise ribs and $< \lambda >_{rib}$ measures the total swirling strength (inversely scaled by the area of the y-z plane, $2L_y L_z$) contained within the streamwise ribs at any streamwise location. $< \lambda >_{rib}$ and A_{rib} can further be averaged over many different time instances covering all phases during the shedding cycle, the resulting time averaged statistics, $(2L_y L_z \overline{< \lambda >_{rib}}^{t})$ and $\overline{A_{rib}}^{t}$, in regimes **H** and **L** are shown in figures 21a and 21b, respectively.

In the very near wake for x<2.5, the total strength of the streamwise ribs in regime **H** is higher than in regime **L**. This is understandable, since in regime **L** the fully rolled-up spanwise vortices form only farther downstream. In the intermediate region between x=2.5 to x=4, the total swirling strength of the streamwise ribs in regime **L** is about the same as that in regime **H**. Farther downstream, regime **H** surpasses again in the total strength of the streamwise ribs, possibly because of the fact that the highly dispersed streamwise ribs observed in regime **L** undergo faster decay as they evolve downstream. The plot of fractional area of the streamwise ribs shown in figure 21b is very informative. It clearly shows that in the near wake region, for x<3, the streamwise ribs in regime **L** have a larger cross-sectional area consistent with their lack of spatial compactness. Farther downstream, the fractional area gradually increases downstream in both regimes suggesting diffusion of streamwise vorticity, but the fractional area of the streamwise ribs in regime **H** becomes larger than that in regime **L**. The intensity or the average concentration of swirling strength within the streamwise ribs can be assessed by the following ratio: $(\overline{<\lambda>_{rib}}^{t} / \overline{A_{rib}}^{t})$, which is plotted for both the regimes in figure 21c. The strength of the streamwise ribs is seen to peak at x≈1.2 and x≈3.5 in regimes **H** and **L** respectively and decay downstream. Figure 21c can be compared to figure 18b to gauge the relative strength of the spanwise vortices and the streamwise ribs at any streamwise location. Note that figure 18b presents an instantaneous picture, while figure 21c also involves an average over time and therefore provides a time-averaged picture. In regime **L** the dominant peak in figure 18b is about the same magnitude as the peak seen figure 21c, suggesting that the spanwise and streamwise vortices are about the same average intensity. This result gives some support to the notion that in regime **L** the streamwise vortices have their origin in the distorted spanwise vortices. On the other hand, in regime **H** the peak intensity of the streamwise vortices (measured either in terms of swirling strength or in terms of vorticity) is about 60% of the dominant spanwise vortex.

7. Discussion

The characteristic three-dimensional vortex structure observed in regime **H** is in many ways similar to that of mode B three-dimensional instability (Williamson 1996, Barkley & Henderson 1996 and Mittal & Balachandar 1995c). Coherent streamwise vortices are observed and they appear to be distinct from the distorted spanwise vortices. An estimation of the average spanwise spacing between the streamwise ribs can be obtained from a two-point correlation of the filtered cross-span swirling strength, defined as:

$$R(\Delta y,\Delta z,t)=\frac{1}{2L_xL_yL_z}\int_0^{L_z}\int_{-L_y}^{L_y}\int_0^{L_x}\lambda_{i,s}(x,y,z,t)I_s(x,y,z,t)\lambda_{i,s}(x,y',z',t)I_s(x,y',z',t)\,dx\,dy\,dz \quad (10)$$

where $y' = y + \Delta y$ and $z' = z + \Delta z$. In figure 22 the two-point correlation computed as shown above is plotted for t=416 in regime **H**. Streamwise average is applied from 0 to $L_x = 2$. As can be expected there is a strong peak at $\Delta y = 0$ and $\Delta z = 0$. The second dominant peak occurs at a non-dimensional separation of $\Delta y \approx 0$ and $\Delta z \approx 0.6$, corresponding to a non-dimensional spanwise wavelength of about 1.2. This correlation peak is consistent with the five pairs of streamwise ribs seen in figures 15 and 20, which corresponds to a spanwise wave length of $L_z / 5 \approx 1.25$. This appears to be somewhat longer than the non-dimensional spanwise wavelength of the most amplified mode B disturbance for a circular cylinder, estimated from a Floquet stability analysis to be 0.82 (Barkley & Henderson 1996). On the other hand, for a square cylinder the most amplified spanwise wavelength is estimated to be about 1.2 (Robichaux, 1997, Robichaux, et al. 1997). Various experiments place the non-dimensional wavelength of mode B instability for a circular cylinder to be around 1.0 over a range of Reynolds number (Mansy, Yang & Williams 1994, Lin et al. 1995a, 1995b, Wu et al. 1994, Williamson 1996 and Chyu & Rockwell 1996). As can be seen from the y-z cross-sectional plots shown in figure 20, unlike in the instability modes, here the ribs are not perfectly aligned along the span. Nevertheless, the correlation correctly predicts an average zero vertical displacement between the streamwise ribs.

Circulation of the streamwise vortices can be computed based on figure 21 and compared with the experimental results for mode B shedding. From figure 21b, in regime **H** the fractional area occupied by all the streamwise vortices at $x \approx 1$, where their intensity reaches a peak, can be estimated to be 0.026, which corresponds to a total non-dimensional area of 2.6 (since $2L_y L_z \approx 100$). With an approximate count of ten streamwise vortices, the above estimate translates to an average non-dimensional diameter of 0.575 for the streamwise vortices. This is consistent with the cross-sectional plot shown in figure 20. Note that since the y-z plane does not pass normal to the streamwise vortices, the actual diameter and the area of cross-section of the streamwise vortices might be somewhat smaller. The cross-sectional size, along with the average cross-span swirling intensity of 1.7 at $x \approx 1$ (based on figure 21c), allows for an estimation of the streamwise circulation to be 0.28π. This estimate compares reasonably well with the PIV measurement of peak circulation to be 0.46π for the mode B streamwise ribs in the wake of a circular cylinder at Re=200 (Brede, Ecklemann & Rockwell 1996). Based on the above evidences it seems reasonable to consider regime **H** to be dominated by mode B three-dimensionality.

In contrast, the nature of three-dimensionality in regime **L** is far more complex. First of all some aspects of the streamwise rib structure resemble those of regime **H** and therefore mode B

three-dimensionality. On the other hand, the process by which the cores of the spanwise vortices undergo large scale deformation and become streamwise vortices is indicative of mode A instability (Williamson 1992). Mittal and Balachandar (1995b) have shown that the saturated state of mode B three-dimensionality can undergo spanwise subharmonic instability resulting in period doubling. In this subharmonic instability, substantial portion of the spanwise vortices tears away and gets stretched in the braid region to form hairpin like vortical structures. Certain aspects of this instability are also seen in regime **L**. But of more immediate relevance is the observation by Williamson (1992, 1996) that the wake transition regime, where mode A instability gives way to mode B instability, is marked by the coexistence of two different shedding frequencies. The higher shedding frequency is associated with a more regular three-dimensional state characterized by mode B instability, whereas, the lower shedding frequency is associated with large scale dislocations in conjunction with either mode A or mode B shedding (referred to as mode A* or B* by Williamson 1996). He also observed that in a natural wake the two frequencies do not coexist at one time, but the flow intermittently swaps between the lower and higher frequencies. Regular signals interspersed with periodic appearance of disturbed shedding cycles associated with spanwise phase incoherence has also been observed by Szepessy (1994). These observations are in total agreement with the behavior of regimes **H** and **L**.

It therefore appears that the low frequency unsteadiness can be characterized as the wake periodically switching back and forth between a reasonably well organized mode B-like three-dimensional regime and a disorganized, dispersed regime of three-dimensionality reminiscent of vortex dislocation. The key difference between these two regimes is in the level of vorticity diffusion. The importance of vorticity diffusion was also addressed by Kiya & Arie (1980). In their discrete vortex simulations vorticity diffusion was included as an external *ad hoc* parameter. They observed that as vorticity diffusion is increased the wake remained in state I (or regime **L**) for increasingly longer period after the start-up, but eventually transitioned to state II (or regime **H**). For sufficiently large diffusion the wake permanently stayed in state I. These results are in agreement with the present observations of coherent vs dispersed vortical structures in regimes **H** and **L**.

The appearance of a low frequency unsteadiness in the wake of a circular cylinder as a result of beating between closely related frequencies has been addressed by Tritton (1959), Gaster (1969, 1971), Gerich & Eckelmann (1982). By controlling the generating vortex dislocations with the interaction of two slightly different shedding frequencies, Williamson (1992) has observed that the dislocations can be made to occur at a regular rate and that the rate at which the dislocations are formed is determined by the beat frequency. In the present case, the average

frequencies in regimes **H** and **L** are computed to be 0.162 and 0.148, respectively (see section 3.3). This yields a beat frequency of 0.014, corresponding to a beat period of about 71.5, which compares reasonable well with the average low frequency period of about 65.5 (see figure 8). Of course, the above estimation of beat frequency is only approximate. As can be seen from figure 7c, there is no one single frequency that characterizes each of the regimes **H** and **L**; shedding frequency shows a continuous variation and falls over a wide range. The above estimation is only to suggest the possibility that the observed low frequency is the beat frequency of two closely related shedding frequencies. This possibility must however be explored for consistency with the various experimental and computational results.

Clear experimental evidence indicating the coexistence of two frequencies exists only over a limited range of wake transitional Reynolds number ($180<Re<260$) for the case of a circular cylinder (Williamson 1996). In a natural unforced wake above a Reynolds number of about 260 only a single shedding frequency has generally been reported. Recent computational results in this transitional regime (Re=225) suggest the presence of a low frequency (Belov et al. 1997). Three-dimensional numerical simulations at higher Reynolds numbers of Re=500 and 1000 (Henderson 1994) also display a low frequency behavior, but the amplitude of low frequency component seen in the drag and lift variations is significantly lower. Based on the above results for a circular cylinder it is tempting to conclude that the low frequency behavior is limited to a narrow window of Reynolds number in the wake transition regime. At much higher Reynolds number, experimental results by Schewe (1983) shows a very strong low frequency unsteadiness in the drag and lift coefficients.

For a normal plate, computational results indicate the presence of a strong low frequency component not only at the present modest Reynolds number of 250 (which is possibly in the wake transition regime), but also at a higher Reynolds number of 1000 (Najjar & Vanka 1995a). Furthermore, experimental results by Lisoski (1993) over a wide range of Reynolds number, from Re=1000 to 12,500, show a strong low frequency component in the drag and lift measurements, whose character is essentially the same as that observed in the present computational results. These results seem to indicate that the low frequency behavior is not just limited to a narrow Reynolds number window in the wake transition regime. While the model of beat frequency between mode B and the dislocation mode (A* or B*) seems to reasonably explain the observed low frequency unsteadiness at low Reynolds numbers, it is not entirely clear as to whether the same (or at least similar beat) mechanism is operational at higher Reynolds numbers as well. The striking resemblance between the drag and lift coefficients of the present case (figures 3b and 3c) and those of Lisoski (1993), Najjar & Vanka (1995a) and

Schewe (1983) lends support to the idea that the mechanism might remain the same over the entire range of Reynolds number. It then remains to be seen what two frequencies are responsible for the beat phenomenon at higher Reynolds numbers.

Next we shall consider possible physical mechanisms responsible for the periodic exchange of state between regimes **H** and **L**. The results of Rockwell & Naudascher (1979) and Rockwell & Kinsely (1980) for a cavity flow have shown that the low frequency unsteadiness has its origin in the feedback of signal from the reattachment point to the separating shear layers. Eaton & Johnston (1982) have suggested that the flow over a backward facing step is considerably more complex and that the low frequency unsteadiness is the consequence of an imbalance between the entrainment from the recirculation region along the shear layer and the reinjection of fluid near the reattachment point. The imbalance provides an adequate explanation for the observed expansion and shrinkage of the recirculation region and the experimental measurements of Kiya & Sasaki (1985) support this hypothesis.

Eaton & Johnston (1982) envisioned that an unusual event may trigger a temporary imbalance through a short-term breakdown in the spanwise vortices. The resulting decreased entrainment will lead to a temporary expansion of the recirculation region, which after a few shedding cycles will recover back to the original state. Kiya & Sasaki (1985) inferred from their detailed measurements that the low frequency unsteadiness is associated with repeated decrease and increase in the spanwise coherence of the Karman vortices. They further pointed out that the spanwise breakdown has a reasonably constant period and hence the feedback mechanism from the reattachment point to the separating shear layers proposed by Rockwell (1983) can not be discounted. Cherry et al. (1984) suggested that there are two different shedding phases and that the low frequency unsteadiness is related to the relaxation process governing the change over from one phase to the other. Finally, Szepessy (1994) observed that one possible explanation for the low frequency unsteadiness in the measured surface pressure correlation is the appearance of perturbed shedding cycles, which are marked by spanwise phase incoherence in the shedding process. He further stated that after perturbation from the regular vortex shedding, it takes a few cycles of more or less disturbed flow to build up the normal pressure oscillation associated with alternating vortex roll-up. All the above proposals are in reasonable agreement that the low frequency unsteadiness can be viewed as the wake oscillating between two different regimes (or states), which are marked respectively by enhanced and breakdown in spanwise coherence.

Further insight into low frequency unsteadiness can be obtained by exploring the alternative possibility of the flow establishing a near periodic state without oscillating back and forth

between two shedding regimes. Williamson (1992, 1996) has shown that by carefully controlling the cylinder end conditions, periodic occurrence of vortex dislocations can be avoided and a relatively periodic pure mode B shedding can be obtained in the experiments. Corresponding computations performed at moderate Reynolds numbers under controlled conditions (Henderson & Barkley 1996 and Mittal & Balachandar 1995c) show that a nonlinearly saturated state of mode B three-dimensionality is possible without any dislocations. This saturated state of mode B three-dimensional shedding is time periodic with period of oscillation only slightly different from that of the corresponding two-dimensional shedding and is devoid of any low frequency component. The primary question will then be why does the wake of a normal flat plate at Re=250 not establish a near periodic state in either regime **H** or regime **L**, but oscillate back and forth between the two regimes? In some sense, this question is intimately related to the origin of repeated appearance of breakdown in spanwise coherence of the spanwise vortices or perturbed shedding or vortex dislocations in a natural wake.

Mittal & Balachandar (1995c) have explored in detail the process by which streamwise ribs are autogenerated in mode B three-dimensional shedding and establish a periodic state. The previous generation mode B streamwise vortices are observed to distort the newly forming spanwise vortices, which in turn pass this information on and result in the formation of a new generation of streamwise vortices identical to the previous generation. This autogeneration process was observed to establish a delicate balance between the spanwise distortion of the spanwise Karman vortices and the strength and spanwise location of the streamwise vortices. Such balance is central to the periodic evolution of a three-dimensional wake without any low frequency component. This balance between the spanwise and streamwise vortical structures is intimately related to the balance between the entrainment and reinjection processes addressed by Eaton & Johnston (1982) and Kiya & Sasaki (1985).

A possible answer as to why low frequency unsteadiness is observed must lie in the inability of the spanwise Karman vortices and the associated three-dimensional streamwise vortex structure to establish a perfect balance in either regime **H** or in regime **L**. If such a balance were to be attained in the three-dimensional state characteristic of regime **H**, then a periodic evolution of the wake, much like the saturated state of mode B instability, would ensue. On the other hand, due to its disorganized nature, a perfect balance in regime **L** can not be expected; but the possibility of an approximate balance and a near-periodic state, without a dominant low-frequency component can not be ruled out. In order to explore this balance between the spanwise and streamwise vortices, in addition to regimes **H** and **L**, data dumps in the intermediate transition regimes **I** and **D**, where the mean drag increases and decreases respectively, were

analyzed as well. A simple qualitative characterization of the spanwise and streamwise vortices in these four regimes is shown below in table I.

Regime	Spanwise Vortices	Streamwise Vortices
L	Form farther from the base and are less coherent	Spatially Distributed
I	Form farther from the base and are less coherent	Organized
H	Form closer to the base and are compact and coherent	Organized
D	Form closer to the base and are compact and coherent	Spatially Distributed

Table I: Qualitative characterization of the spanwise and streamwise vortical structures in the different regimes of the low frequency cycle.

The above table serves to provide only a simple basic characterization of the spanwise and streamwise vortices. For example, it is not implied that the spanwise vortices are of the same strength in regimes **L** and **I** or that the ribs are of the same level of organization in regimes **I** and **H**, etc.

The picture to be drawn from the table is as follows: in regime **L** the spanwise and streamwise vortices are not coherent. The incoherency in the streamwise ribs arises from the tearing of spanwise vortices. Since spanwise vortices are weak in regime **L**, during subsequent evolution incoherency in the streamwise ribs decrease and they organize themselves in regime **I**. Whereas the spanwise vortices are still relatively weak and form farther from the base. The organized ribs of regime **I** are not nearly as strong and therefore subsequently generated spanwise vortices are not torn apart and they remain coherent. As a result, the spanwise vortices begin to roll-up closer to the normal plate initiating regime **H**. During regime **H**, the organized streamwise vortices also grow in strength. The older generation spanwise Karman vortices of regime **H** begin to tear apart and result in a state of incoherent streamwise vortices in regime **D**. The effect of the incoherent streamwise ribs is still not felt in the formation of the Karman vortices and therefore in regime **D** they still roll-up closer to the base. Finally the incoherent streamwise vortices weaken the spanwise vortices as well and the wake returns to regime **L**. This scenario implies that within each shedding cycle a perfect synchronization between the spanwise and streamwise vortices does not exist. Some imbalance or phase mismatch exists between their

generation mechanisms, which results in the low frequency unsteadiness. It must be cautioned that the above scenario is only a conjecture based on the detailed visualization at various stages during the shedding process. Even at the present modest Reynolds number of 250 the wake dynamics is far too complicated to extract a precise dynamical model. Future investigations under controlled conditions will hopefully shed light on the mechanistic details.

8. Conclusions

The wake behind a zero-thickness flat plate held normal to the flow at Re=250 is observed to exhibit a low frequency unsteadiness in addition to the primary shedding frequency corresponding to the Karman vortices. This mechanism is clearly evident in the time history of instantaneous span-averaged drag and lift coefficients. Autocorrelations of drag and lift coefficients reveal that the non-dimensional shedding (or Strouhal) and low frequencies are 0.16 and 0.015 respectively. Time history of single point velocity measurement reveals the shedding frequency, but the low frequency unsteadiness is not apparent in the velocity signals. On the other hand, autocorrelations of the velocity signal extract the low frequency behavior accurately. Thus, the low frequency unsteadiness is not just restricted to global measurements, it is a complex phenomenon experienced by the entire flow field.

In the case of the drag coefficient, a low frequency component is superposed on top of oscillations at twice the shedding frequency. During the low frequency cycle (or over roughly ten shedding cycles) the flow gradually switches back and forth between shedding cycles of high mean drag to shedding cycles of low mean drag. The high and low mean drag states of the wake are referred to as regime **H** and regime **L**. Owing to symmetry about the wake centerline, the mean lift within each shedding cycle remains nearly zero and therefore a noticeable low frequency component is not superposed on the time series of the lift coefficient. Instead, the low frequency modulates the lift variation at the shedding frequency. In other words, the peak-to-valley variation in lift coefficient during a shedding cycle is at its highest value in regime **H**, and is very low in regime **L**. This low frequency amplitude modulation can also be observed in the drag coefficient; large variation in drag coefficient over a shedding cycle occurs when the mean drag is high, while the variation in drag coefficient over a shedding cycle is virtually non-existent when the mean drag is low. Apart from the amplitude modulation, the low frequency unsteadiness modulates the shedding frequency as well. The shedding frequency increases from regime **L** to regime **H**, i.e. with increasing mean drag. Further, the variation in shedding frequency as flow goes from regime **L** to **H** seems to differ from its variation as the flow evolves from regime **H** to **L**, thus showing signs of hysteresis.

The spanwise Karman vortices evolve differently in regimes **H** and **L**. In the high drag regime, the spanwise vortices are compact and roll-up close to the back side of the normal plate. On the other hand, in regime **L** the spanwise vortices are less compact and their formation region extends farther away from the normal plate. As a result, the mean recirculation region in regime **H** is significantly shorter than that of regime **L**. The associated mean base suction pressure is higher in regime **H**, thus explaining the higher mean drag coefficient. The periodic generation of strong coherent spanwise vortices in the immediate wake of the plate in regime **H** translates to large amplitude variation in drag and lift coefficients over the shedding cycle. In contrast, the less coherent spanwise vortices of regime **L** forming farther downstream result in no significant variation in drag and lift coefficients. The significantly different dynamics of the spanwise vortices can also explain the observed frequency modulation.

Further, the three-dimensional structure of the wake is also significantly different between regimes **H** and **L**. In the high drag regime, reasonably well organized streamwise vortices (or ribs) are seen to extend in the braid region connecting the spanwise Karman vortices. The spanwise vortices are significantly distorted along the spanwise direction as a result of the strain field induced by the streamwise vortices. In spite of their mutual interaction, the spanwise and streamwise vortices are observed to be distinct and this state of three-dimensionality resembles the mode B shedding observed in circular and square cylinder wakes (Williamson 1996 and Robichaux et al. 1997). In the low drag regime, the spanwise vortices are seen to tear apart and large sections of spanwise vorticity enters into the braid region and gets tilted and stretched along the streamwise direction to form streamwise vortices. In addition, few mode B type streamwise vortices are also observed. In general the three-dimensional structure of the wake in regime **L** is highly incoherent and streamwise vorticity seems to be distributed over a larger region. This state of three-dimensionality resembles the large scale dislocation addressed by Williamson (1992, 1996).

It appears that the low frequency unsteadiness might be the result of a beat phenomenon arising from the interaction between the characteristic shedding frequencies in regime **H** and **L**. It is also noted that for a three-dimensional wake to establish a periodic state, a balanced interplay between the spanwise and streamwise vortices is required. The streamwise vortices distort the spanwise vortices along the spanwise direction and these distortions aid in the formation of next generation streamwise vortices (Mittal & Balachandar 1995c). Once this synchronized evolution is established with a perfect balance between the spanwise and streamwise vortices, the shedding cycle can continue for a long time without any low frequency

component. In contrast to this scenario, here based on detailed visualization of flow structures we conjecture that the formation of streamwise and spanwise vortices is not in perfect synchronization and as a result of this imbalance (or phase mismatch) the wake undergoes a low frequency cycle. Further investigation is needed to verify this conjecture.

Acknowledgments

This work was supported jointly through a Post-doctoral fellowship from the Division of Advanced Scientific Computing (DASC) at the National Science Foundation and the National Center for Supercomputing Applications. The calculations were performed on the Thinking Machines CM-5 at the National Center for Supercomputing Applications (NCSA) at the University of Illinois, Urbana-Champaign. The support of these organizations is gratefully acknowledged. FMN would like to acknowledge Prof. Vanka for his continuous guidance and initial motivation in bluff body wakes and Dr. D.K. Tafti for his support.

References

Abernathy, F.H. 1962 Flow over an inclined plate. *ASME J. Basic. Eng.* **61**, WA-124.

Arie, M. & Rouse, H. 1956 Experiments on two-dimensional flow over a normal wall. *J. Fluid Mech.* **1**, 129.

Balachandar, S., Mittal, R. & Najjar, F.M. 1997 Properties of the mean wake recirculation region in the wakes of two-dimensional bluff bodies. to appear in *J. Fluid Mech.*

Barkley, D. & Henderson, R. 1996 Three-dimensional Floquet stability analysis of the wake of a circular cylinder. *J. Fluid Mech.* **322**, 215.

Belov, A., Jameson, A. & Martinelli, L. 1997 Three-dimensional unsteady compressible flow calculations using multigrid. *AIAA* **97-0443**, 35th Aerospace Sciences Meeting and Exhibit, Reno, NV.

Berger, E. 1964 Bestimmung der hydrodynamischen Groessen einer Karmanschen wirbelstarsse aus hitzdrahtmessungen bei kleinen Reynoldsschen zahlen. *Z. Flugwiss.* **12**, 41.

Bloor, M.S. & Gerrard, J.H. 1966 Measurements on turbulent vortices in a cylinder wake. *Proc. R. Soc. Lond.* A **294**, 319.

Bradbury, L.J.S. & Moss, W.D. 1975 Pulsed wire anemometer measurements in the flow past a normal flat plate in a uniform flow and in a sheared flow. *Proc. 4th Int. Conf. Wind Effects on Building and Structures*, London, 485.

Brede, M., Ecklemann, H. & Rockwell, D. 1996 On secondary vortices in the cylinder wake. *Phys. Fluids* **8**, 2117.

Buzbee, B.L., Dorr, F.W., George, J.A. & Golub, G.H. 1971 The direct solution of the discrete poisson equation on irregular regions. *SIAM J. Numer. Anal.* **8**, 722.

Cantwell, B. & Coles, D. 1983 An experimental study of entrainment and transport in the near wake of circular cylinder. *J. Fluid Mech.* **136**, 321.

Castro, I.P. 1971 Wake characteristics of two-dimensional perforated plates normal to an air-stream. *J. Fluid Mech.* **46**, 599.

Castro, I.P. & Jones, J.M. 1987 Studies in numerical computations of recirculating flows. *Int. J. Num. Meth. Fluids* **7**, 793.

Cherry, N.J., Hillier, R. & Latour, M.P. 1984 Unsteady measurements in a separated and reattaching flow. *J. Fluid Mech.* **144**, 13.

Chong, M.S., Perry, A.E. & Cantwell, B.J. 1990 A general classification of three-dimensional flow fields. *Phys Fluids* **2**, 765.

Chua, K., Lisoski, D., Leonard, A. & Roshko, A. 1990 A numerical and experimental investigation of separated flow past an oscillating flat plate. *ASME Non-Steady Flow Symposium*, FED **92**, Toronto, Canada, 455.

Chyu, C. & Rockwell, D. 1996 Evolution of patterns of streamwise vorticity in the turbulent near wake of a circular cylinder. *J. Fluid Mech.* **320**, 117.

Collatz, L. 1960 *The Numerical Treatment of Differential Equations*. Springer-Verlag, Berlin.

Corcos, G.M. & Lin, S.J. 1984 The mixing layer: deterministic models of turbulent flow. Part 2. The origin of three-dimensional motion. *J. Fluid Mech.* **139**, 67.

Dallman, U., Hilgenstock, A., Riedelbauch, S., Schulte-Werning. B. & Vollmers, H. 1991 On the footprints of three-dimensional separated flows around blunt bodies. *AGARD CP-***494**.

Dauchy, C., Dusek, J. & Fraunie, P. 1997 Primary and secondary instabilities in the wake of a cylinder with free ends. *J. Fluid Mech.* **332**, 295.

Davies, M.E. 1976 A comparison of the wake structure of a stationary and oscillating bluff body, using a conditional averaging technique. *J. Fluid Mech.* **75**, 209.

Eaton, J. K. & Johnston, J. P. 1982 Low frequency unsteadyness of a reattaching turbulent shear layer. In *Turbulent Shear Flows* (ed: L.J.S. Bradbury, F. Durst, B.E. Launder, F.W. Schmidt & J.H. Whitelaw), Springer-Verlag, New York, 162.

Fage, A. & Johansen, F.C. 1927 On the flow of air behind an inclined flat plate of infinite span. *British Aero. Res. Coun. Rep. Memo.* **1104**, 81.

Gaster, M. 1969 Vortex shedding from slender cones at low Reynolds numbers. *J. Fluid Mech.* **38**, 565.

Gaster, M. 1971 Vortex shedding from circular cylinders at low Reynolds numbers. *J. Fluid Mech.* **46**, 749.

Gerich, D. & Eckelmann, H. 1982 Influence of end plates and free ends on the shedding frequency of circular cylinders. *J. Fluid Mech.* **122**, 109.

Griffin, O.M. & Votaw, C.W. 1972 The vortex street in the wake of a vibrating cylinder. *J. Fluid Mech.* **66**, 553.

Griffin, O.M. & Ramberg, S.E. 1974 The vortex street wakes of vibrating cylinders. *J. Fluid Mech.* **66**, 553.

Haidvogel, D.B. & Zang, T. 1979 The accurate solution of Poisson's equation by expansion in Chebyshev polynomials. *J. Comp. Phys.* **30**, 167.

Hayakawa, M. & Hussain, F. 1989 Three-dimensionality of organized structures in a plane turbulent wake. *J. Fluid Mech.* **206**, 375.

Henderson, R. 1994 Unstructured spectral element methods: parallel algorithms and simulations. Ph.D. Thesis, Princeton University.

Henderson, R. & Barkley, D. 1996 Secondary instability in the wake of a circular cylinder. *Phys. Fluids* **8**, 1683.

Joshi, D.S., Vanka, S.P. & Tafti, D.K. 1994 Large eddy simulation of the wake of a normal flat plate. *Boundary Layer and Free Shear Flows*, FED **184**, 231.

Karniadakis, G.E. & Triantafyllou, G.E. 1992 Three-dimensional dynamics and transition to turbulence in the wake of bluff objects. *J. Fluid Mech.* **238**, 1.

Kiya, M. & Arie, M. 1980 Discrete-vortex simulation of unsteady flow behind a nearly normal plate. *Bull. JSME* **23**, 1451.

Kiya, M. & Matsumura, M. 1988 Incoherent turbulence structure in the near wake of a normal plat. *J. Fluid Mech.* **190**, 343.

Kiya, M. & Sasaki, K. 1983 Structure of a turbulent separation bubble. *J. Fluid Mech.* **137**, 83.

Kiya, M. & Sasaki, K. 1985 Structure of large-scale vortices and unsteady reverse flow in the reattaching zone of a turbulent separation bubble. *J. Fluid Mech.* **154**, 463.

Kuwahara, K. 1973 Numerical study of flow past an inclined flat plate by an inviscid model. *J. Phys. Soc. Japan* **35**, 1545.

Leder, A. 1991 Dynamics of fluid mixing in separated flow. *Phys. Fluids* **3**, 1741.

Lin, J.-C., Towfighi, J. & Rockwell, D. 1995a Instantaneous structure of near-wake of a cylinder: on the effect of Reynolds number. *J. Fluids Struct.* **9**, 409.

Lin, J.-C., Vorobieff, P. & Rockwell, D. 1995b Three-dimensional patterns of streamwise vorticity in the turbulent near-wake of a cylinder, *J. Fluids Struct.* **9**, 231.

Lisoski, D. 1993 Nominally two-dimensional flow about a normal flat plate. Ph.D. Thesis, California Institute of Technology, Pasadena, California.

Madabhushi, R.K., Balachandar, S. & Vanka, S.P. 1993 A divergence-free Chebyshev collocation procedure for incompressible flows with two non-periodic directions. *J. Comp. Phys.* **105**, 199.

Mansy, H., Yang, P.-M. & Williams, D.R. 1994 Quantitative measurements of three-dimensional structures in the wake of a circular cylinder. *J. Fluid Mech.* **270**, 277.

Maskell, E.C. 1963 A theory of the blockage effects on bluff bodies and stalled wings in a closed wind tunnel. *Aero. Res. Comm. Rep. & Memo* **3400**.

Mittal, R. & Balachandar, S. 1995a Effect of three-dimensionality on the lift and drag of nominally two-dimensional cylinders. *Phys. Fluids* **7**, 1841.

Mittal, R. & Balachandar, S. 1995b Generation of streamwise vortical structure in bluff body wakes. *Phys. Rev. Lett.* **75**, 1300.

Mittal, R. & Balachandar, S. 1995c Autogeneration of three-dimensional vortical structures in the near wake of a circular cylinder. *TAM Report* **812**, University of Illinois, Urbana-Champaign.

Najjar, F.M. 1994 Direct numerical simulations of separated and separated-reattaching flows on massively parallel processing computers. Ph. D. Thesis, University of Illinois at Urbana-Champaign.

Najjar, F.M. & Balachandar, S. 1996 Transition dynamics in the wake of a normal flat plate. *Bull. Amer. Phys. Soc., 49th Annual Meeting Division of Fluid Dynamics* **41**, 1715.

Najjar, F.M. & Vanka, S.P. 1995a Effects of intrinsic three-dimensionality on the drag characteristics of a normal flat plate. *Phys. Fluids* **7**, 2516.

Najjar, F.M. & Vanka, S.P. 1995b Simulations of the unsteady separated flow past a normal flat plate. *Int. J. Num. Meth. Fluids* **21**, 525.

Perry, A.E. & Steiner, T.R. 1987 Large-scale vortex structures in turbulent wakes behind bluff bodies. Part I Vortex formation processes. *J. Fluid Mech.* **174**, 233.

Pierrehumbert, R. & Windall, S. 1982 The two- and three-dimensional instabilities of a spatially periodic shear layer. *J. Fluid Mech.* **114**, 59.

Prasad, A. & Williamson, C.H.K. 1997 The instability of the shear layer separating from a bluff body. *J. Fluid Mech.* **333**, 375.

Rai, M.M. & Moin, P. 1991 Direct simulations of turbulent flow using finite-difference schemes. *J. Comp. Phys.* **96**, 15.

Reynolds, W.C. & Hussain, A.K.M.F. 1972 The mechanisms of an organized wave in turbulent shear flow. Part 3. Theoretical models and comparisons with experiments. *J. Fluid Mech.* **54**, 263.

Robichaux, J. 1997 Ph.D. thesis, University of Illinois at Urbana-Champaign.

Robichaux, J., Balachandar, S. & Vanka, S.P. 1997 Three-dimensional instability of the wake of a square cylinder. To be submitted to *Phys. Fluids.*

Rockwell, D. 1983 Oscillations of impinging shear layers. *AIAA J.* **21**, 645.

Rockwell, D. & Knisely, C. 1980 Vortex edge interaction mechanisms for generating low-frequency components. *Phys. Fluids* **23**, 239.

Rockwell, D. & Naudscher, E. 1979 Self-sustained oscillations of impinging free shear layers. *Annu. Rev. Fluid Mech.* **11**, 67.

Roshko, A. 1954 On the drag and shedding frequency of two-dimensional bluff bodies. *NACA Tech. Note* **3169**.

Roshko, A. 1993 Perspectives on bluff body aerodynamics. *J. Wind Eng. Ind. Aero.* **49**, 79.

Schewe, G. 1983 On the force fluctuations acting on a circular cylinder in crossflow from subcritical up to transcritical Reynolds numbers. *J. Fluid Mech.* **133**, 265.

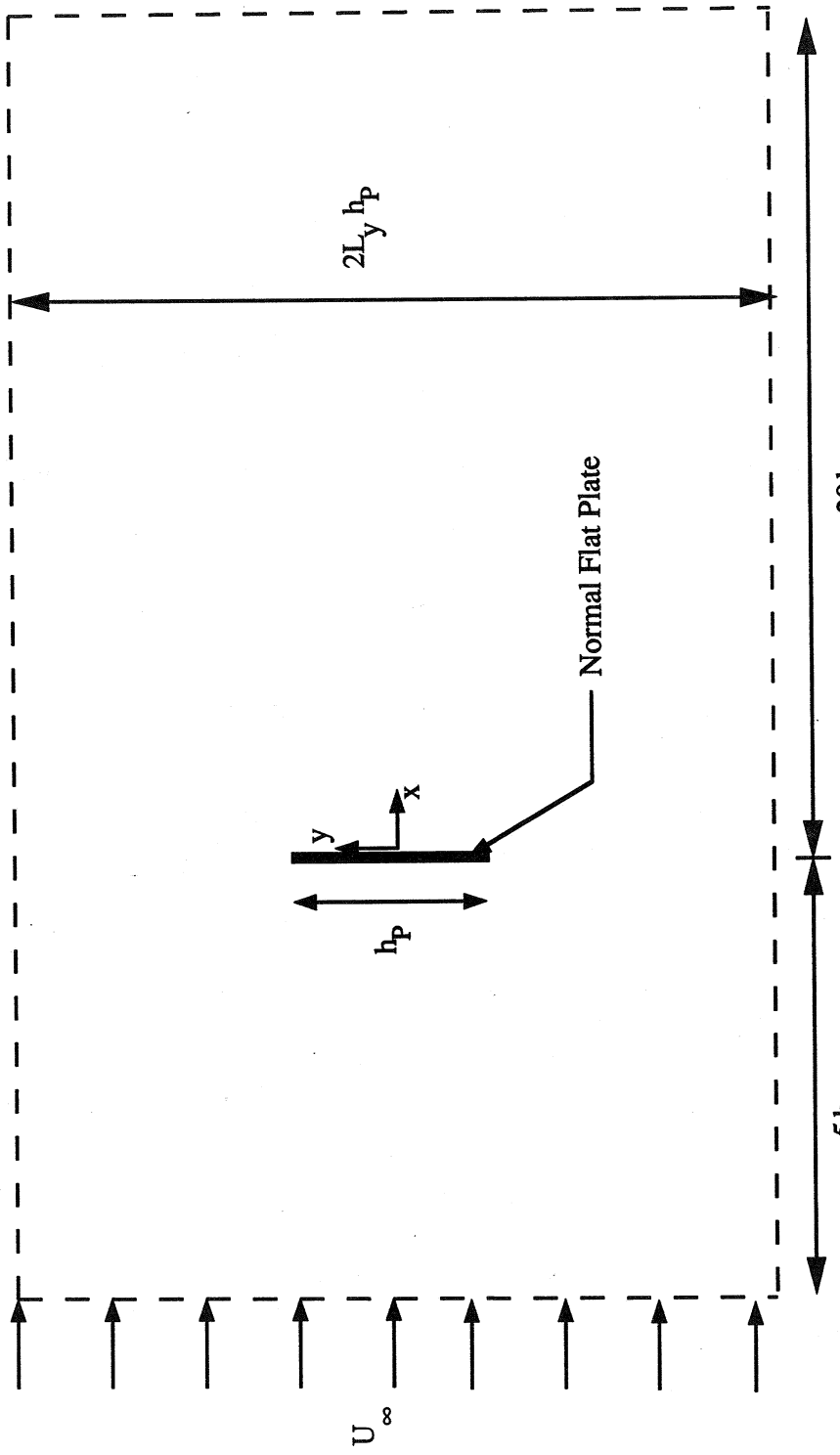

Figure 1.

Figure 1. Schematic showing the normal flat plate and the extent of the computational domain. The origin of the coordinate system is fixed on the plate. The *x*-axis represents the downstream direction, the *y*-axis is cross-stream to the flow , and the *z*-axis is along the plate axis. The *x*-*y* grid resolution consists of 192x128 nodes. The mesh resolution in the spanwise direction is 48 nodes with a grid size of $2\pi/48 = 0.13$.

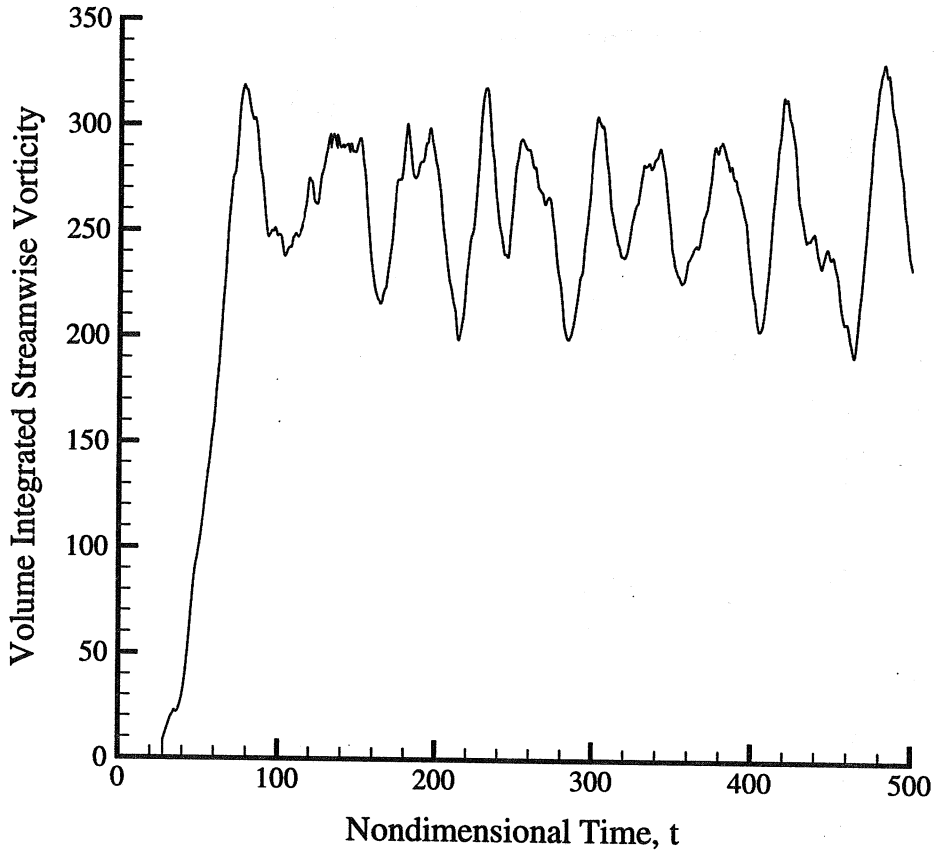

Figure 2. Transition from a two-dimensional flow to a three-dimensional flow is monitored with the temporal signature of the volume-integrated streamwise vorticity magnitude, $\iiint |\omega_x| dx\,dy\,dz$. The flow is fully three-dimensional by about t=100.

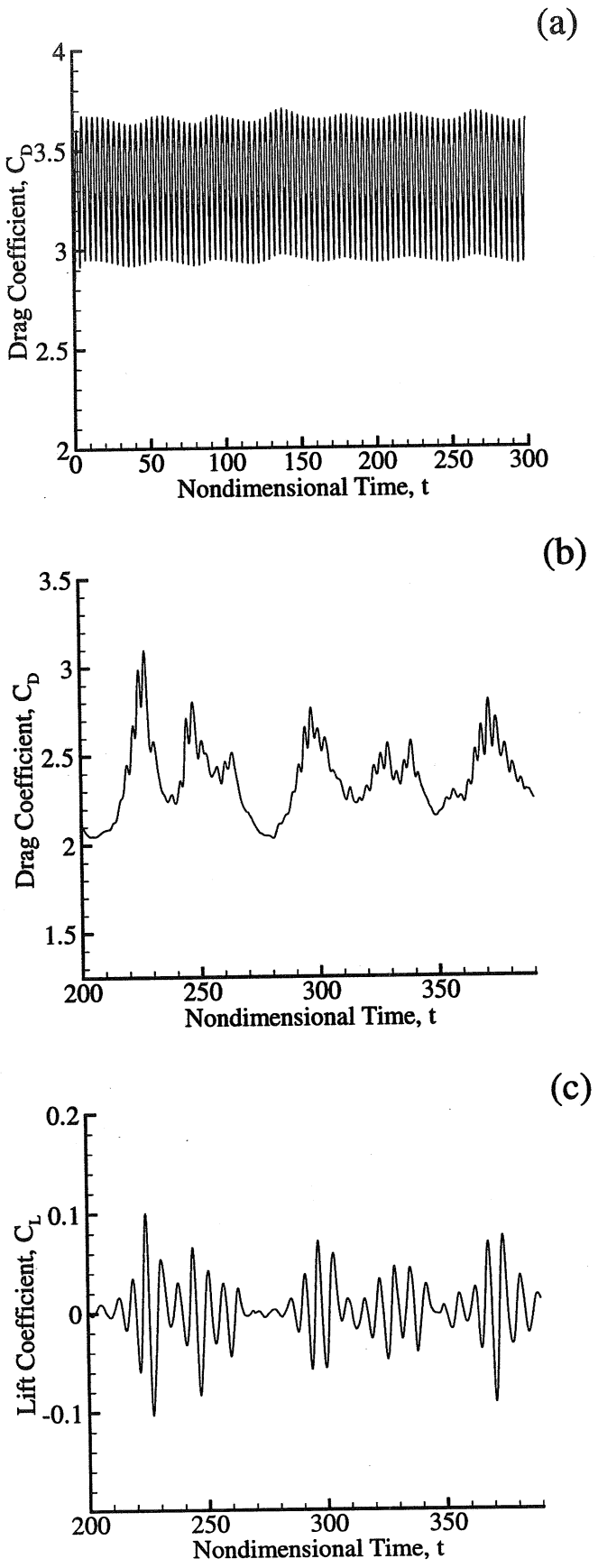

Figure 3. Time variation of the drag coefficient obtained from (a) 2-D simulation, (b) 3-D simulation and (c) lift coefficient computed from 3-D simulation. The drag coefficient oscillates at twice the Karman shedding frequency. The two-dimensional simulation captures a periodic drag variation with a primary non-dimensional shedding period of 3.6. The shedding period obtained in the three-dimensional simulation is about 6.2. Also can be seen in the three-dimensional simulation is a strong low frequency unsteadiness.

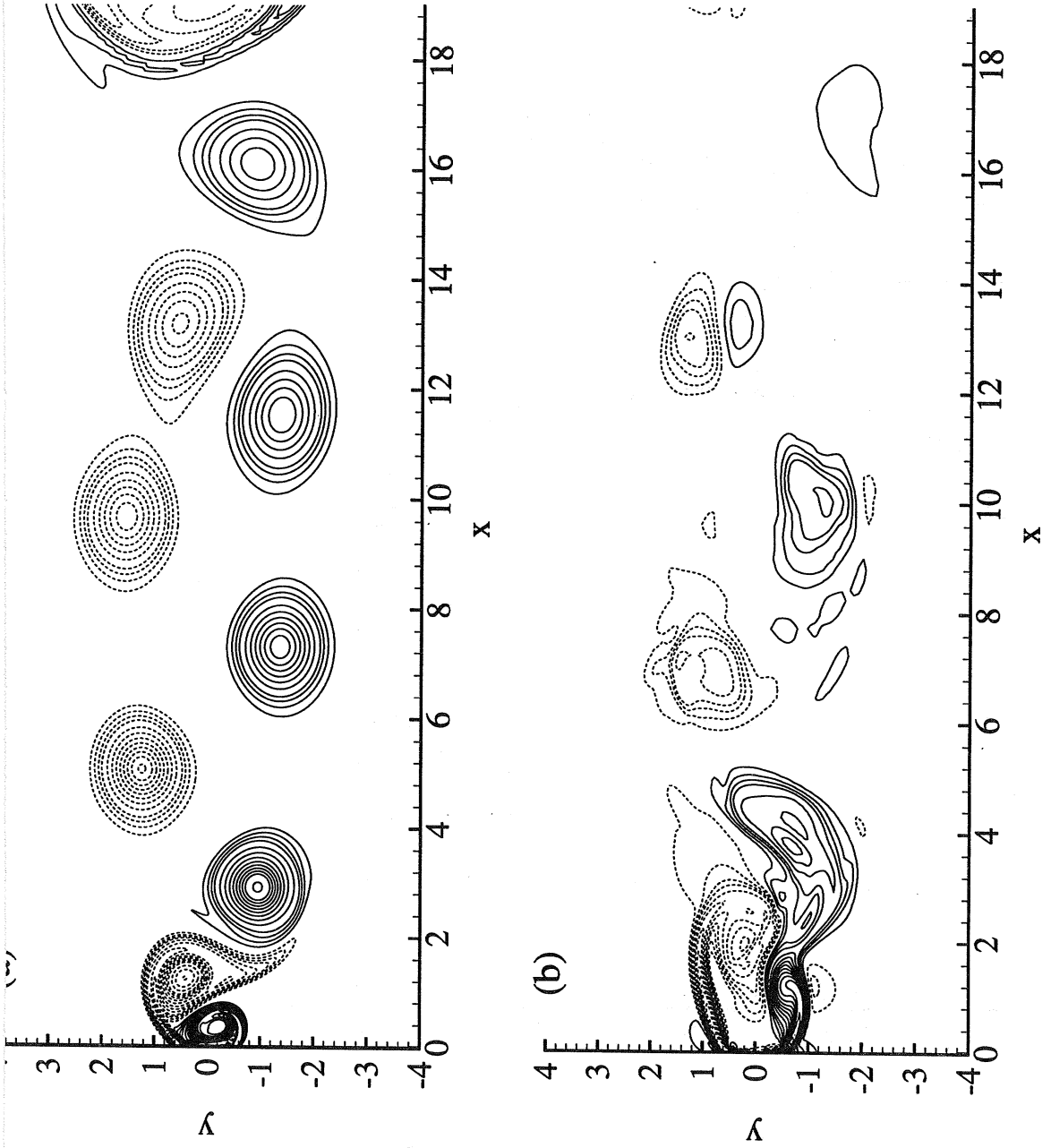

Figure 4. Contour plots of instantaneous spanwise vorticity, ω_z, in the near-wake of the normal flat plate computed from (a) 2-D simulation, (b) 3-D simulation. Span-averaged values are presented in the case of the 3-D computation. Dashed (solid) contours represent clockwise (counter-clockwise) rotation. Three sets of contour levels are used and they are: ($\pm$0.25 to $\pm$1.0 in steps of 0.25), ($\pm$1.0 to $\pm$5.0 in steps of 0.5) and ($\pm$5.0 to $\pm$10.0 in steps of 1.0).

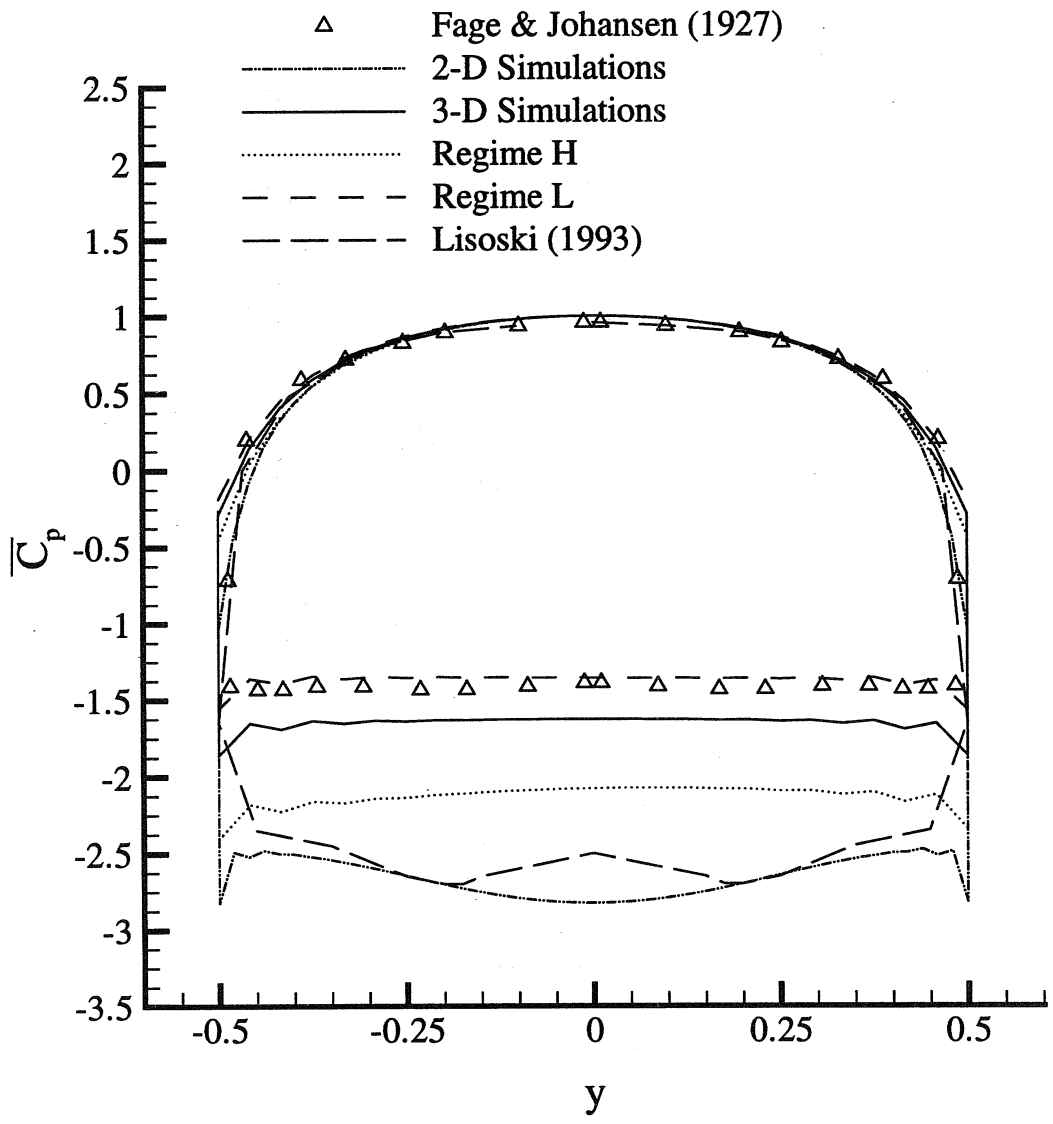

Figure 5. Distribution of the mean pressure coefficient, $\overline{C}_p$, along the plate surface obtained from experiments and computations. The experimental data of Fage and Johansen (1927) is for Re = 1.5×10^5 and the computational results of Lisoski (1993) are obtained from a two-dimensional discrete vortex method. Both current two-dimensional and three-dimensional results are presented. Also shown are the distributions of mean pressure coefficient obtained by time integration only within regimes **H** and **L** of the present three-dimensional simulation.

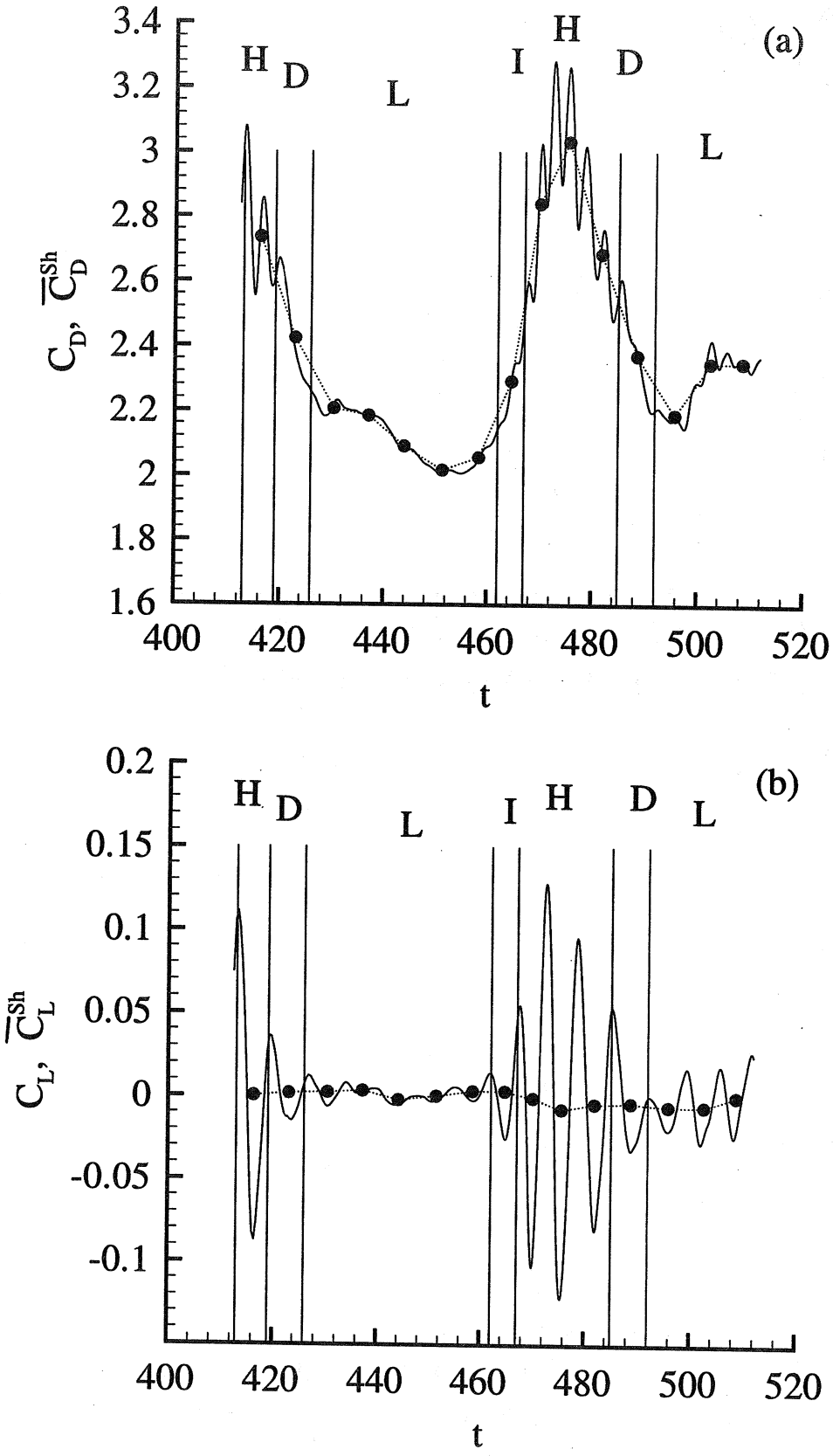

Figure 6. Modulation of (a) the drag and (b) lift coefficients during the time period extending from t=412 to 512 covering two low-frequency cycles. Four regimes are identified and are denoted as regime of high drag (marked **H**), regime of low drag (marked **L**), regime of increasing drag (marked **I**), and regime of decreasing drag (marked **D**). Their temporal extents are demarcated by the vertical lines. The mean drag and lift coefficients averaged within each shedding cycle, $\overline{C}_D^{Sh}$ and $\overline{C}_L^{Sh}$, are plotted as (....•....).

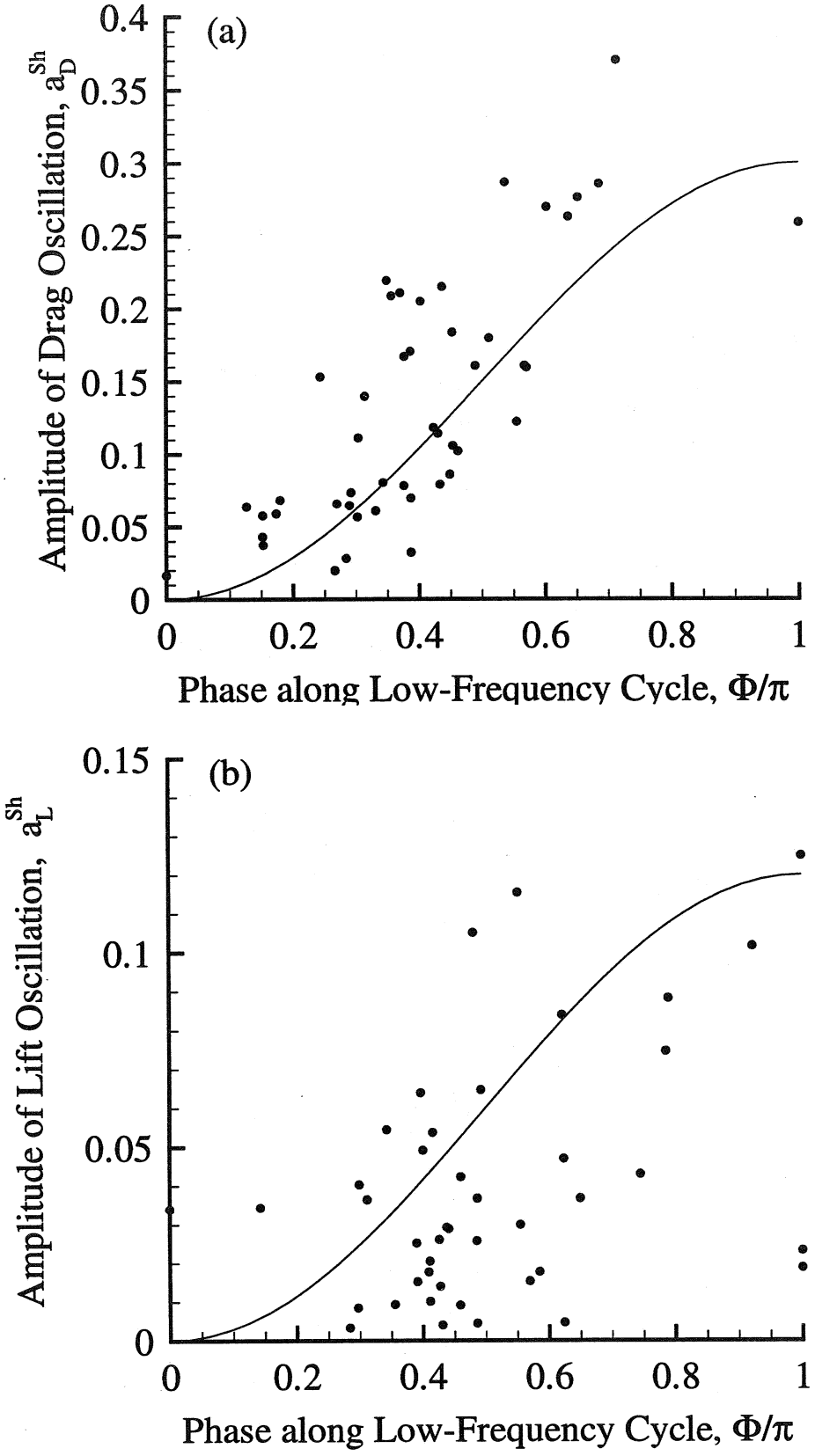

Figure 7. See next page

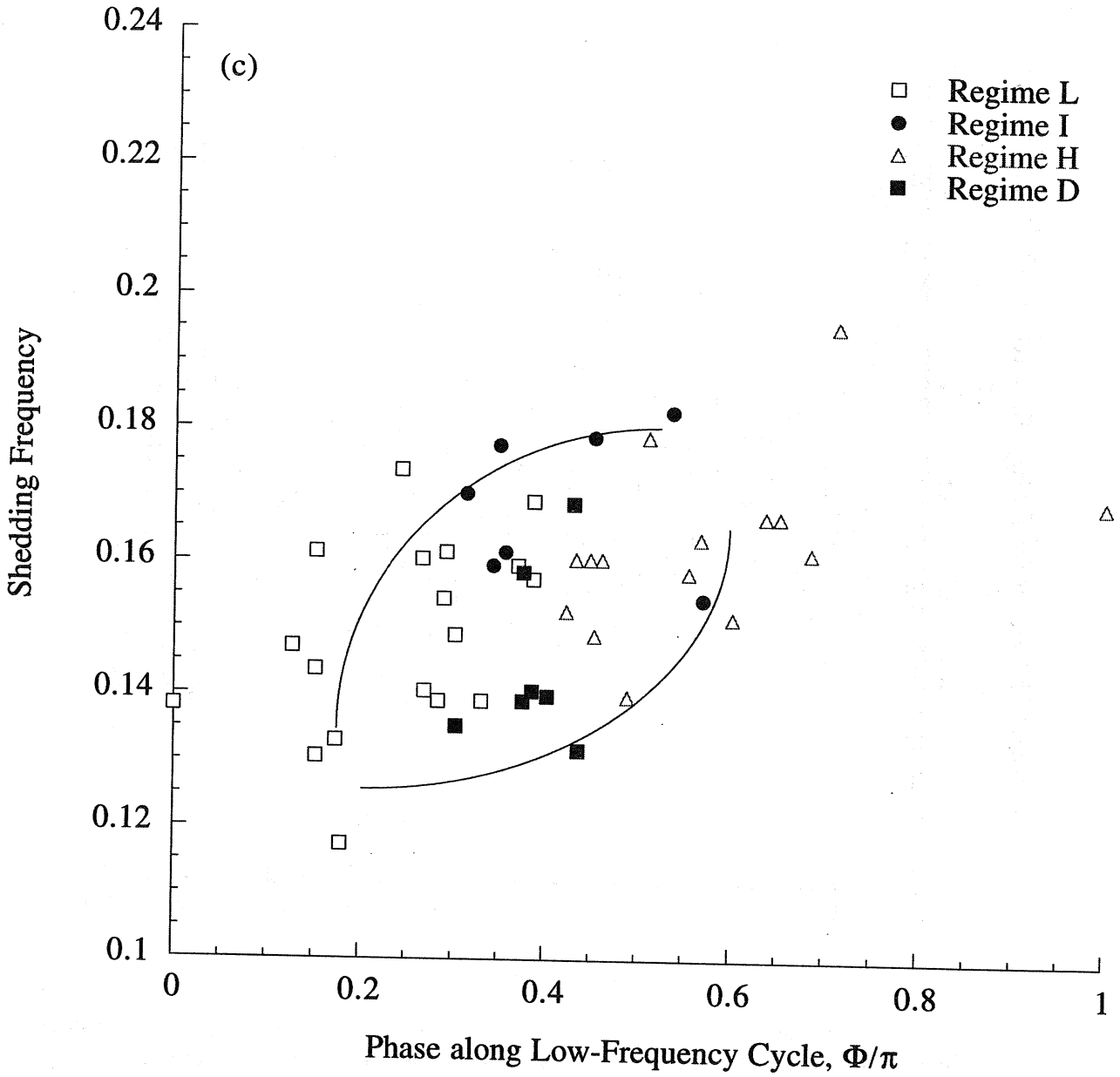

Figure 7. Distribution of (a) the amplitude of the drag oscillation, a_D^{Sh}, (b) the amplitudes of lift oscillation, a_L^{Sh}, and (c) the shedding frequency against the phase along the low-frequency cycle, Φ. $\Phi = 0$ and 2π correspond to time instances of low drag and $\Phi = \pi$ corresponds to time instances of high drag. Analytical models of the amplitudes of drag and lift coefficient variation within each shedding cycle are presented as solid lines: (a) $a_{DI} \sin^2(\Phi/2)$ with $a_{DI} = 0.3$, (b) $a_L \sin^2(\Phi/2)$ with $a_L = 0.12$. In the distribution of shedding frequency, data from the four different regimes are marked by four different symbols. A possible hysteresis in shedding frequency between increasing and decreasing phase of low frequency unsteadiness is sketched out as two solid lines in (c). A general trend of higher shedding frequency with increasing mean drag can be identified in (c).

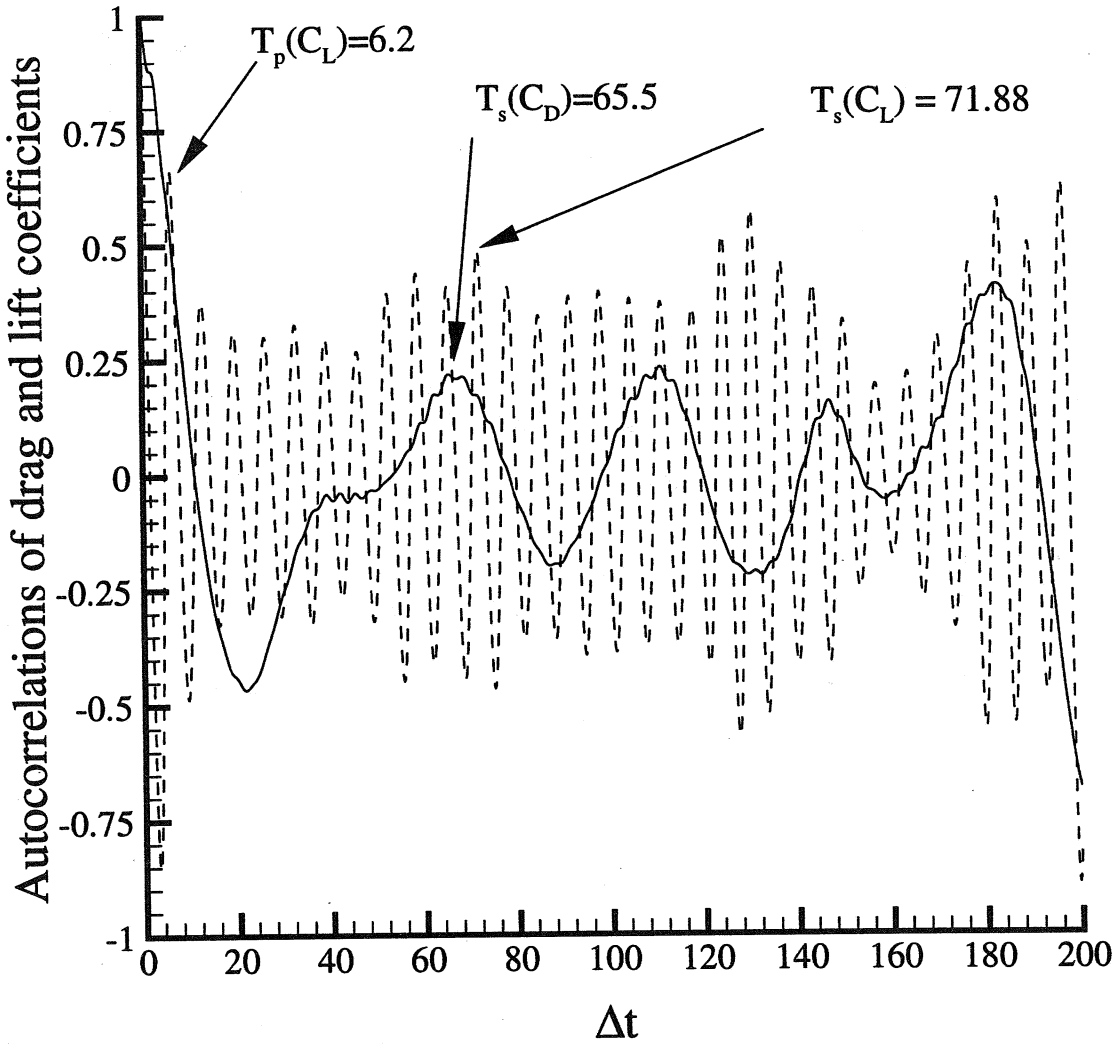

Figure 8. Autocorrelations of drag and lift coefficients are represented by solid and dashed lines respectively. The dominant peak in the autocorrelation of lift corresponds to a shedding period of about 6.2, while the dominant peak in the drag coefficient corresponds to low frequency period of about 65.5. The peak corresponding to the low frequency unsteadiness in the lift coefficient suggests a slightly longer period of about 71.88.

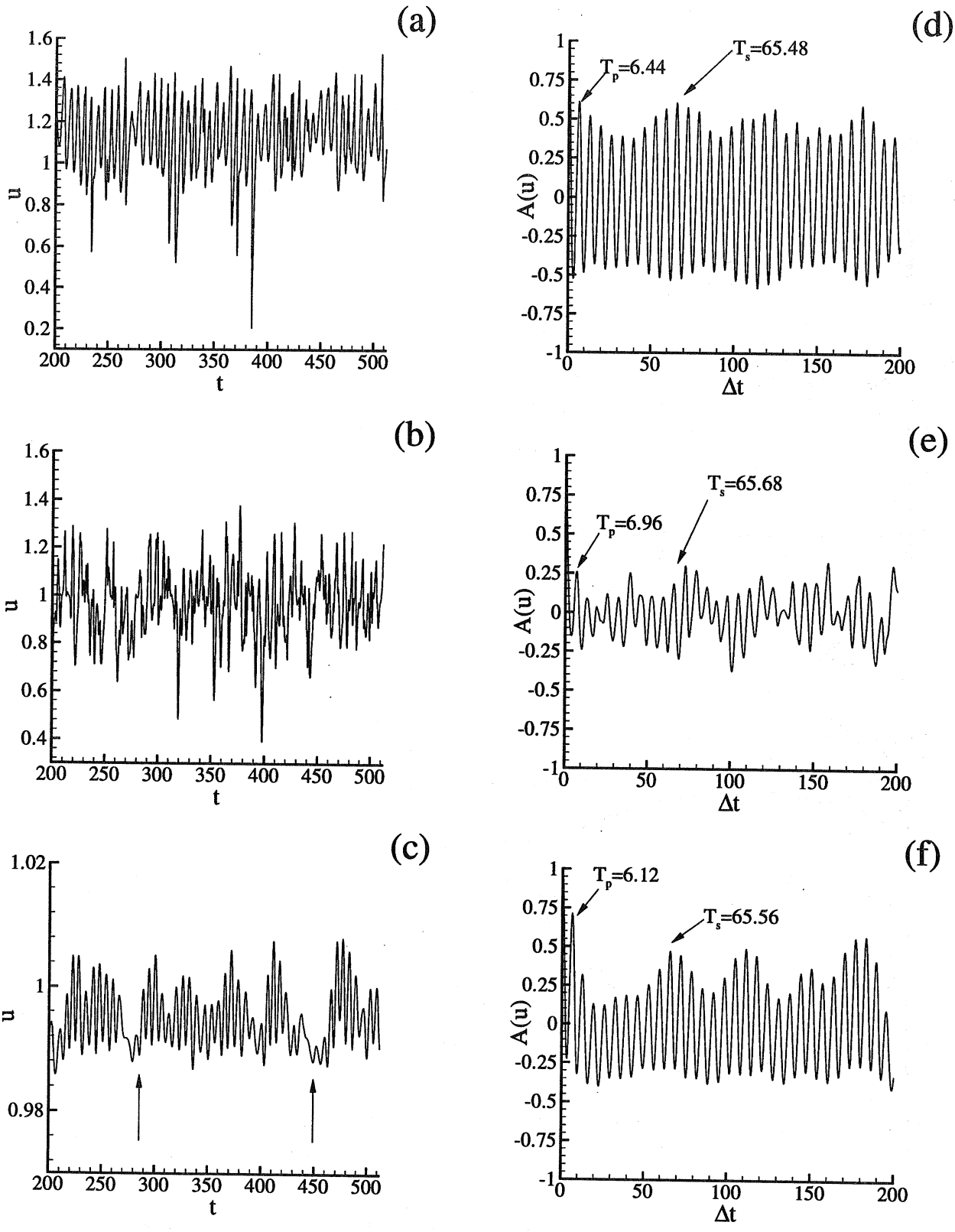

Figure 9. Time signals of the streamwise velocity component at three streamwise locations, (a) $x = 1$, (c) $x = 4$, and (c) $x = 8$. The cross-stream and spanwise locations of all three points are $y = 0.5$ and $z = \pi/2$, respectively. Note that the 'glitches' in (c) (marked with arrows) are qualitatively similar to those due to vortex dislocations, discussed in Williamson (1992). Corresponding autocorrelations of the velocity signals at (d) $x = 1$, (e) $x = 4$, (f) $x = 8$ are also shown. The periods of the primary Karman shedding (T_p) and the secondary low frequency unsteadiness (T_s) are marked. This clearly shows that the low-frequency unsteadiness is not just limited to global variables such as the lift and drag coefficients.

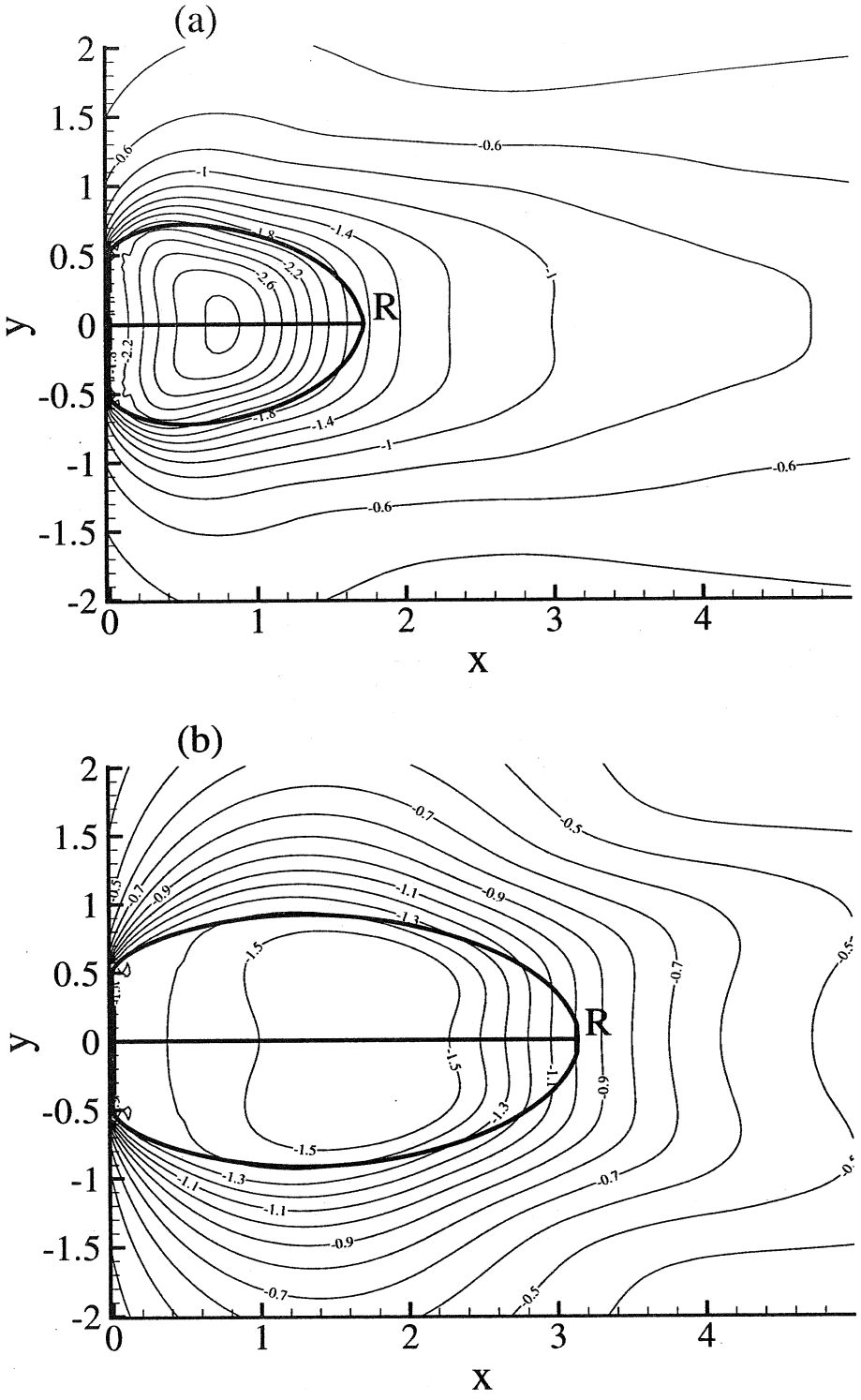

Figure 10. Contour plots of time and span-averaged pressure coefficient in (a) Regime **H** and (b) Regime **L**. The contour levels in (a) extend from -3.0 to -0.4 in steps of 0.1 and in (b) from -1.5 to -0.4 steps of 0.1. The value of base pressure coefficient on the downstream face of the normal plate are -2.1 and -1.5 in regimes **H** and **L**, respectively. The mean wake recirculation region for each regime is identified by the zero-streamline of the time and span-averaged velocity field and drawn as thick contour lines. The reattachment point is marked as R. The length of the mean wake recirculation region is computed from $x = 0$ to R and the half height is defined as the maximum cross-stream (y) distance from the centerline to the periphery of the mean recirculation region.

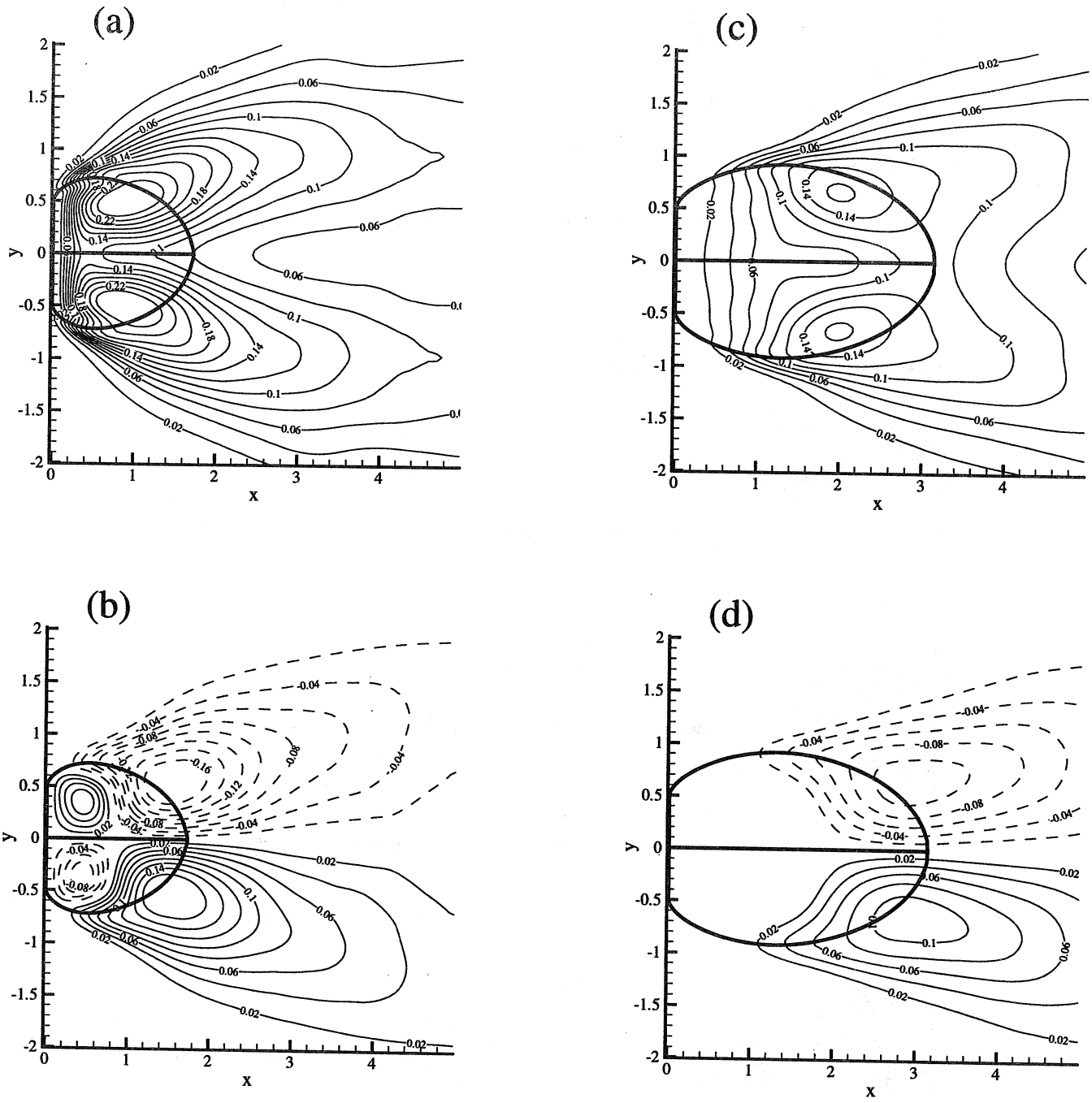

Figure 11. Contour plots of Reynolds streamwise normal and shear stresses in regimes **H** (a-b) and **L** (c-d). Solid and dashed contours denote positive and negative values, respectively. The mean wake recirculation region is also shown as a thick line. (a) and (c) Reynolds streamwise normal stress: contour levels are from 0.02 to 0.24 in steps of 0.02. (b) and (d) Reynolds shear stress: contour levels are from ±0.02 to ±0.16 in steps of 0.02.

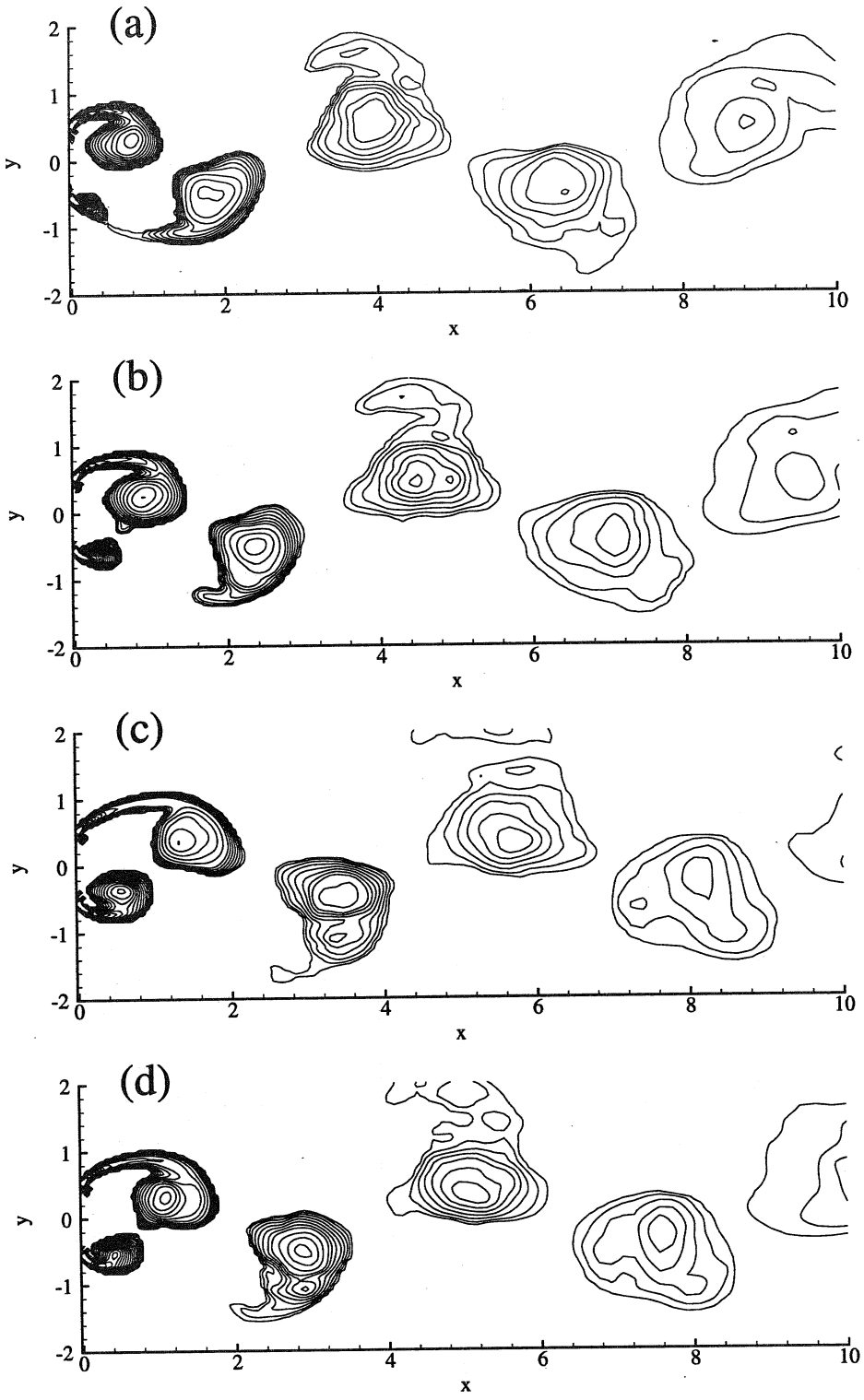

Figure 12. Contours plots of the phase-averaged coherent spanwise swirling strength, $[\overline{\tilde{\lambda}}_{i,p}]_k$. in regime **H**: (a) Phase 1, (b) Phase 2, (c) Phase 3 and (d) Phase 4. Phases 5-8 can be obtained from the above four by reflectional symmetry about the wake centerline. Flow is from left to right with the normal plate at $x = 0$ extending from $-0.5<y<0.5$. Contour levels are: from 0.125 to 1.0 in steps of 0.125 and from 1.0 to 5.0 in steps of 0.25.

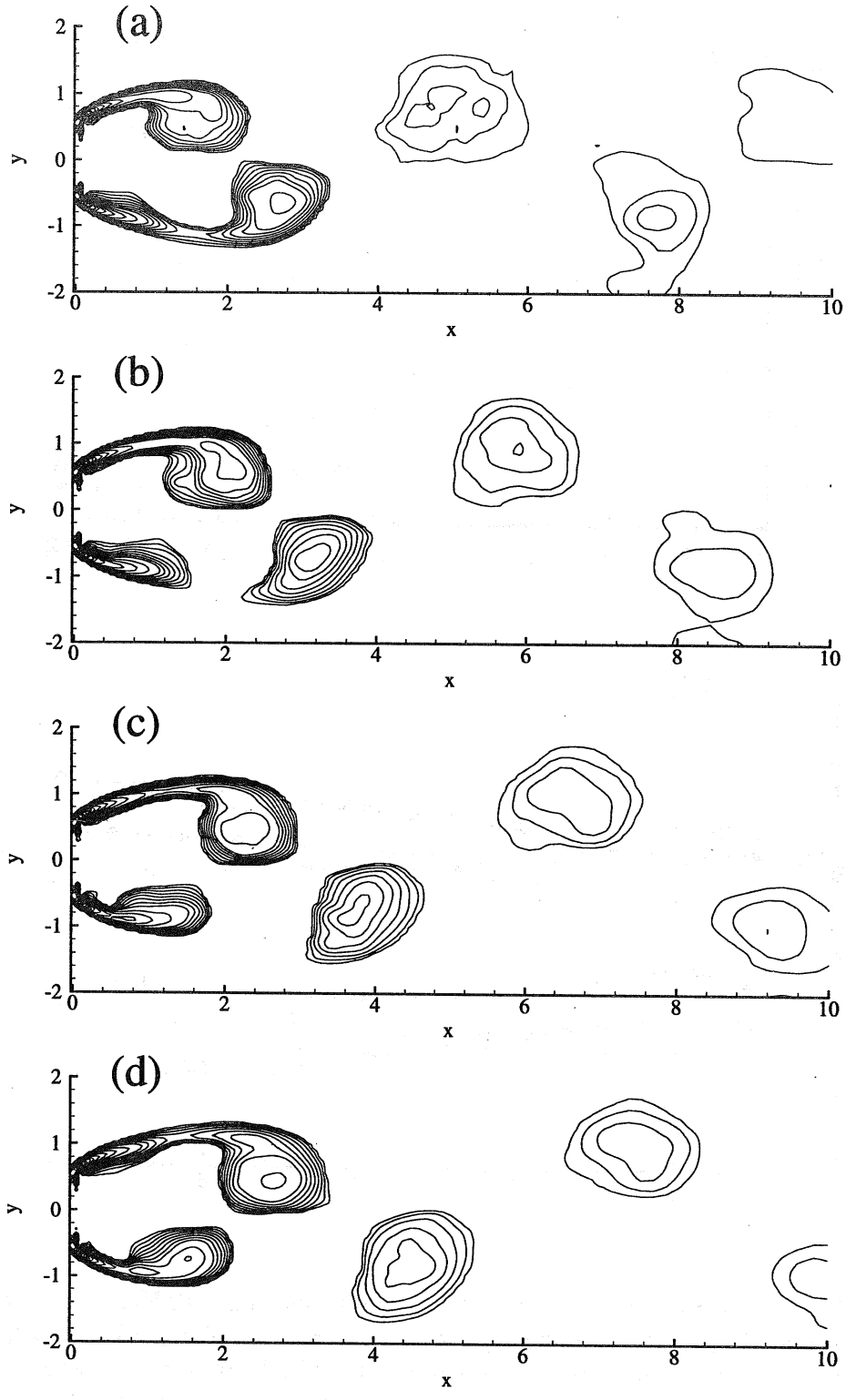

Figure 13. Same as figure 12 for regime **L**.

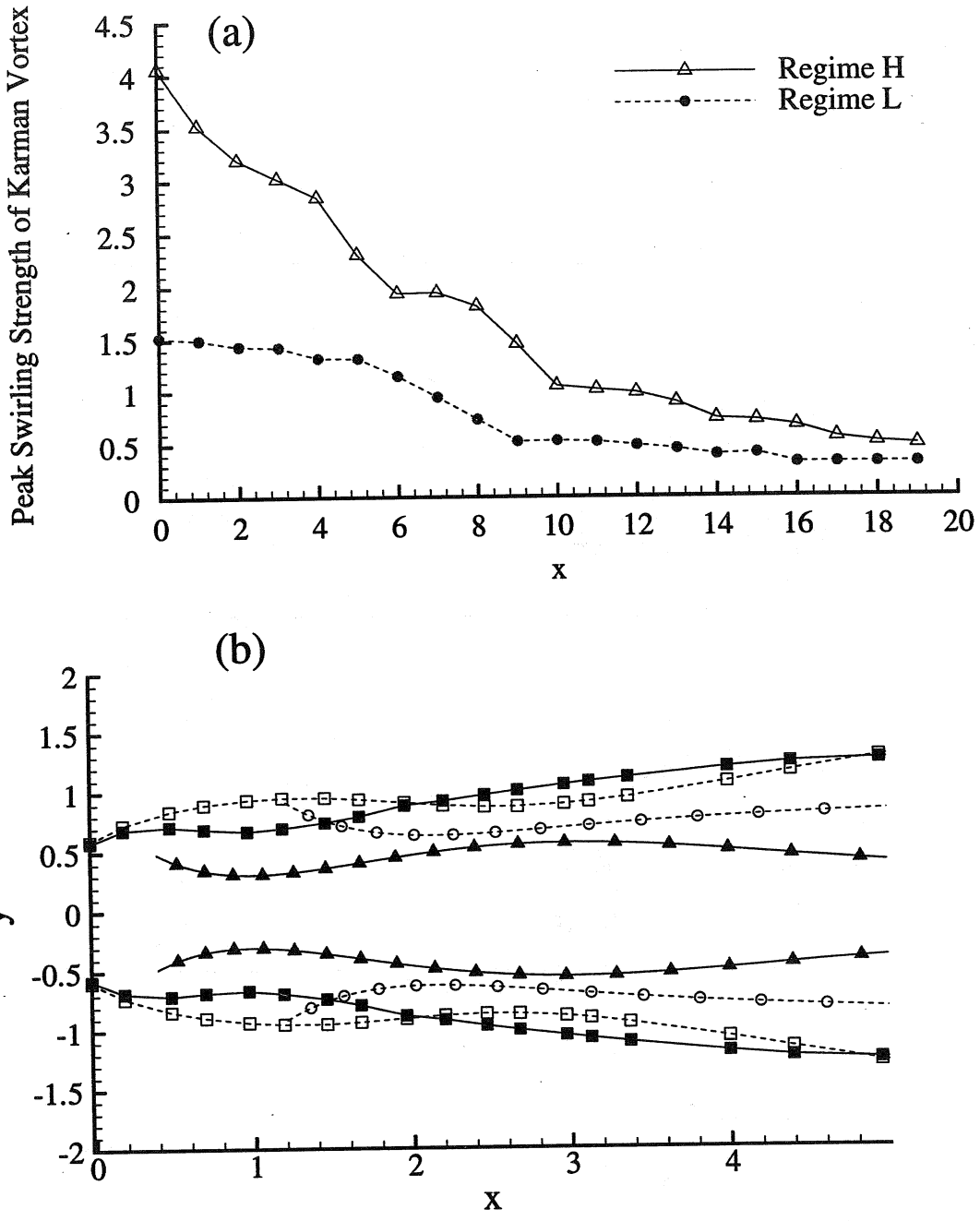

Figure 14. (a) Streamwise evolution of the peak strength of the coherent Karman vortex core in regime **H** (____Δ____) and regime **L** (- - - • - - -). The peak strength of the vortex core is defined as the maximum magnitude of the spanwise swirling strength within the vortex (see Figures 12 and 13). (b) Typical Karman vortex trajectories (circles) and the location of the shear layer center, y_c , (squares) in regimes **H** and **L**. Open and closed symbols denote regimes **L** and **H**.

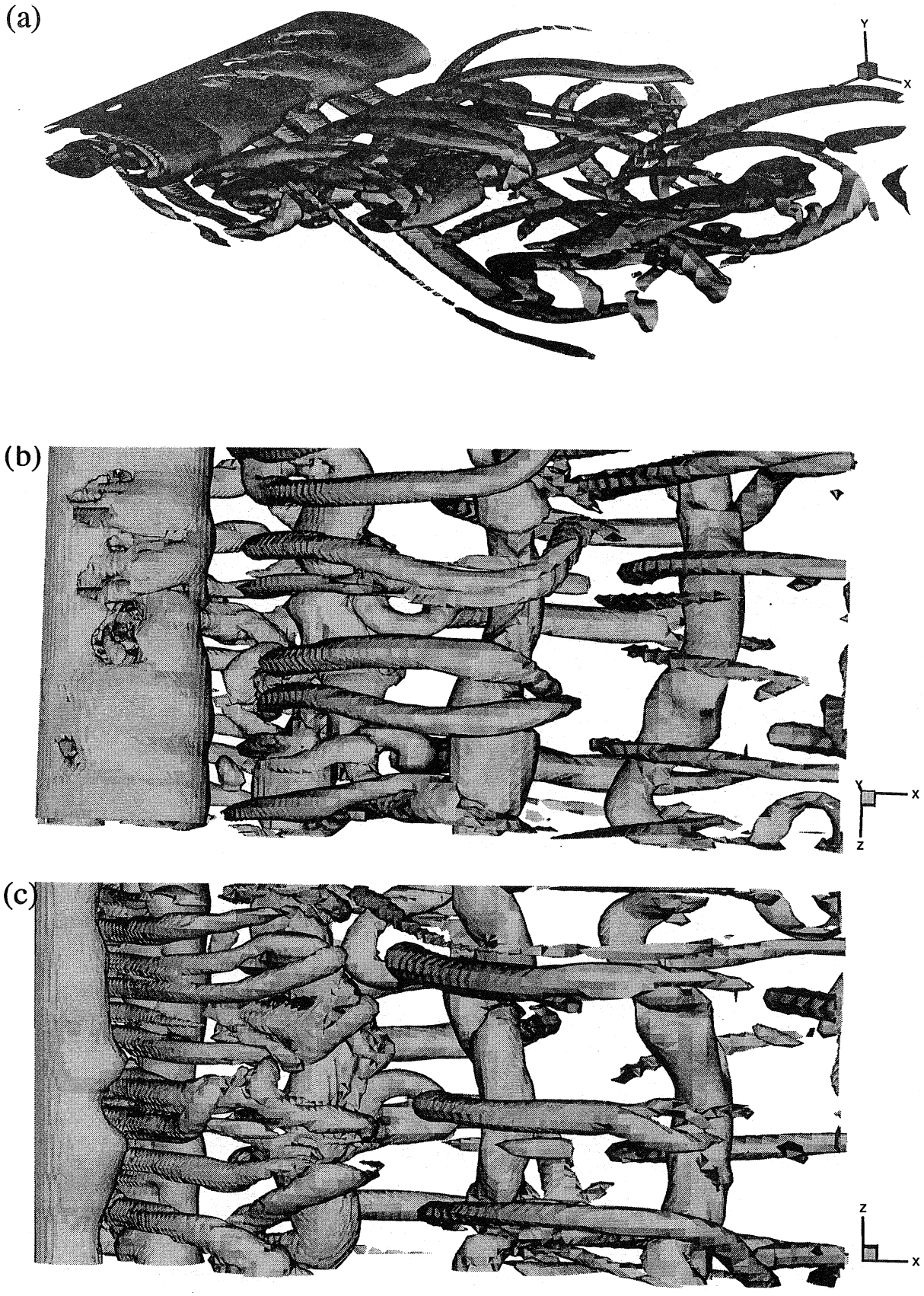

Figure 15. Iso-surface of the three-dimensional instantaneous swirling strength, $\lambda_{i,3D}=1.0$, at $t=416$, in regime **H**. (a) Perspective, (b) top, and (c) bottom views of the iso-surface. Flow is from left to right. Clockwise rotating (CR) and Counter-clockwise rotating (CCR) Karman vortices are pointed with arrows.

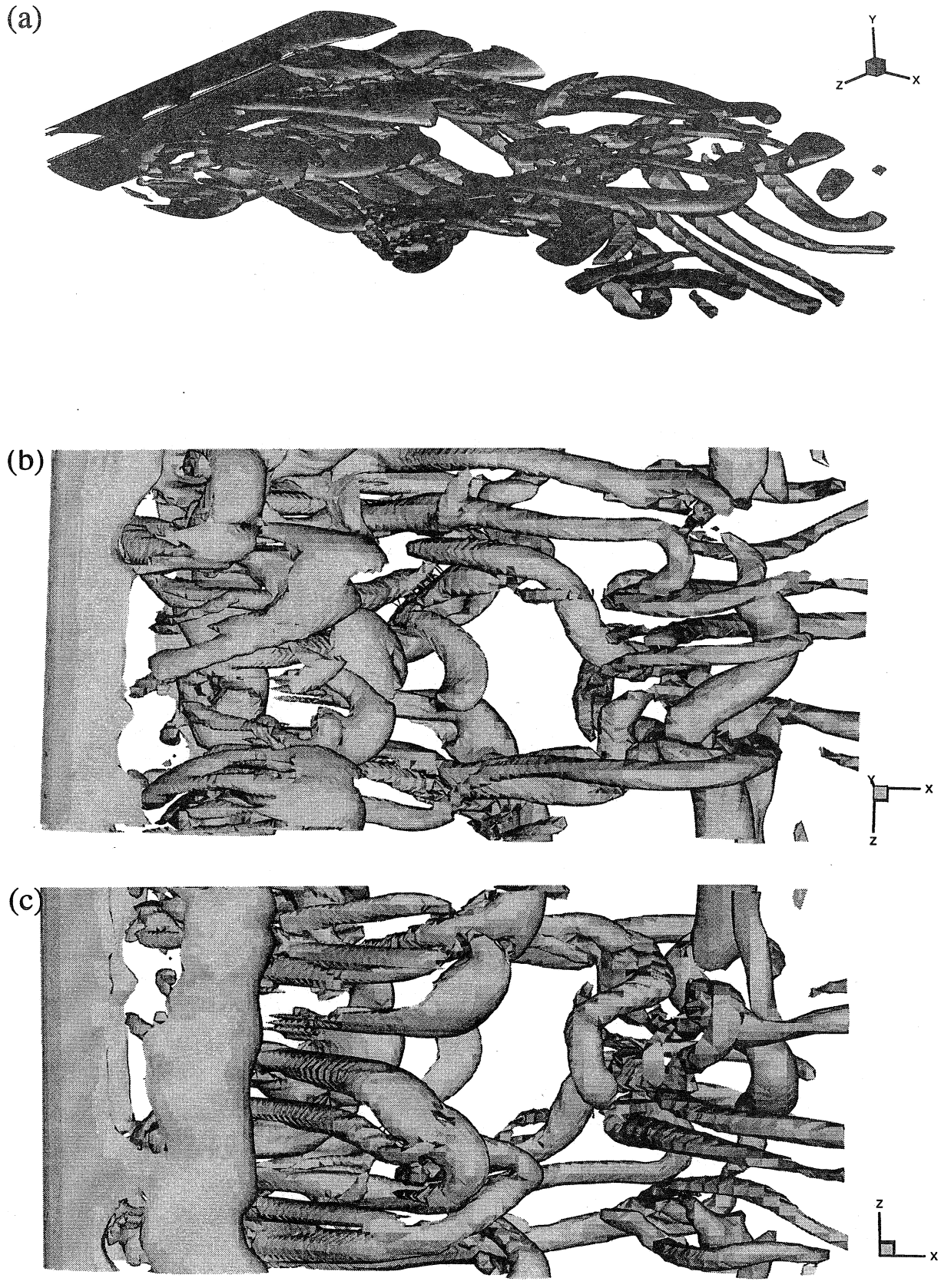

Figure 16. Same as figure 15 at t=456, in regime **L**.

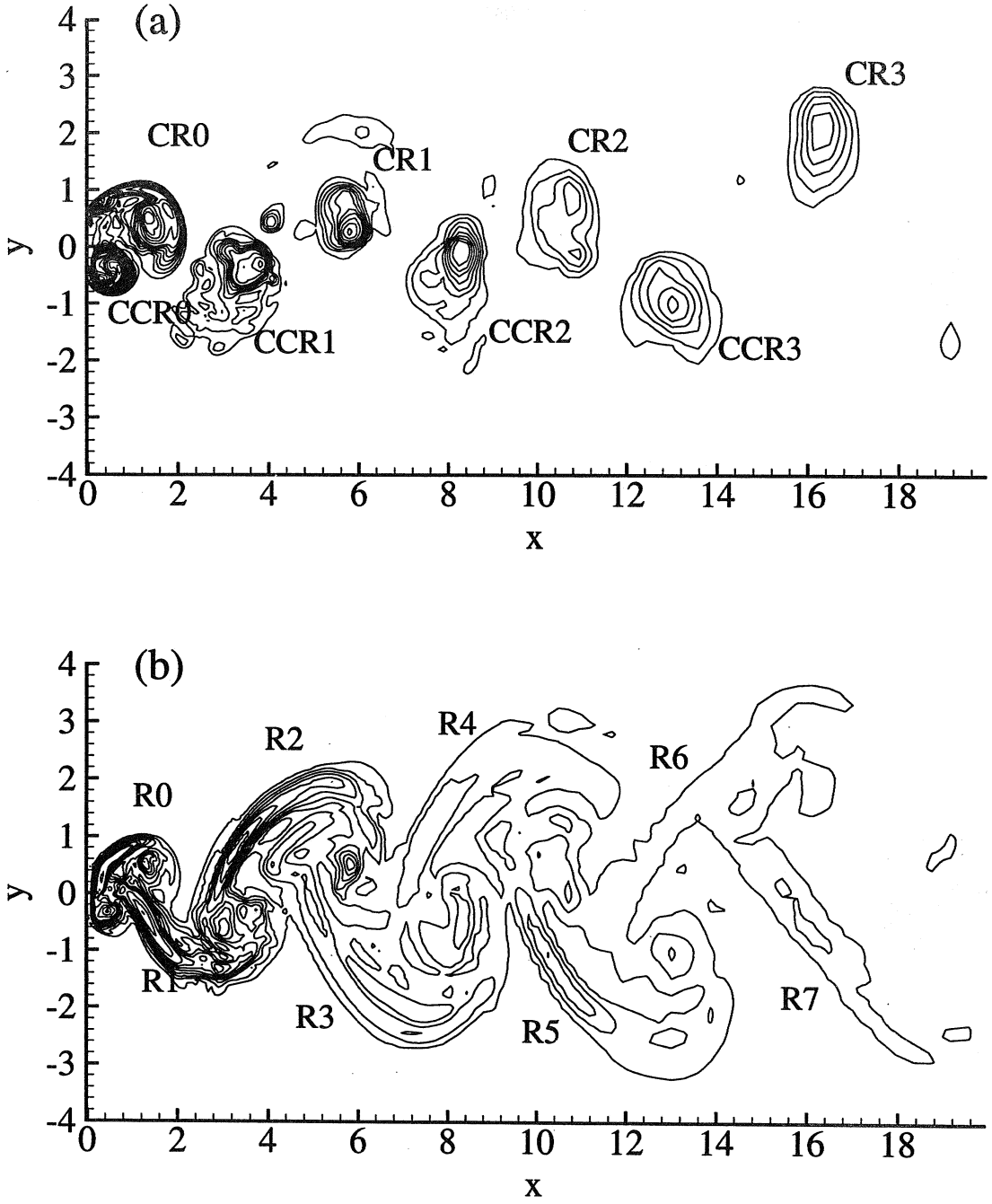

Figure 17. Contour plots of span-averaged instantaneous spanwise swirling strength, $\langle\lambda_{i,p}\rangle_z$, in (a) Regime **H** at t=416 and (c) Regime **L** at t=456. Clockwise rotating (CR) and Counter-clockwise rotating (CCR) Karman vortices are numbered and marked. Contour plots of span-averaged instantaneous streamwise swirling strength, $\langle\lambda_{i,s}\rangle_z$, in (b) Regime **H** at t=416 and (d) Regime **L** at t=456. Streamwise ribs connecting the Karman vortices are marked as R0, R1, etc. Contour levels are 0.125 to 1.0 in steps of 0.125 and from 1.0 to 5.0 in steps of 0.25.

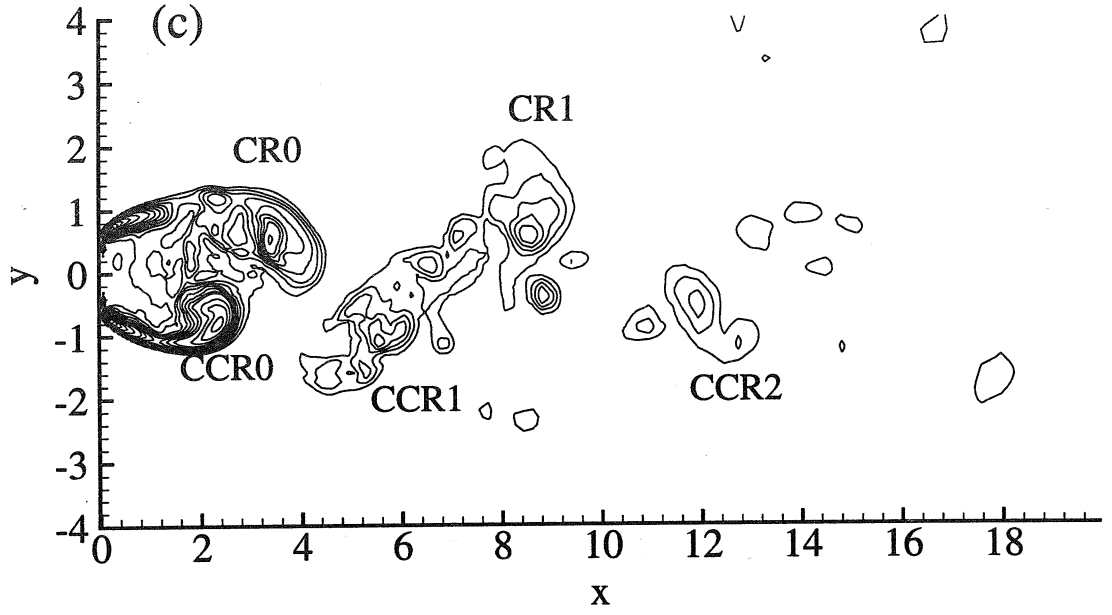
(c)
CR0
CR1
CCR0
CCR1
CCR2
y
x

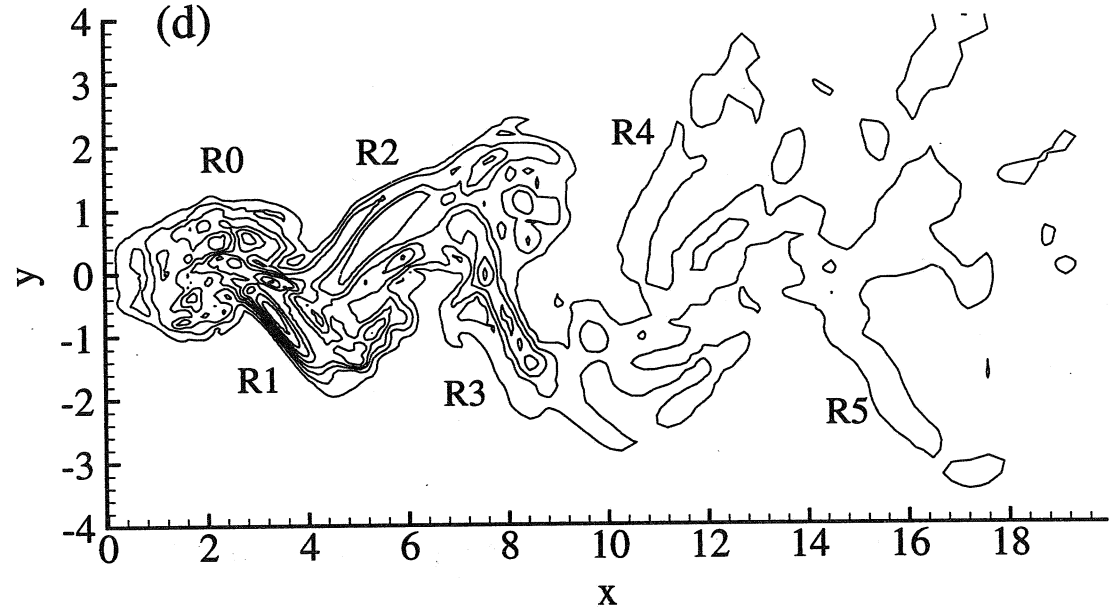
(d)
R0
R1
R2
R3
R4
R5
y
x

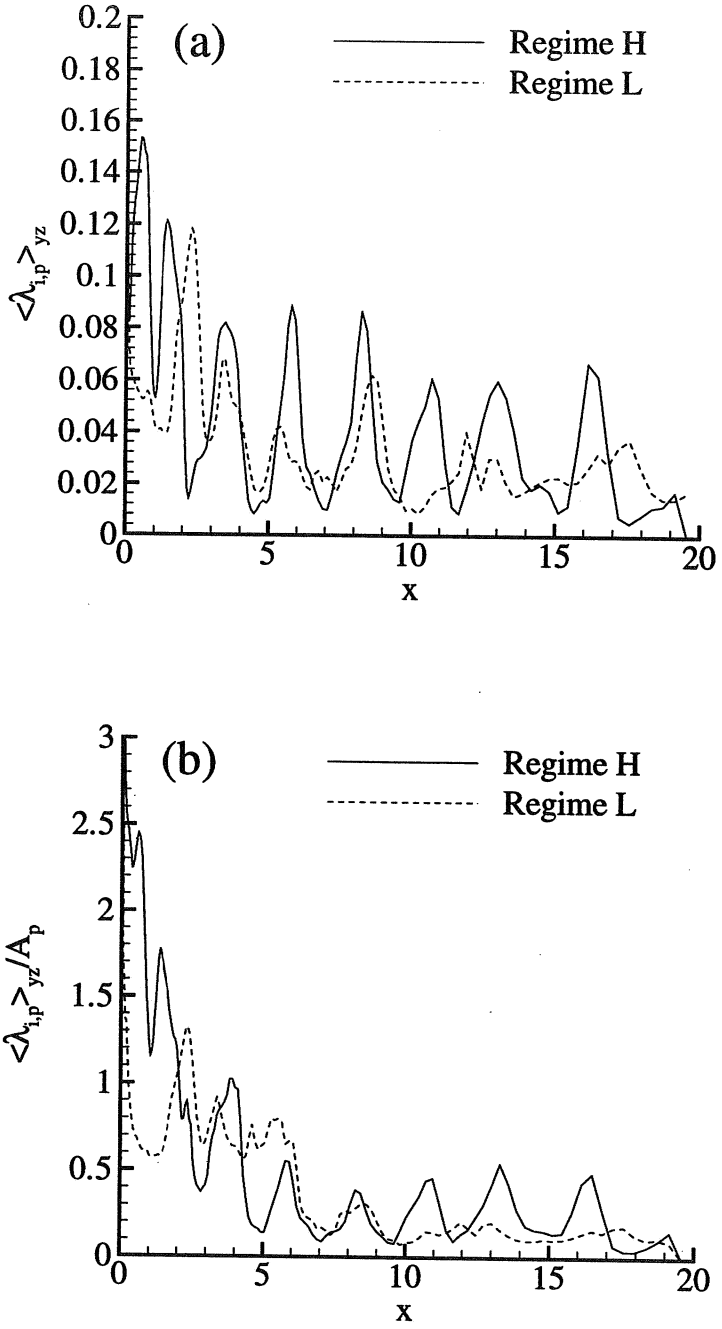

Figure 18. (a) Streamwise evolution of the instantaneous y-z plane-averaged spanwise swirling strength, $<\lambda_{i,p}>_{yz}$. This plot when scaled by the cross-sectional area of the y-z plane, $2L_yL_z$, gives the total swirling strength of the Karman vortices at any streamwise location. (b) Same as the above but the plane-averaged spanwise swirling strength inversely scaled by the fractional area, A_p, occupied by the primary Karman vortices in any y-z plane, $<\lambda_{i,p}>_{yz}/A_p$. This appropriately scaled quantity provides the true intensity or the average concentration of swirling strength within the spanwise vortices. The solid line denotes regime **H** (t=416), and the broken line denotes regime **L** (t=456).

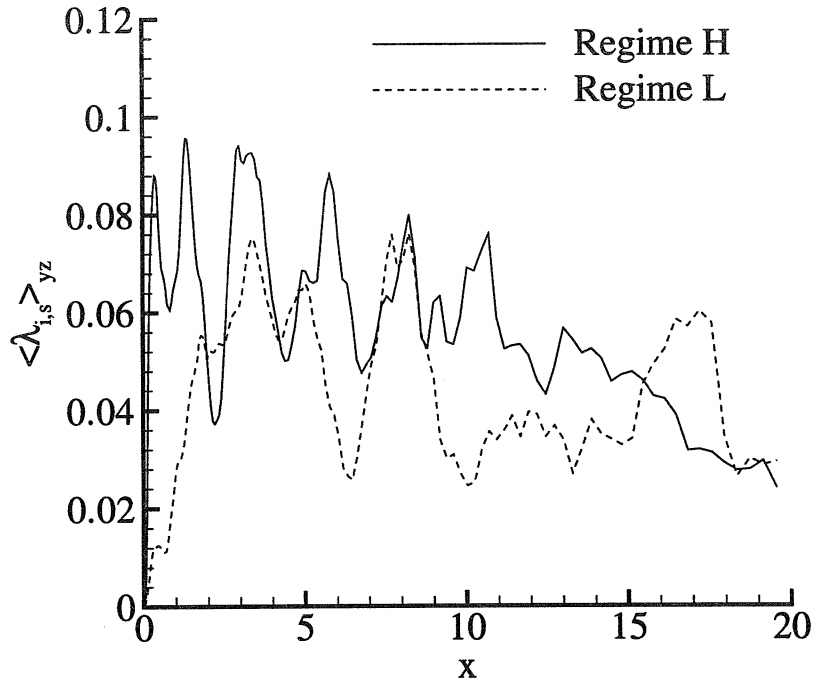

Figure 19. Streamwise evolution of the instantaneous y-z plane-averaged cross-span (secondary) swirling strength, $\langle\lambda_{i,s}\rangle_{yz}$. Solid line denotes regime **H**(t=416), and broken line denotes regime **L** (t=456). This plot when scaled by the cross-sectional area of the y-z plane, $2L_yL_z$, gives the total swirling strength of the streamwise vortices at any streamwise location.

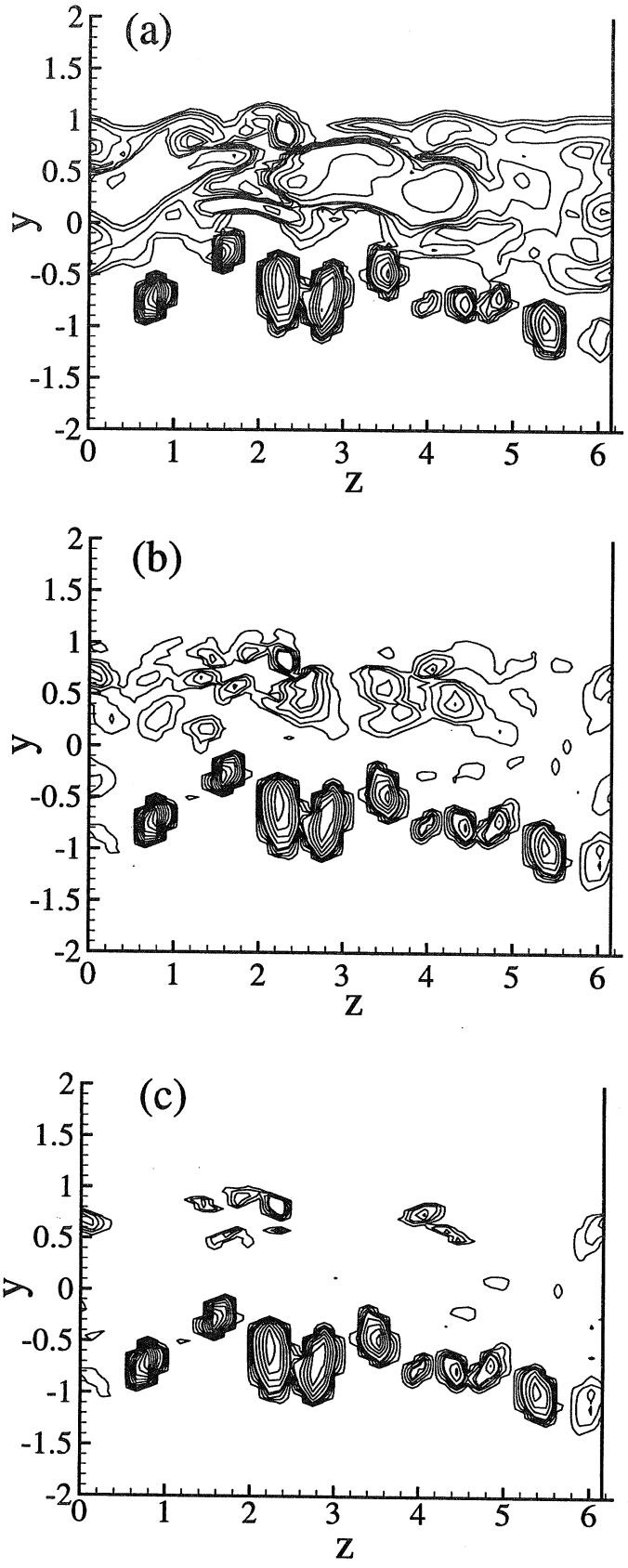

Figure 20. Contour plots of (a) three-dimensional swirling strength, $\lambda_{i,3D}$, (b) unfiltered cross-span swirling strength, $\lambda_{i,s}$, and (c) filtered streamwise swirling strength, $\lambda_{i,s}I_s$, in the y-z plane at x = 1.5 for time instance, t=416 (Regime H). About ten streamwise ribs can be seen in all three plots, but the influence of the distorted spanwise Karman vortex has clearly been filtered out in (c). Contour levels are from 0.25 to 1.75 in steps of 0.5 and from 2.0 to 9.0 in steps of 1.0.

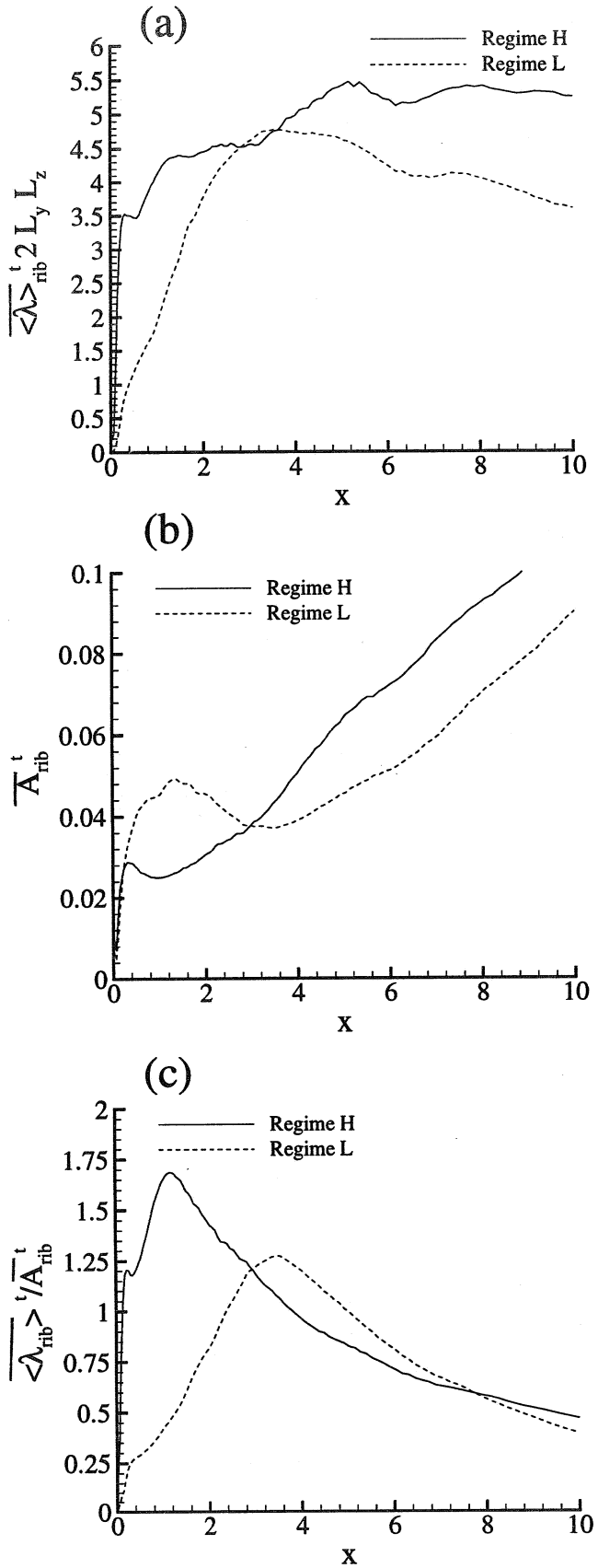

Figure 21. Streamwise distributions of (a) total swirling strength of the streamwise ribs, $(2L_y L_z)\overline{<\lambda>_{rib}}^{t}$ (b) fractional area, $\overline{A_{rib}}^{t}$, occupied by the ribs in the *y*-*z* plane and (c) the intensity or the average concentration of swirling strength within the streamwise ribs measured as the ratio of swirling strength to the fractional area of the ribs, $\overline{<\lambda>_{rib}}^{t} / \overline{A_{rib}}^{t}$. The solid lines denote regime **H**, and broken line denotes regime **L**. Quantities have been averaged both in the *y*-*z* plane and in time.

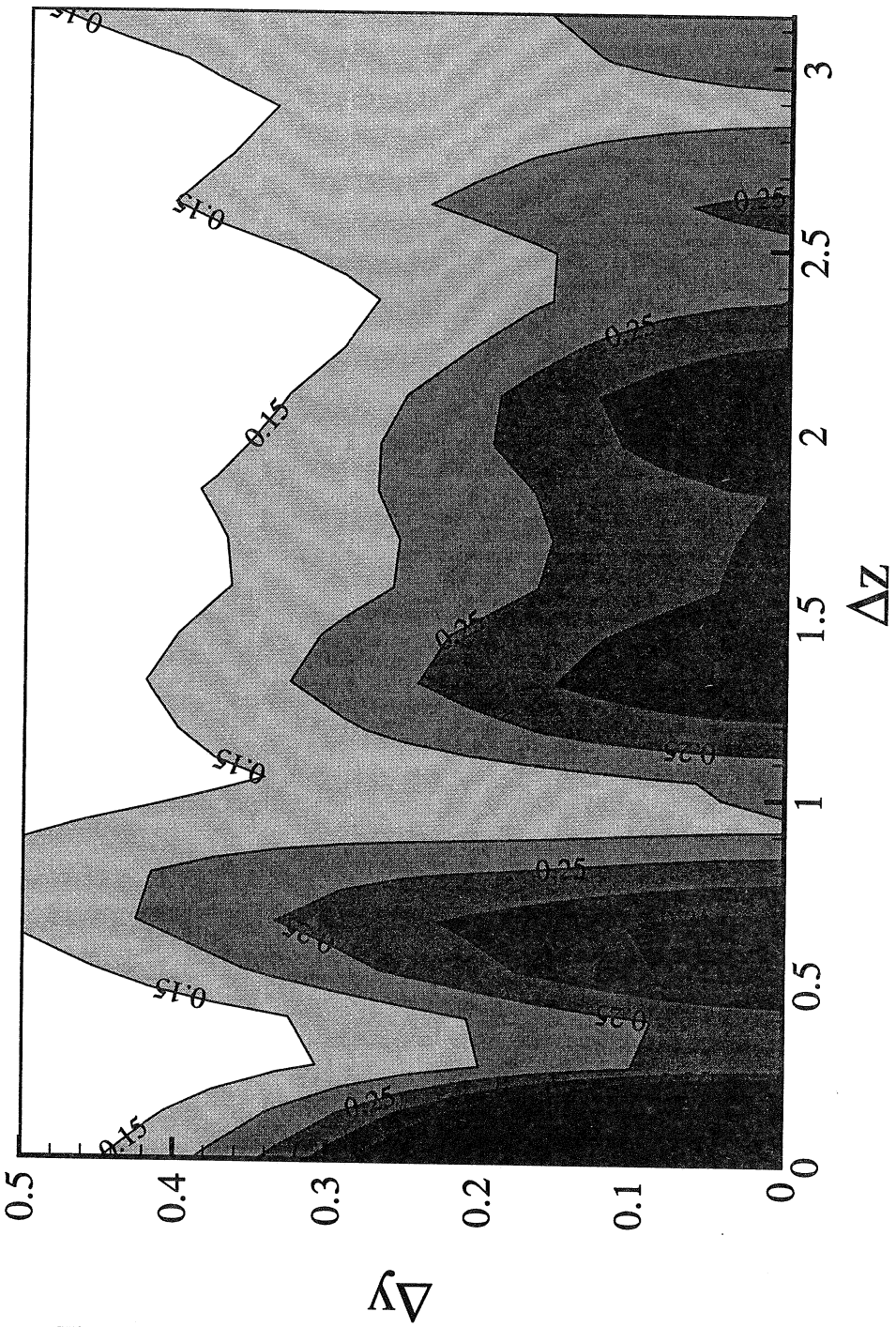

Figure 22. The two-point correlation, $R(\Delta y, \Delta z, t)$, of the filtered streamwise swirling strength, $\lambda_{i,s} I_s$, plotted as a function of separation along the cross-stream (y) and spanwise (z) directions, for the time instance t = 416, in regime **H**. Light shades represent low values of the correlation and dark shades correspond to high values. Contours levels are from 0.15 to 0.45 in steps of 0.05. Apart from the dominant peak at $\Delta y = 0$ and $\Delta z = 0$, a second peak at $\Delta y \approx 0$ and $\Delta z \approx 0.6$ can also be observed corresponding to a non-dimensional spanwise wavelength of about 1.2.

List of Recent TAM Reports

No.	Authors	Title	Date
773	Stewart, D. S., T. D. Aslam, J. Yao, and J. B. Bdzil	Level-set techniques applied to unsteady detonation propagation—In "Modeling in Combustion Science," *Lecture Notes in Physics* , eds. J. Buckmaster and J. Takeno **126**, 390–409 (1996)	Oct. 1994
774	Mittal, R., and S. Balachandar	Effect of three-dimensionality on the lift and drag of circular and elliptic cylinders—*Physics of Fluids* **7**, 1841–1865 (1995)	Oct. 1994
775	Stewart, D. S., T. D. Aslam, and J. Yao	On the evolution of cellular detonation	Nov. 1994 *Revised* Jan. 1996
776	Aref, H.	On the equilibrium and stability of a row of point vortices—*Journal of Fluid Mechanics* **290**, 167–181 (1995)	Nov. 1994
777	Cherukuri, H. P., T. G. Shawki, and M. El-Raheb	An accurate finite-difference scheme for elastic wave propagation in a circular disk—*Journal of the Acoustical Society of America*, in press (1996)	Nov. 1994
778	Li, L., and N. R. Sottos	Improving hydrostatic performance of 1–3 piezocomposites—*Journal of Applied Physics* **77**, 4595–4603 (1995)	Dec. 1994
779	Phillips, J. W., D. L. de Camara, M. D. Lockwood, and W. C. C. Grebner	Strength of silicone breast implants—*Plastic and Reconstructive Surgery* **97**, 1215–1225 (1996)	Jan. 1995
780	Xin, Y.-B., K. J. Hsia, and D. A. Lange	Quantitative characterization of the fracture surface of silicon single crystals by confocal microscopy—*Journal of the American Ceramics Society* **78**, 3201–3208 (1995)	Jan. 1995
781	Yao, J., and D. S. Stewart	On the dynamics of multi-dimensional detonation—*Journal of Fluid Mechanics* **309**, 225–275 (1996)	Jan. 1995
782	Riahi, D. N., and T. L. Sayre	Effect of rotation on the structure of a convecting mushy layer—*Acta Mechanica* **118**, 109–120 (1996)	Feb. 1995
783	Batchelor, G. K., and TAM faculty and students	A conversation with Professor George K. Batchelor	Feb. 1995
784	Sayre, T. L., and D. N. Riahi	Effect of rotation on flow instabilities during solidification of a binary alloy—*International Journal of Engineering Science* **34**, 1631–1645 (1996)	Feb. 1995
785	Xin, Y.-B., and K. J. Hsia	A technique to generate straight surface cracks for studying the dislocation nucleation condition in brittle materials—*Acta Metallurgica et Materialia* **44**, 845–853 (1996)	Mar. 1995
786	Riahi, D. N.	Finite bandwidth, long wavelength convection with boundary imperfections: Near-resonant wavelength excitation—*International Journal of Mathematics and Mathematical Sciences*, in press (1996)	Mar. 1995
787	Turner, J. A., and R. L. Weaver	Average response of an infinite plate on a random foundation—*Journal of the Acoustical Society of America* **99**, 2167–2175 (1996)	Mar. 1995
788	Weaver, R. L., and D. Sornette	The range of spectral correlations in pseudointegrable systems: GOE statistics in a rectangular membrane with a point scatterer—*Physical Review E* **52**, 341 (1995)	Apr. 1995
789	Students in TAM 293–294	Thirty-second student symposium on engineering mechanics, J. W. Phillips, coordinator: Selected senior projects by K. F. Anderson, M. B. Bishop, B. C. Case, S. R. McFarlin, J. M. Nowakowski, D. W. Peterson, C. V. Robertson, and C. E. Tsoukatos	Apr. 1995
790	Figa, J., and C. J. Lawrence	Linear stability analysis of a gravity-driven Newtonian coating flow on a planar incline	May 1995
791	Figa, J., and C. J. Lawrence	Linear stability analysis of a gravity-driven viscosity-stratified Newtonian coating flow on a planar incline	May 1995
792	Cherukuri, H. P., and T. G. Shawki	On shear band nucleation and the finite propagation speed of thermal disturbances—*International Journal of Solids and Structures*, in press (1996)	May 1995

List of Recent TAM Reports (cont'd)

No.	*Authors*	*Title*	*Date*
793	Harris, J. G.	Modeling scanned acoustic imaging of defects at solid interfaces—Chapter in *IMA Workshop on Inverse Problems in Wave Propagation*, eds. G. Chevant, G. Papanicolaou, P. Sacks and W. E. Symes, 237–258, Springer-Verlag, New York (1996)	May 1995
794	Sottos, N. R., J. M. Ockers, and M. J. Swindeman	Thermoelastic properties of plain weave composites for multilayer circuit board applications	May 1995
795	Aref, H., and M. A. Stremler	On the motion of three point vortices in a periodic strip—*Journal of Fluid Mechanics* **314**, 1–25 (1996)	June 1995
796	Barenblatt, G. I., and N. Goldenfeld	Does fully-developed turbulence exist? Reynolds number independence versus asymptotic covariance—*Physics of Fluids* **7**, 3078–3082 (1995)	June 1995
797	Aslam, T. D., J. B. Bdzil, and D. S. Stewart	Level set methods applied to modeling detonation shock dynamics—*Journal of Computational Physics*, **126**, 390–409 (1996)	June 1995
798	Nimmagadda, P. B. R., and P. Sofronis	The effect of interface slip and diffusion on the creep strength of fiber and particulate composite materials—Proceedings of the ASME Applied Mechanics Division **213**, 125–143 (1995)	July 1995
799	Hsia, K. J., T.-L. Zhang, and D. F. Socie	Effect of crack surface morphology on the fracture behavior under mixed mode loading—*ASTM Special Technical Publication* 1296, in press (1996)	July 1995
800	Adrian, R. J.	Stochastic estimation of the structure of turbulent fields—*Eddy Structure Identification*, ed. J. P. Bonnet, Springer: Berlin 145–196 (1996)	Aug. 1995
801	Riahi, D. N.	Perturbation analysis and modeling for stratified turbulence	Aug. 1995
802	Thoroddsen, S. T.	Conditional sampling of dissipation in high Reynolds number turbulence—*Physics of Fluids* **8**, 1333–1335	Aug. 1995
803	Riahi, D. N.	On the structure of an unsteady convecting mushy layer—*Acta Mechanica*, in press (1996)	Aug. 1995
804	Meleshko, V. V.	Equilibrium of an elastic rectangle: The Mathieu–Inglis–Pickett solution revisited—*Journal of Elasticity* **40**, 207–238 (1995)	Aug. 1995
805	Jonnalagadda, K., G. E. Kline, and N. R. Sottos	Local displacements and load transfer in shape memory alloy composites	Aug. 1995
806	Nimmagadda, P. B. R., and P. Sofronis	On the calculation of the matrix–reinforcement interface diffusion coefficient in composite materials at high temperatures—*Acta Metallurgica et Materialia*, **44**, 2711–2716 (1996)	Aug. 1995
807	Carlson, D. E., and D. A. Tortorelli	On hyperelasticity with internal constraints—*Journal of Elasticity* **42**, 91–98 (1966)	Aug. 1995
808	Sayre, T. L., and D. N. Riahi	Oscillatory instabilities of the liquid and mushy layers during solidification of alloys under rotational constraint—*Acta Mechanica* **121** , 143–152 (1997)	Sept. 1995
809	Xin, Y.-B., and K. J. Hsia	Simulation of the brittle–ductile transition in silicon single crystals using dislocation mechanics	Oct. 1995
810	Ulysse, P., and R. E. Johnson	A plane-strain upper-bound analysis of unsymmetrical single-hole and multi-hole extrusion processes	Oct. 1995
811	Fried, E.	Continua described by a microstructural field—*Zeitschrift für angewandte Mathematik und Physik*, **47**, 168–175 (1996)	Nov. 1995
812	Mittal, R., and S. Balachandar	Autogeneration of three-dimensional vortical structures in the near wake of a circular cylinder	Nov. 1995
813	Segev, R., E. Fried, and G. de Botton	Force theory for multiphase bodies—*Journal of Geometry and Physics*, in press (1996)	Dec. 1995
814	Weaver, R. L.	The effect of an undamped finite-degree-of-freedom "fuzzy" substructure: Numerical solutions and theoretical discussion—*Journal of the Acoustical Society of America* **100**, 3159–3164 (1996)	Jan. 1996

List of Recent TAM Reports (cont'd)

No.	Authors	Title	Date
815	Haber, R. B., C. S. Jog, and M. P. Bendsøe	A new approach to variable-topology shape design using a constraint on perimeter—*Structural Optimization* **11**, 1–12 (1996)	Feb. 1996
816	Xu, Z.-Q., and K. J. Hsia	A numerical solution of a surface crack under cyclic hydraulic pressure loading	Mar. 1996
817	Adrian, R. J.	Bibliography of particle velocimetry using imaging methods: 1917–1995—*Produced and distributed in cooperation with TSI, Inc., St. Paul, Minn.*	Mar. 1996
818	Fried, E., and G. Grach	An order-parameter based theory as a regularization of a sharp-interface theory for solid–solid phase transitions—*Archive for Rational Mechanics and Analysis*, in press (1996)	Mar. 1996
819	Vonderwell, M. P., and D. N. Riahi	Resonant instability mode triads in the compressible boundary-layer flow over a swept wing—*Physics of Fluids*, in press (1996)	Mar. 1996
820	Short, M., and D. S. Stewart	Low-frequency two-dimensional linear instability of plane detonation—*Journal of Fluid Mechanics*, in press (1997)	Mar. 1996
821	Casagranda, A., and P. Sofronis	On the scaling laws for the consolidation of nanocrystalline powder compacts—Proceedings of the IUTAM Symposium on the Mechanics of Granular and Porous Materials (1996)	Apr. 1996
822	Xu, S., and D. S. Stewart	Deflagration-to-detonation transition in porous energetic materials: A comparative model study—*Journal of Fluid Mechanics*, in press (1997)	Apr. 1996
823	Weaver, R. L.	Mean and mean-square responses of a prototypical master/fuzzy structure—*Journal of the Acoustical Society of America*, in press (1996)	Apr. 1996
824	Fried, E.	Correspondence between a phase-field theory and a sharp-interface theory for crystal growth—*Continuum Mechanics and Thermodynamics*, in press (1997)	Apr. 1996
825	Students in TAM 293–294	Thirty-third student symposium on engineering mechanics, J. W. Phillips, coordinator: Selected senior projects by W. J. Fortino II, A. A. Mordock, and M. R. Sawicki	May 1995
826	Riahi, D. N.	Effects of roughness on nonlinear stationary vortices in rotating disk flows—*Mathematical and Computer Modeling*, in press (1996)	June 1996
827	Riahi, D. N.	Nonlinear instabilities of shear flows over rough walls	June 1996
828	Weaver, R. L.	Multiple scattering theory for a plate with sprung masses: Mean and mean-square responses	July 1996
829	Moser, R. D., M. M. Rogers, and D. W. Ewing	Self-similarity of time-evolving plane wakes	July 1996
830	Lufrano, J. M., and P. Sofronis	Enhanced hydrogen concentrations ahead of rounded notches and cracks—Competition between plastic strain and hydrostatic constraint	July 1996
831	Riahi, D. N.	Effects of surface corrugation on primary instability modes in wall-bounded shear flows	Aug. 1996
832	Bechel, V. T., and N. R. Sottos	Measuring debond length in the fiber pushout test—Proceedings of the ASME Mechanics and Materials Conference (1996)	Aug. 1996
833	Riahi, D. N.	Effect of centrifugal and Coriolis forces on chimney convection during alloy solidification—*Journal of Crystal Growth*, in press (1997)	Sept. 1996
834	Cermelli, P., and E. Fried	The influence of inertia on configurational forces in a deformable solid—*Proceedings of the Royal Society of London A*, in press (1996)	Oct. 1996
835	Riahi, D. N.	On the stability of shear flows with combined temporal and spatial imperfections	Oct. 1996
836	Carranza, F. L., B. Fang, and R. B. Haber	An adaptive space–time finite element model for oxidation-driven fracture	Nov. 1996
837	Carranza, F. L., B. Fang, and R. B. Haber	A moving cohesive interface model for fracture in creeping materials	Nov. 1996

List of Recent TAM Reports (cont'd)

No.	*Authors*	*Title*	*Date*
838	Balachandar, S., R. Mittal, and F. M. Najjar	Properties of the mean wake recirculation region in two-dimensional bluff body wakes	Dec. 1996
839	Ti, B. W., W. D. O'Brien, Jr., and J. G. Harris	Measurements of coupled Rayleigh wave propagation in an elastic plate	Dec. 1996
840	Phillips, W. R. C.	On finite-amplitude rotational waves in viscous shear flows	Jan. 1997
841	Riahi, D. N.	Direct resonance analysis and modeling for a turbulent boundary layer over a corrugated surface	Jan. 1997
842	Liu, Z.-C., R. J. Adrian, C. D. Meinhart, and W. Lai	Structure of a turbulent boundary layer using a stereoscopic, large format video-PIV	Jan. 1997
843	Fang, B., F. L. Carranza, and R. B. Haber	An adaptive discontinuous Galerkin methods for viscoplastic analysis	Jan. 1997
844	Xu, S., T. D. Aslam, and D. S. Stewart	High-resolution numerical simulation of ideal and non-ideal compressible reacting flows with embedded internal boundaries	Jan. 1997
845	Zhou, J., C. D. Meinhart, S. Balachandar, and R. J. Adrian	Formation of coherent hairpin packets in wall turbulence	Feb. 1997
846	Lufrano, J. M., P. Sofronis, and H. K. Birnbaum	Elastoplastically accommodated hydride formation and embrittlement	Feb. 1997
847	Keane, R. D., N. Fujisawa, and R. J. Adrian	Unsteady non-penetrative thermal convection from non-uniform surfaces	Feb. 1997
848	Aref, H., and M. Brøns	On stagnation points and streamline topology in vortex flows	Mar. 1997
849	Asghar, S., T. Hayat, and J. G. Harris	Diffraction by a slit in an infinite porous barrier	Mar. 1997
850	Shawki, T. G., H. Aref, and J. W. Phillips	Mechanics on the Web—Proceedings of the International Conference on Engineering Education (Aug. 1997, Chicago)	Apr. 1997
851	Stewart, D. S., and J. Yao	The normal detonation shock velocity–curvature relationship for materials with non-ideal equation of state and multiple turning points	Apr. 1997
852	Fried, E., A. Q. Shen, and S. T. Thoroddsen	Traveling waves, standing waves, and cellular patterns in a steadily forced granular medium	Apr. 1997
853	Boyland, P. L., H. Aref, and M. A. Stremler	Topological fluid mechanics of stirring	Apr. 1997
854	Parker, S. J., and S. Balachandar	Viscous and inviscid instabilities of flow along a streamwise corner	May 1997
855	Soloff, S. M., R. J. Adrian, and Z.-C. Liu	Distortion compensation for generalized stereoscopic particle image velocimetry	May 1997
856	Zhou, Z., R. J. Adrian, S. Balachandar, and T. M. Kendall	Mechanisms for generating coherent packets of hairpin vortices in near-wall turbulence	June 1997
857	Neishtadt, A. I., D. L. Vainshtein, and A. A. Vasiliev	Chaotic advection in a cubic Stokes flow	June 1997
858	Weaver, R. L.	Ultrasonics in an aluminum foam	July 1997
859	Riahi, D. N.	High gravity convection in a mushy layer during alloy solidification	July 1997
860	Najjar, F. M., and S. Balachandar	Low-frequency unsteadiness in the wake of a normal flat plate	Aug. 1997